A semi-analytical approach to simulate strains in load sensing bearings using FEA
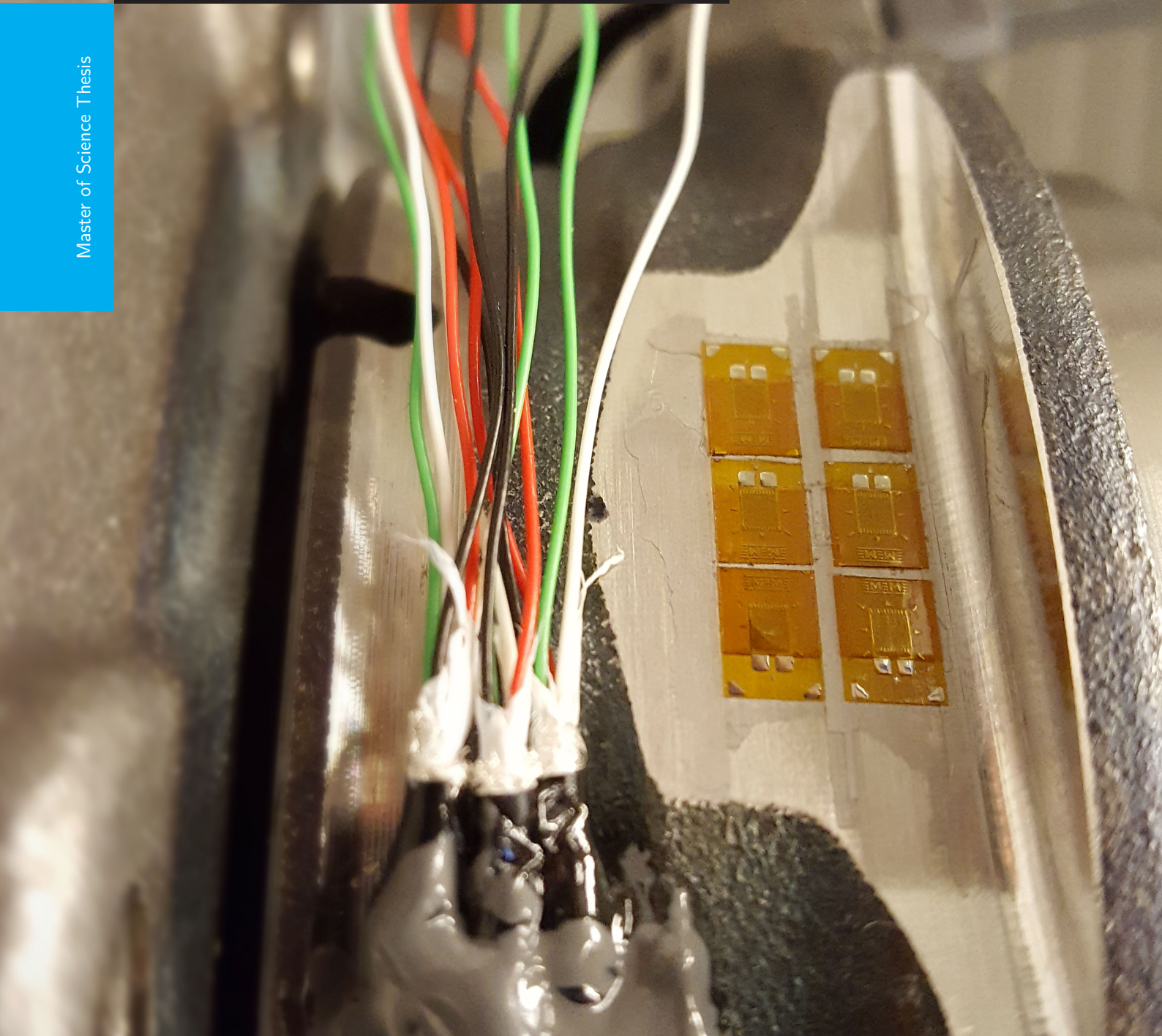
Jens Ravesloot, 4010140

August 29, 2019

TU Delft
Delft
University of
Technology

Challenge the future

A SEMI-ANALYTICAL APPROACH TO SIMULATE STRAINS IN LOAD SENSING BEARINGS USING FEA

MASTER OF SCIENCE THESIS

For the degree of Master of Science in Vehicle Engineering at
Delft University of Technology

By

JENS RAVESLOOT
4010140

On

August 29, 2019

This research is confidential and cannot be made public until further notice.

Faculty of Mechanical, Maritime and Materials Engineering
Delft University of Technology

DELFT UNIVERSITY OF TECHNOLOGY
DEPARTMENT OF COGNITIVE ROBOTICS (CoR)

The undersigned hereby certify that they have read and recommend to the Faculty of
Mechanical, Maritime and Materials Engineering (3mE) for acceptance a thesis
entitled

A SEMI-ANALYTICAL APPROACH TO SIMULATE STRAINS IN
LOAD SENSING BEARINGS USING FEA

by

JENS RAVESLOOT

in partial fulfillment of the requirements for the degree of

MASTER OF SCIENCE VEHICLE ENGINEERING

Dated: August 29, 2019

Supervisors:

Dr.ir. Barys Shyrokau

Ir. Henk Mol (SKF)

Graduation committee:

Prof.dr.ir. Martijn Wisse

Dr.ir. Carlos Hernandez Corbato

Abstract

The advancements in driver assistance systems in cars and the development of autonomous vehicles require more states of the car to be known than the conventional sensors can accurately determine. Load sensing bearings (LSBs) are under development that measure the wheel forces under dynamic load. Through sensor fusion, the addition of this sensor can increase the robustness and accuracy of the state estimators used in cars. An algorithm uses the strain measured on the surface of an instrumented LSB to calculate the forces on the bearing. The development of LSBs requires a tool that simulates the strain signals in a fast and accurate manner to gain insight into the bearing behavior.

Due to the complex nonlinear behavior of the bearing, there is not a fast, straightforward tool available that estimates its strains. This thesis presents a methodology that uses finite element analyses (FEA) to construct a model that calculates the strain in the outer ring of a wheel bearing for any given load. The FEA consists of a linear elastic model of the outer ring and a single loaded ball that is modeled by a Hertzian contact. Multiple simulations are done for different positions of the ball, such that a rotating bearing can be approximated. A nonlinear analytical bearing model in conjunction with a, from FEA constructed, outer ring flexibility model calculates the load on each bearing ball. A strain model, also built from the FEA, uses these loads to calculate the strain on the outer ring.

The simulated strains are validated with experiments performed on a bearing test rig of SKF. Measurements from a with strain gauges instrumented bearing show that the model predicts the observed behavior in the signals. Analyses of the simulated and measured signals in the frequency domain show a difference in gain and offset, which can be calibrated. Unexpected discrepancies are observed within the measured signals of symmetrically placed sensors on the LSB, which should give identical signals, that are likely caused by a distortion of the shape of the outer ring introduced by the manufacturing process or installation of the bearing.

The scope for future work should focus on further validation of the model and developing a calibration method to increase the accuracy. It is believed that the uncertainties in the model can be summarized into a small set of parameters that can be calibrated for a specific instrumented LSB with only a few measurements. Once accurate strains can be simulated, the model could be utilized in a state observer to convert actual strain measurements into loads, and it is possible to use it to optimize the design of the LSB and the location of the strain gauges.

CONTENTS

NOMENCLATURE

Indices:

i Index used for inner ring or raceway

o Index used for outer ring or raceway

0 Index used to indicate initial state, when no load is applied to bearing

k Index used to indicate symbol is used separately for both rows (i.e., $k = i, o$)

Greek characters:

α Contact angle

$\hat{\alpha}$ Normalized contact angle on range [-1,1]

δ Deformation of contact area

δ^* Dimensionless contact parameter to calculate δ

δ_n Normal approach of raceways under load

ε Strain

Θ Compliance approximation

θ_m Compliance of the corresponding m-shape

ν Poisson's ratio

ξ Strain per load

$\Sigma(\rho)$ Curvature-sum of rolling element and raceway

$F(\rho)$ Curvature-difference of rolling element and raceway

σ Normal stress in the contact area

φ Compliance shapes

ψ Azimuth in outer ring

Ψ Azimuth of applied load in outer ring

Ω Matrix containing polynomials

Ω_α A set of Chebyshev polynomials

Ω_ψ A set of Fourier polynomials

ω_α Chebyshev polynomials

ω_Ψ Fourier polynomials

Letters:

a Large semi-axis of the contact ellipse

a^* Dimensionless contact parameter to calculate a

b Small semi-axis of the contact ellipse

b^* Dimensionless contact parameter to calculate b

C Material properties related constant in Hertzian contact model

$c_{k,w}$ Coefficient of the combined Fourier and Chebyshev polynomials

D Rolling element diameter

E Young's modulus

F Load on bearing

K Amount of modes in the dimension of the amount of applied loads

K load-deflection factor of Hertzian contact model

K^{-1} Compliance function

M Amount of modes in the dimension of the azimuth

p_r Row pitch circle diameter

p_y Distance between pitch circles of both rows

Q Rolling element load

R Radial location of raceway

r Raceway groove curvature

S Distance between raceway loci

u Raceway deformation

W Amount of modes in the dimension of the contact angle

X Displacement of inner ring

Y Axial location of raceway

ACKNOWLEDGMENTS

1

INTRODUCTION

Cars are being designed and mass-produced for more than 100 years now, while safety and efficiency are continually improving. The next big step in transportation technology is the introduction of the autonomous car. Estimations show that about 90% of all traffic accidents are caused by human error, so it is expected that autonomous driving systems will improve safety while it also improves the traffic flow [1]. Due to technological advancements, the systems required for autonomous cars become better and cheaper to implement, and the desire to reduce traffic incidents and casualties increasingly makes these systems integral to the design of the car [2]. For these systems to function well, the car should know what happens in and around it with increased performance and reliability, which can be achieved with sensor fusion. Similar requirements also become necessary for the wheel dynamics where the states of the wheels should be known, since estimating the wheel force from only the accelerometer is not reliable and has low performance with 150 ms delay [3]. Multiple different technologies are being developed to sense the forces that act on the wheels like suspension force sensors [4], wheel force transducers [5, 6], smart tires [7–9], and load sensing bearings [10–12].

This thesis focuses on the development of a methodology to calculate the strains in an outer ring of a wheel end bearing which can aid in the development of a load sensing bearing.

1.1. INTRODUCTION TO HBU3 BEARINGS

For more than a decade, SKF has been developing one of these load sensing bearings (LSB) on their HBU3 (Hub Bearing Unit 3) bearing series, which are double-row ball bearings that are placed inside the wheels of cars. Figure 1.1 shows an image of such an HBU3 bearing. It is cut open so that the internals can be seen. The red part is the inner ring and, the green part is the outer ring. Two rows of balls, the so-called rolling elements, transfer the load on the inner ring to the outer ring while it can rotate freely
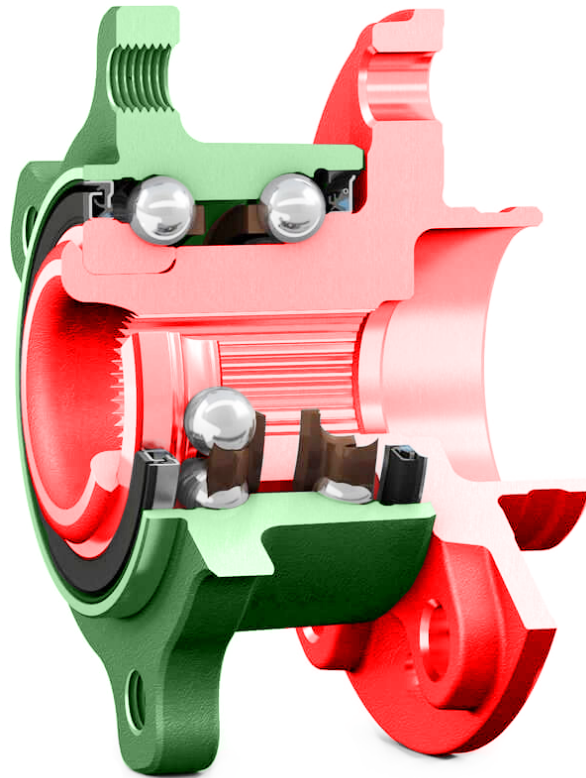
Figure 1.1: An HBU3 bearing cut open so its internals can be seen. The outer and inner ring are shown in green and red, respectively. Between the rings are two rows of balls, the so-called rolling elements. The brown part around the rolling elements is called a cage and keeps all the rolling elements at an equal distance from each other. Seals are on either side of both rows to prevent grease from leaving the bearing and dust entering it.

around its axial axis. Each row has a cage, the brown parts, that keep all the rolling elements at an equally spaced distance in their respective rows. To ensure low friction and increase the lifetime of the bearing, grease is placed around the rolling elements. Seals on either side of the rows keep the grease in place and prevent dust from entering the bearing. In a car, each wheel contains one of these HBU3 bearings. The outer ring has four threaded holes which are used to assemble it on the knuckle of a car. The brake disk and wheel are attached to the inner ring.

In this report, two coordinate systems are used in the bearing. In some cases, a Cartesian system is used with coordinates x, y, and z, and a cylindrical system is used with coordinates r, ψ, and y in other cases. The y-axis is the same in both systems. Figure 1.2 shows a schematic cross-section and side view of the HBU3 bearing. As with the previous picture, the outer ring is green, and the inner ring is red. The left side in figure 1.2a is mounted on the knuckle. This side is called the inboard side, and
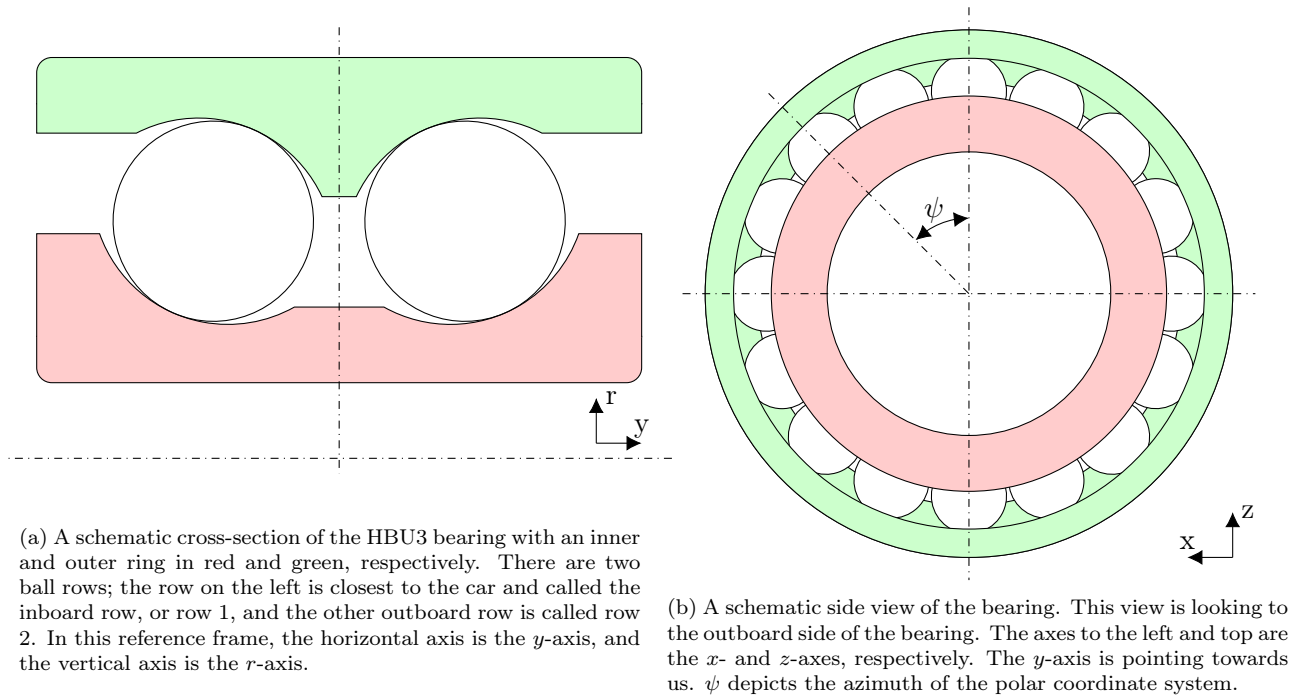
(a) A schematic cross-section of the HBU3 bearing with an inner and outer ring in red and green, respectively. There are two ball rows; the row on the left is closest to the car and called the inboard row, or row 1, and the other outboard row is called row 2. In this reference frame, the horizontal axis is the y-axis, and the vertical axis is the r-axis.

(b) A schematic side view of the bearing. This view is looking to the outboard side of the bearing. The axes to the left and top are the x- and z-axes, respectively. The y-axis is pointing towards us. ψ depicts the azimuth of the polar coordinate system.

Figure 1.2: Schematic views of the bearing. A Cartesian (x,y,z) and a cylindrical (r,ψ,y) coordinate system are used often throughout this report. The y-axes of both systems are the same.

the row in that position is called row 1. The right side is attached to the brake disk and wheel and is called the outboard side. The corresponding row is row 2. Figure 1.2b shows the side view of the bearing when looked upon from the outboard side. Any azimuth ψ is referenced from the top, the z-axis, and rotates counterclockwise. The x-axis is pointing to the left side, and the y-axis is pointing towards us, the outboard side. The coordinates of both coordinate systems are shown in both figures.

Any load applied to the inner ring will be transferred through the rolling elements to the outer ring. The contacts between the rolling elements and the rings can be considered as nonlinear springs which deform under load. This means that the inner ring displaces with respect to the outer ring when a load is applied. This displacement also causes a change in the contact angle. This is the angle between the contact force acting on the rolling element and the radial axis. Figure 1.3 shows animations of how the inner ring and rolling elements schematically deform when a moment is applied (left) and when an axial load is applied (right). The inner and outer ring are considered rigid in these animations, while in reality the outer ring deforms significantly due the loads on the individual rolling elements. Each different load case on the bearing creates a different distribution of the loads over the rolling elements. This, in turn, creates a distinct deformation of the outer ring. By measuring the strain on the outer ring of the bearing, it should, in theory, be possible to estimate the total load that acts on

(a) A moment applied to the inner ring will rotate it. The contacts between the rolling elements and the rings act as a nonlinear spring and will deform.

(b) When a pure radial load is applied to the inner ring, it will stay aligned with the outer ring but move closer or further away.

Figure 1.3: Schematic of the loaded bearing. The inner ring displaces with respect to the outer ring. These figures are animations and only work in Adobe Reader.

the bearing.

1.2. CHALLENGES IN LOAD ESTIMATIONS

In SKF, this HBU3 bearing unit is equipped with strain gauges that measure the strain on the surface of the outer ring of the bearing. Most algorithms used to determine the forces are data-driven and show promising results, but remain not accurate enough [10, 13]. The exact reasons for these problems remain unclear although the following phenomena are believed to be the source of these uncertainties:

Preload Both bearing rows are installed with a certain preload to ensure that there is no play in the bearing and to increase its life. The preload strongly influences the strain on the outer ring. To give an example, the loads on the rolling elements are calculated for different bearing loads and preloads with the rigid bearing model, presented later in this report. Figure 1.4 shows how the load on the highest loaded element is related to the preload (defined in axial interference) and the radial bearing load. Assumed here is a rigid outer bearing ring. Due to creep, wear, and plastic deformation, the preload will change over time.

Temperature An increase in temperature expands the material and thus directly changes the strain [14]. This deformation also changes the preload on the bearing, which indirectly affects the strain. The influence of the temperature can be
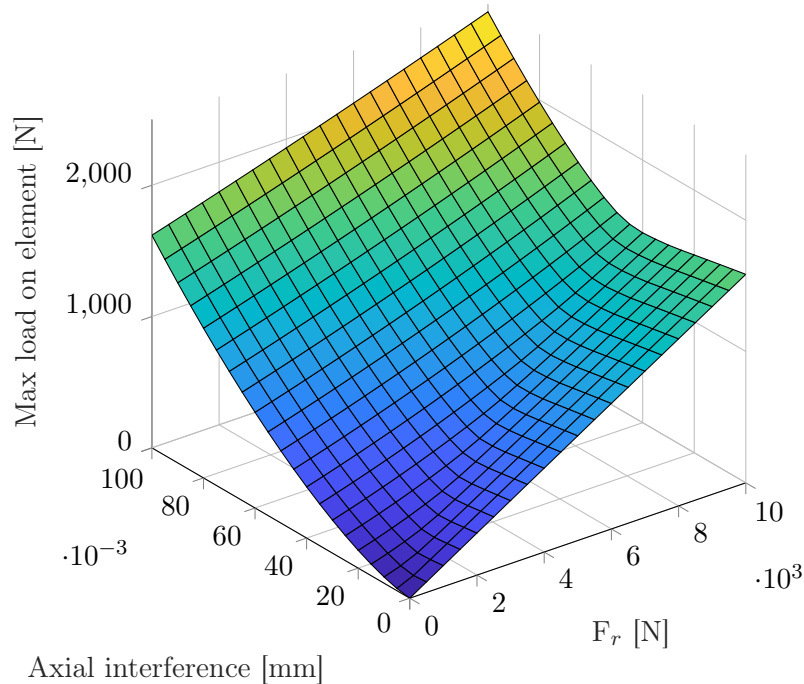
Figure 1.4: The load on the maximum loaded rolling element as a function of a radial load applied to the bearing and a preload (defined by axial interference). Assumed is a rigid inner and outer bearing ring. A change in preload drastically changes the loads on the rolling elements. An HBU3 bearing typically has a preload of about 30 µm.

categorized into a local temperature difference and a global temperature difference. Rolling friction of the loaded elements causes local temperature differences and has the same deformation shapes as the strains and are thus hard to compensate for. The global temperature differences are caused by the temperature of surrounding components, which for instance heat up due to braking.

Row interference The strain gauges measure the superposed strains of both rows at the same time. It is difficult to distinguish the contribution of each row to this signal.

Surrounding stiffness The HBU3 is mounted in the car on a knuckle which has a varying stiffness along the whole bearing circumference [15]. Although this is a factor that can be modeled beforehand, it complicates the understanding of how the bearing behaves. The clamping force of each bolt also influences the strain by creating stresses in the outer ring. These change each time a bearing in being reinstalled on the car.

Different load algorithms have been explored that try to eliminate some of these effects. These algorithms can be classified into generation 1 (G1) and generation 2 (G2)

algorithms. Note that generation 2 does not imply that it is more advanced or better at estimating the loads. Each generation has its advantages and disadvantages:

Generation 1 This first-generation tries to determine the individual contact forces and angles of each rolling element in order to calculate the total force acting on the bearing. Generally, these algorithms are less sensitive to global temperature differences. On the other hand, these algorithms need to distinguish the contribution of each row, which is difficult.

Generation 2 The G2 algorithms look at the global bearing deformation, specifically the outer bearing ring deformation, to estimate the forces that are applied to the bearing. This basically means that the bearing is modeled as a load cell, and a low-pass filter is applied to the measured signals. The advantage of these methods is that they can observe fast load variations. Any temperature gradient in the bearing makes these algorithms very inaccurate.

The existing data-driven load estimation algorithms are at the moment not capable enough to cope with all the uncertainties. More understanding of how the bearing behaves is necessary to make the algorithms more accurate.

1.3. Challenges in gaining insights

To better understand how the bearing behaves under loading conditions, two methods are used to acquire strain gauge signals for different load cases. The first method is by simulating the bearing in a finite element analysis (FEA) model. This model consists of an inner ring and outer ring within between 32 rolling elements, divided over two rows. Each rolling element has one contact with each ring, resulting in 64 contact constraints in the model. Since all these constraints are highly nonlinear and need a very fine mesh, the model takes a very long time to solve. Solving this model for one load case and for one position of the rolling elements takes at least one hour on a computing cluster. If the bearing rotates in time, and thus the rolling elements change position, then the model needs to be solved again. Due to this time-consuming process, only a limited amount of load cases can be calculated.

Another method for gaining the strain gauge signals is by using a physical test rig. A bearing unit is instrumented with strain gauges and placed on this rig which rotates it and applies a load. This gives more accurate results and can easily apply many different load cases to the bearing, but these setups are limited in the number of strain gauges that are installed on the bearing. These sensors, including their conditioners and AD-converters, are expensive, and the surface of the bearing can only accommodate a finite amount of sensors. On top of that, the bearing acts as a black box on which a load is applied and outputs certain strains. It is hard to directly know the loads and contact angles of each rolling element and their individual influence on the strains. There are currently no tools available that are fast and accurate in calculating the strain signals for certain load cases.

1.4. Research question

The development of a load sensing bearing requires knowledge about the strain signals from an HBU3 bearing when it is loaded. Since the modeling in FEA and experiments on the test rig are expensive, a third option is explored in this thesis; a fast semi-analytical model is proposed that can generate the strains based on FEA simulations. This Master's thesis tries to answer the following question:

Main research question:
How can a bearing model be constructed with finite element analyses data such that the strains on the outer bearing ring can be simulated for different load cases?

Some subquestions are made related to the research question that could help to better understand the strains due to the bearing mechanics. To simulate the strains on the outer ring, it is necessary to know the loads and possibly the contact angles of each rolling element. This leads to the first subquestion:

Subquestion 1:
What mechanics in the bearing determine the loads and contact angles on each rolling element?

The strains on the outer ring of the bearing are simulated once the loads and contact angles are known. Generation 1 algorithms try to estimate the loads on each individual rolling element. One way to do this is by translating the measured strain into the frequency domain. This shows a peak at the frequency at which all the rolling elements pass the sensor. The amplitude of this frequency is called the first harmonic. The second harmonic is the same at twice the frequency. Analyses of previously measured strain signals have resulted in the hypothesis that by looking at these first and second harmonics of the strain gauge signal, it might be possible to distinguish between ball rows and observe the contact angles more accurately. To better understand how the measured signal is related to the mechanics of the bearing, the following subquestion is composed:

Subquestion 2:
What are the effects of the contact angle on the first and second harmonics of the strain signal?

Strain gauges installed on the bearing give a signal on one location in the time domain. When the bearing is circular symmetric and an axial load is applied (i.e., all the

individual rolling element loads are identical) it is easy to visualize that the measured signal is the same as the strain along the circumference of the ring. In other words, the strain in the time domain is the same as the strain in the spatial domain. See figure 1.5 for an example of this strain.
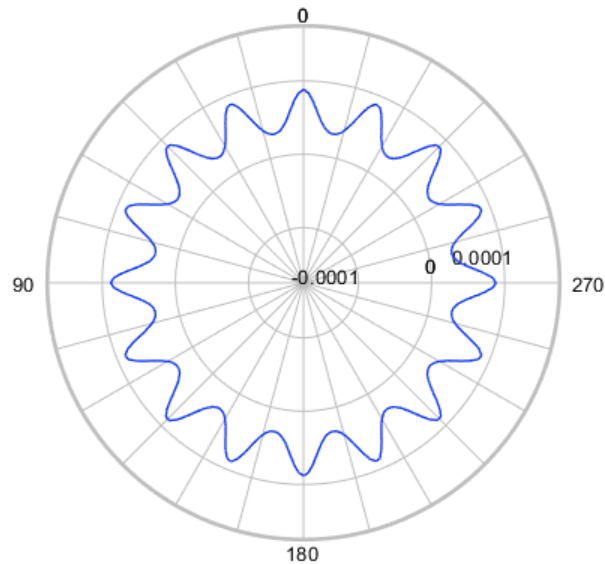

Figure 1.5: Polar plot of radial strain (mm/mm) on a line along the circumference of an axisymmetric outer ring where a pure axial load is applied. In this case, the strain is perfectly rotational symmetric; thus the strain signal measured at one fixed location during rotation would be identical to the strain measured along the outer ring.

It would be interesting to know if this relation between the time domain and the spatial domain is the same for a different bearing or a different load case:

Subquestion 3:
Are the strains in the time domain and the spatial domain related?

The proposed methodology will use FEA simulations to generate data for the model. These simulations can take up a long time, especially when many nonlinear behavior is modeled. Since one of the goals of the model is to be fast, the FEA needs to be simplified to reduce the computation time. This leads to the final subquestion:

Subquestion 4:
How can the FEA be simplified to decrease the computation time, but maintain accuracy?

With the help of these questions, a methodology will be proposed that is fast and can estimate the strains on the strain gauge locations.

1.5. Report overview

This report gives an overview of what is achieved during a Master's thesis on the subject of creating a model that computes the strains on the surface of a bearing when loads are applied. The model is presented in chapter 2. In chapter 3, the proposed model is compared with experiments, and finally, the thesis is concluded in chapter 4. Some figures contain animations instead of just static images. These animations work in Adobe Reader, so it is advised to use this program to view this PDF.

2

PROPOSED SEMI-ANALYTICAL MODEL

A fast model that calculates the surface strain for loads on a bearing is instrumental in developing an algorithm to estimate the loads on a bearing instrumented with strain gauges. This thesis aims to construct such a load-to-strain model by using FEA data, which will be explained in this chapter.
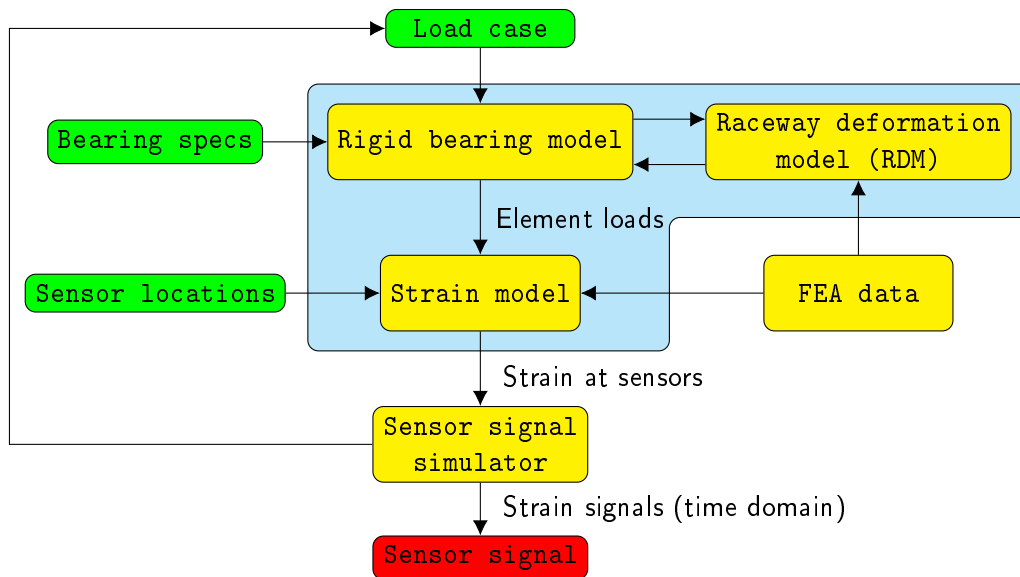
Figure 2.1: Schematic overview of the proposed model. The rigid bearing model and RDM together calculate the distribution of the loads over all the rolling elements. The strain model converts these into a strain on the locations of the simulated sensors. Both the RDM and strain model are constructed from FEA simulations once. The sensor signal simulator controls the load case and azimuths of the rolling elements over time. These are fed back into the whole model. These successive simulations generate a strain signal in the time domain.

2.1. Overview of all submodels

The proposed semi-analytical model consists of multiple parts that all have their function. Figure 2.1 shows schematically how the model will be built and what the individual submodels are. In the schematic overviews, the green blocks represent inputs, and the red blocks represent outputs. The following list gives a description of all the parts of this model:

FEA data The FEA should be used to calculate the full displacement field of the outer bearing ring, which is the input for the raceway deformation model and strain model. Only one rolling element is modeled and placed on different places along the raceways. By calculating all these different positions, enough data can be generated to build the other models. The FEA only contains the outer bearing ring and its plate on which it is attached in order to reduce the number of elements.

Rigid bearing model For the strains to be calculated on the outer ring, the loads on all the rolling elements need to be known. All the rolling elements and the deformation of the outer ring behave like a large system with many springs, as can be seen in figure 2.2. Here the coils in the image represent the nonlinear Hertzian contacts, and the green and red rings represent the deformed outer and rigid inner ring of the bearing, respectively. To find the equilibrium of this system, it is split into a nonlinear rigid bearing model that calculates the loads on each rolling element for a predefined deformation and displacement of the inner and outer ring, and a linear elastic raceway deformation model that calculates the deformation of the outer ring as a function of the load of the rolling elements acting on it. The rigid bearing model is an analytical model that calculates the individual loads, contact angles, and contact shape according to the Hertzian contact theory and bearing theory as described in [16]. The rigid bearing model will be validated with simulations of SimPro, which has the possibility to simulate all the contact forces with a rigid outer ring.

Raceway deformation model A semi-analytical model will be used to estimate the deformation of the raceway due to the loads acting on it. This deformation causes the loads to redistribute differently over all the elements. This model can then be iterated with the rigid bearing model until equilibrium is reached. The semi-analytical raceway deformation model uses FEA data to construct deformation shapes and corresponding coefficients. This FEA data needs to be generated one time only. Once this semi-analytical model is built, this FEA is not needed anymore, making this raceway deformation model fast.

Strain model The FEA data used for the semi-analytical raceway deformation model can also be used to construct a new model that relates the strain in the outer ring to the loads on all the elements. The strain will be a function of the location
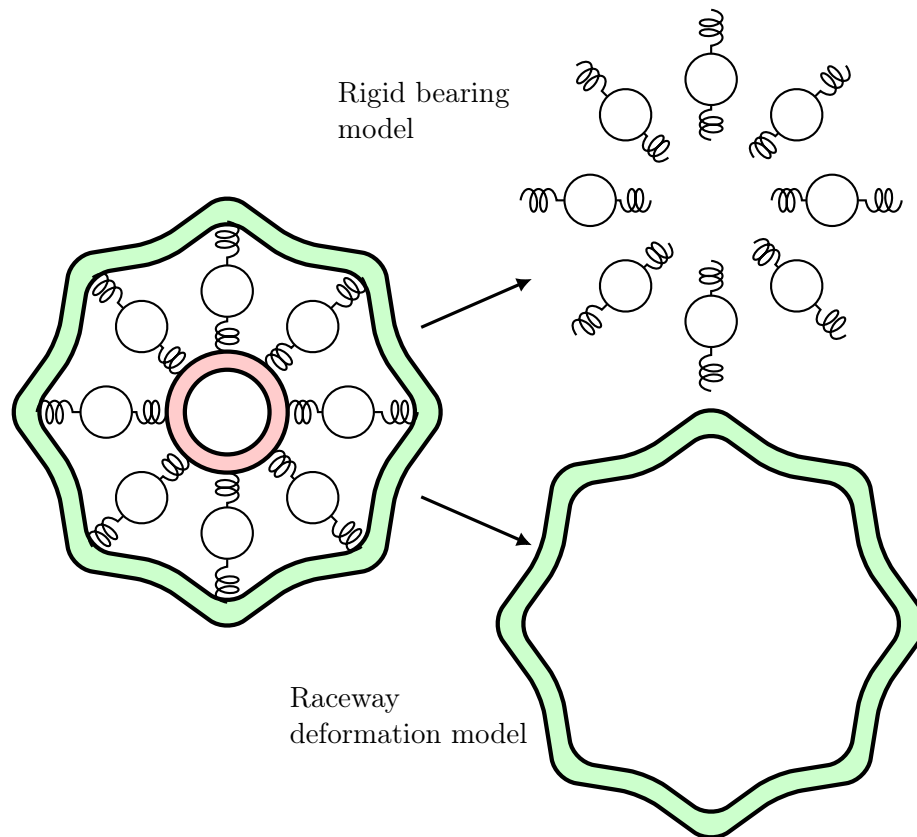
Figure 2.2: To calculate the load distribution over all the rolling elements, the Hertzian contact behavior and the outer ring deformation are split into separate models called the rigid bearing model and the raceway deformation model, respectively. The rigid bearing model is nonlinear and analytic, while the raceway deformation model is assuming a linear elastic outer ring, but is based on numerically solved FEA data.

of the rolling elements and their contact angles. Before this strain model is constructed a set of strain gauge locations is determined for which this model is generated.

Sensor signal simulator Once the strains are known, it is possible to simulate the sensor signals for predefined strain gauge locations. The sensor signals are calculated by letting the whole model, indicated by the blue area in figure 2.1, run with small increments in the rotation of the cages of the rolling elements for varying load cases. The whole model can be validated by comparing these resulting strain signals with measurements taken on the BETSY (BEaring Test SYstem) rig.

2.2. RIGID BEARING MODEL

A model is being built that is able to generate the strains based on the load that is acting on the bearing. The first step in this model is to calculate the load distribution of the forces on all the rolling elements. An analytical model based on the equations from [16] is used to calculate the forces acting on each rolling element. For simplicity, only the equations for row 1 are given. The equations for the second row are the same but flipped in the axial direction. Figure 2.3 shows an overview of how this model is constructed.
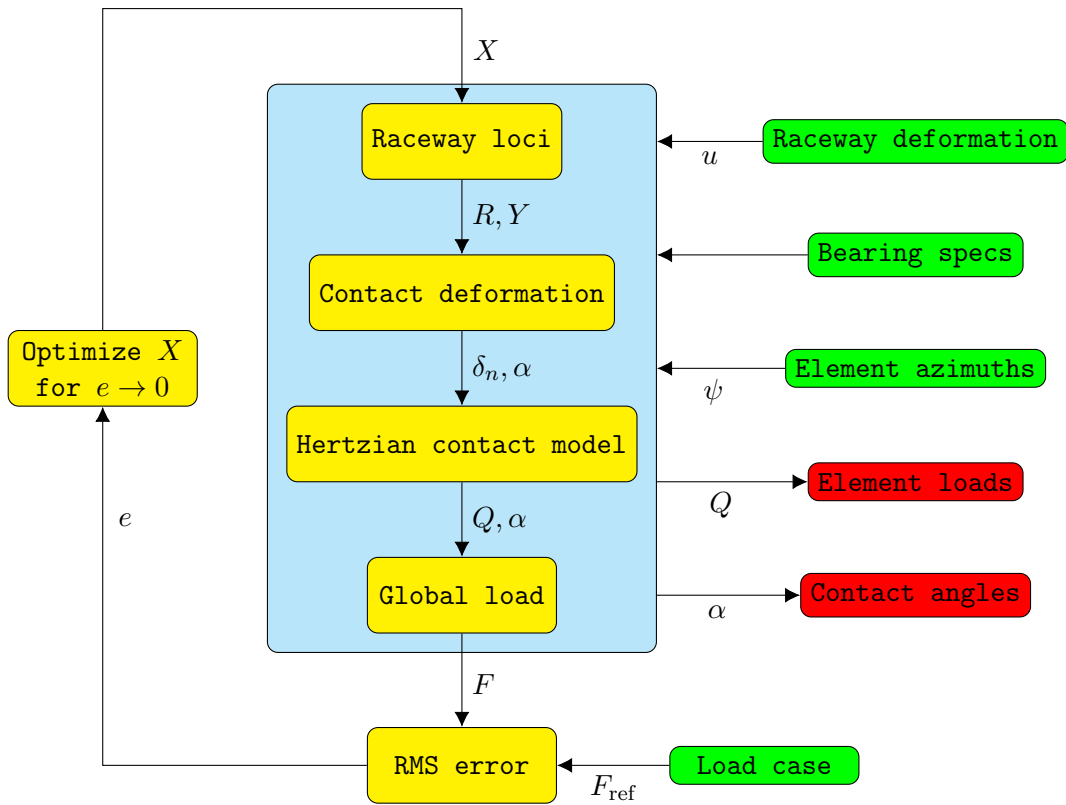

Figure 2.3: Schematic overview of the rigid bearing model. A displacement of the inner ring, X, is used to calculate the loads and contact angles on all the rolling elements, which then is used to calculate the global load that acts on the bearing. This load is compared to the desired load, F_{ref}, and iterated until the correct X is found. The outputs of the model are the rolling element loads and contact angles.

The outer and inner ring of the bearing are assumed rigid in this model. Later in section 2.3 a variable u is added which represents the raceway deformation of the outer ring account for the finite stiffness of this outer ring. The input of the model is a displacement X of the inner ring with respect to the outer ring. The compression of

the contact areas can be calculated via trigonometry. These are then used to calculate the individual contact loads which can be combined to find the total load that acts on the bearing. In short, this rigid bearing model calculates the global bearing load for a given inner ring displacement.

The input of this model, however, should be the global load acting on the bearing while the output should be the contact parameters. In order to achieve this, an optimization is used to find the value for X such that the global load on the bearing is equal to the desired load case. Once this displacement is found, the contact parameters can be extracted from the model.

2.2.1. LOCATION OF RACEWAY LOCI ALONG AZIMUTH

The first step of the rigid bearing model is to determine the loci of all the raceways. Figure 2.4 shows a schematic of the cross-section of the inner and outer ring of the HBU3 bearing, depicted in red and green, respectively. The outer ring is fixed to the

(a) Schematic cross-section of the inner and outer ring with the two ball rows visible. Row 1 is on the left, and row 2 on the right. The green and red dots represent the loci of the outer and inner raceways, respectively. The loci are the centers of the arcs in the image that represent the raceways.

(b) Close-up of row 1. It can be seen that the initial contact angle α_0 is the angle between the vertical line and the line that passes through points of contact with the inner and outer raceways. This line also passes through both loci.
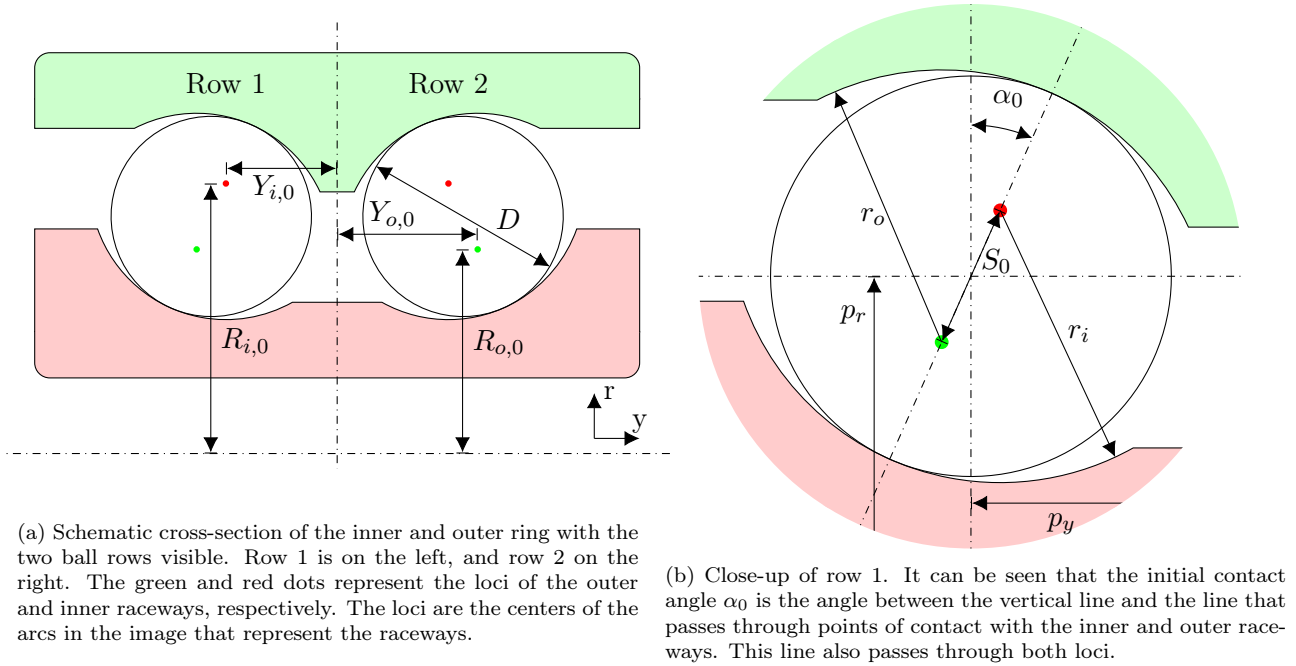
Figure 2.4: Schematic cross-section of the HBU3 bearing in unloaded condition. Green represents the outer ring, and red the inner ring. This schematic bearing is circular symmetric around the horizontal dashed line in figure 2.4a.

hub of the car while the inner ring rotates and is connected to the wheel. Each HBU3 bearing has two bearing rows filled with balls, the so-called rolling elements. Each row has an inner and an outer raceway, which is the groove in which the rolling elements roll. The center of each raceway is called the raceway locus and the locations of these are displayed with the red and green dots in the figure.

The centerline underneath the left image shows the axis of the bearing around which this cross-section revolves. The vertical centerline shows the center between the two rows. In our reference frame, the intersection of these lines is (0,0). The parameters shown in these figures are all the parameters that define the geometry of the two bearing rows, and thus the behavior of the whole unit. The letters i and o stand for the inner and outer ring, respectively, while the number 0 stands for the initial unloaded state. The parameters Y and R are the axial and radial distance from the raceway loci to the center of the bearing. $R_{o,0}$, for instance, is the radial distance of the locus of the outer raceway in the undeformed state. These constants are equal for both rows since the HBU3 bearing units have symmetric rows. r_i and r_o are the groove curvatures of the inner and outer raceways, and the diameter of the rolling elements is D. The value of S_0 represents the distance between the loci when the bearing is unloaded and can be calculated with:

$$S_0 = r_i + r_o - D \tag{2.1}$$

Note that the rolling element will try to find a position with the least potential energy. This means that it will go to the position in which it deforms the least. This point can be found by drawing a line between the inner and outer raceway loci. The points where this line intersects the raceways are where the rolling element contacts the raceways in order to have the least deformation. The angle between this line and the vertical line is called the contact angle α. In the figure, the contact angle under no load is represented by α_0.

The pitch circle is the mean of the inner and outer raceway contact diameters. The pitch diameter can be calculated with

$$p_r = R_{o,0} + R_{i,0} + (r_o - r_i)\cos(\alpha_0) \tag{2.2}$$

and the distance between the pitch circle of row 1 and row 2 is

$$p_y = Y_{o,0} + Y_{i,0} + (r_i - r_o)\sin(\alpha_0) \tag{2.3}$$

When a load F is applied to the inner ring, it will displace with respect to the fixed outer ring. Figure 2.5 shows an exaggerated example of this with a radial and axial translation and a rotation of the inner ring. In the Cartesian coordinate system, these forces and displacements of the inner ring can be placed into a vector

$$F = \begin{bmatrix} F_x \\ F_y \\ F_z \\ M_x \\ M_z \end{bmatrix}, \quad X = \begin{bmatrix} x \\ y \\ z \\ \theta_x \\ \theta_z \end{bmatrix} \tag{2.4}$$

We assume there is no friction in the bearing. This means that the bearing is unable
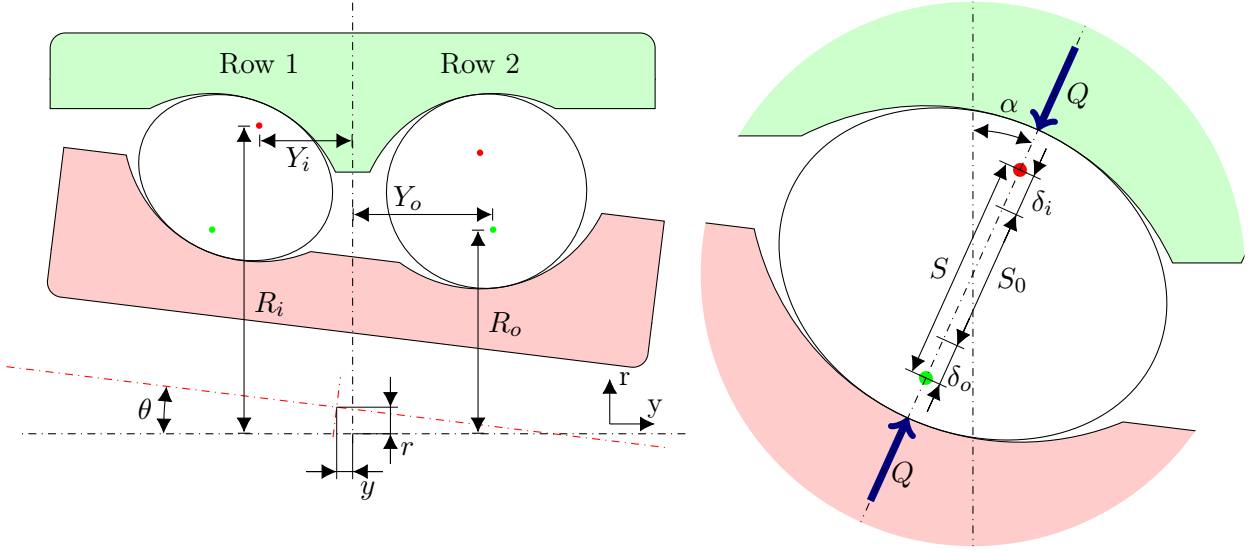
(a) Schematic cross-section of the displaced inner ring. The displacement of the inner ring due to the load on the bearing is represented by a rotation θ and displacements r and y. This displacement also causes the loci of the inner raceway to move.

(b) Close-up of the displaced inner ring. The load on the element, Q, compresses the contact. The deformation of the contact at the outer and inner ring is represented by δ_o and δ_i, respectively.

Figure 2.5: Schematic cross-section of a loaded bearing. The load will cause the inner ring to have a displacement with respect to the outer ring.

to generate a moment around its axial y-axis, so there does not exist a moment M_y. Also, the axial rotation θ_y of the inner ring itself does not influence any other state of the bearing and is therefore not considered.

The initial radial and axial locations of the raceways, $R_{k,0}$ and $Y_{k,0}$, are constants and a property of the bearing. The locations of the raceways after deformation are different at each azimuth ψ. From the figures, the location of the raceway loci can be determined for each position along the azimuth. Assumed are small deformations. For the first row these locations are

$$
\begin{align}
R_i(\psi) = & \quad R_{i,0} + x\sin(\psi) + z\cos(\psi) - Y_{i,0}\left(\sin(\theta_x)\cos(\psi) - \sin(\theta_z)\sin(\psi)\right) && (2.5) \\
Y_i(\psi) = & -Y_{i,0} + y && -R_{i,0}\left(\sin(\theta_x)\cos(\psi) - \sin(\theta_z)\sin(\psi)\right) && (2.6) \\
R_o(\psi) = & \quad R_{o,0} + u_r\left(\psi, \alpha(\psi), Q(\psi)\right) && (2.7) \\
Y_o(\psi) = & -Y_{o,0} + u_y\left(\psi, \alpha(\psi), Q(\psi)\right) && (2.8)
\end{align}
$$

Since our reference frame is fixed to the outer ring, the locations of the loci of the outer ring do not change when this outer ring is considered rigid. We will assume $u_r = 0$ and $u_y = 0$. Later in section 2.3, the outer ring is assumed flexible, and these raceway deformations u_r and u_y will be calculated.

The locations for the second row can be obtained in a similar way. With the locations of the loci known, it is now possible to calculate the deformations of the contact areas.

2.2.2. Deformation of the contact areas

In order to calculate the load Q that acts on each rolling element, it is necessary to know how much each contact area is compressed. The contact angle α is calculated with

$$\alpha(\psi) = \tan^{-1} \left(\frac{Y_i(\psi) - Y_o(\psi)}{R_i(\psi) - R_o(\psi)} \right) \tag{2.9}$$

and the distance between the raceway loci can be expressed by

$$S(\psi) = \left((R_i(\psi) - R_o(\psi))^2 + (Y_i(\psi) - Y_o(\psi))^2 \right)^{1/2} \tag{2.10}$$

As can be seen in figure 2.5, this distance is the sum of

$$S(\psi) = S_0 + \delta_i(\psi) + \delta_o(\psi) \tag{2.11}$$

Here δ_i and δ_o are the deformations of the contacts at the inner and outer raceway. S and S_0 are known, but this is not enough to calculate both deformations. Therefore the sum of the deformations δ is used, which can later be used to calculate the load on the rolling element.

$$\delta(\psi) = \delta_i(\psi) + \delta_o(\psi) = S(\psi) - S_0 \tag{2.12}$$

2.2.3. Loads on rolling elements

Using the Hertzian contact model, the load acting on the rolling elements can be calculated from these deformations. If $\delta < 0$ then the load on the element is 0. The load on each contact is

$$Q_i = K_i \delta_i^{3/2}, \quad Q_o = K_o \delta_o^{3/2} \tag{2.13}$$

Here K is the load-deflection factor. Assumed is that Q_i and Q_o are the only forces acting on the rolling elements, thus $Q_i = Q_o$. Combining this with equations 2.12 and 2.13 gives

$$Q = K\delta^{3/2} \tag{2.14}$$

with K being the equivalent load-deflection factor given by

$$K = \left(\frac{1}{K_i^{-2/3} + K_o^{-2/3}} \right)^{3/2} \tag{2.15}$$

The load-deflection factor for the inner and outer raceway, K_k (with $k = i, o$), is defined in the Hertzian contact model as

$$K_k = \left(\frac{C_k^2}{2} \right)^{-3/2} (\delta_k^*)^{-3/2} \Sigma(\rho)_k^{-1/2} \tag{2.16}$$

Here C_k is a constant related to the material properties of the bearing, the curvature-sum $\Sigma(\rho)_k$ is a constant related to the geometry of the bearing, and δ_k^* is a dimensionless contact parameter which is also related to the geometry of the bearing (with again $k = i, o$). C_k is calculated with

$$C_k = \left(\frac{3}{2} \left(\frac{1 - \nu_k^2}{E_k} + \frac{1 - \nu_b^2}{E_b} \right) \right)^{1/3} \tag{2.17}$$

ν and E are the Poisson's ratio and Young's modulus of the raceway and the ball. In our case, the values for these are assumed to be the same for all raceways and all rolling elements. For a ball bearing the curvature-sum is defined as

$$\Sigma(\rho)_k = \frac{4}{D} - \frac{1}{r_k} + \frac{1}{R_{k,\text{eff}}} \tag{2.18}$$

Here r_k and D are the bearing parameters, as shown in figure 2.4. $R_{k,\text{eff}}$ is the effective radius of the raceways at the location of the contact calculated with

$$R_{i,\text{eff}} = \frac{1}{2} \left(\frac{p_r}{\cos(\alpha)} - D \right) \tag{2.19}$$

$$R_{o,\text{eff}} = -\frac{1}{2} \left(\frac{p_r}{\cos(\alpha)} + D \right) \tag{2.20}$$

The so called curvature-difference is calculated as follows

$$F(\rho)_k = \frac{\frac{1}{r_k} + \frac{1}{R_{k,\text{eff}}}}{\Sigma \rho_k} \tag{2.21}$$

This curvature-difference, $F(\rho)_k$ is used to obtain the dimensionless contact parameter from table table A.1 in appendix A. The contact parameters are a^*, b^*, and δ^*, and are used to calculate the size and deformation of the contact area. δ^* is used in equation 2.16 to calculate the load-deflection factor. This contact area is assumed to have the shape of an ellipse from which the semi-axes a and b are calculated as

$$a_k = a_k^* C_k \left(\frac{Q}{\Sigma \rho_k} \right)^{1/3} \tag{2.22}$$

$$b_k = b_k^* C_k \left(\frac{Q}{\Sigma \rho_k} \right)^{1/3} \tag{2.23}$$

Figure 2.6 shows a detail of what this ellipse can look like on the outer raceway. a and b can be seen here as the semi-axes of the ellipse, and x and y are the local coordinate system along these semi-axes. The stress is distributed on this ellipse as

$$\sigma_k = \frac{3Q}{2\pi a_k b_k} \left(1 - \left(\frac{x}{a_k} \right)^2 - \left(\frac{y}{b_k} \right)^2 \right)^{1/2} \tag{2.24}$$

All these variables are the contact parameters and define the contacts between each rolling element and the raceways.
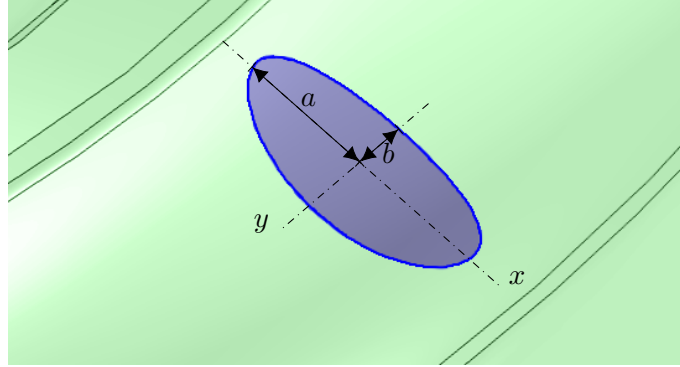
Figure 2.6: Schematic of the contact area between the rolling element and the raceways. This contact area is in the shape of an ellipse with semi-axes a and b. This ellipse has its own local 2D coordinate system with coordinates x and y.

2.2.4. Load on whole bearing

Now that the individual contact loads are computed, it is possible to calculate the global load that acts on the bearing in order to obtain the given displacement X. For clarity, the element loads are split into a radial and axial component

$$Q_r = Q \cos(\alpha) \tag{2.25}$$
$$Q_y = Q \sin(\alpha) \tag{2.26}$$

$$F = \begin{bmatrix} F_x \\ F_y \\ F_z \\ M_x \\ M_z \end{bmatrix} = \begin{bmatrix} \sum Q_r \sin(\psi) \\ \sum Q_y \\ \sum Q_r \cos(\psi) \\ \sum -Q_y \frac{p_r}{2} \cos(\psi) - Q_r \frac{p_y}{2} \cos(\psi) \\ \sum Q_y \frac{p_r}{2} \sin(\psi) - Q_r \frac{p_y}{2} \sin(\psi) \end{bmatrix} \tag{2.27}$$

Now that the global loads on the bearing are known an optimization is used to find the value of the displacement vector X such that the global load equals the desired load case.

2.2.5. Verification of rigid bearing model

In the rigid bearing model proposed in section 2.2, the Hertzian contact model was used to calculate the load distribution over all the rolling elements. A load case F is the input of the model, and an optimization algorithm tries to find a displacement vector X that produces a force equal to the load case. The outputs are the individual loads on all the rolling elements and their contact angles. This model will be verified by comparing the load distribution against a simulation performed in SKF SimPro Expert.

SimPro is a simulation tool from SKF that uses multi-body physics together with a component mode synthesis algorithm to calculate the load and contact angle on each

rolling element, and it is often used in SKF to simulate bearings. The inner and outer ring will be kept rigid in order to compare it to the proposed model, and the only deformation that takes place is in the rolling element contacts, which are modeled with Hertzian contacts. The rigid bearing model and SimPro will both model the SKF BAR0162 HBU3 bearing unit. The following load is applied to the bearing:

$$F = \begin{bmatrix} 5000\,\text{N} & 0 & 0 & -1000\,\text{N}\,\text{m} & 0 \end{bmatrix}^T \tag{2.28}$$

Figure 2.7 shows the load acting on each rolling element and the corresponding contact
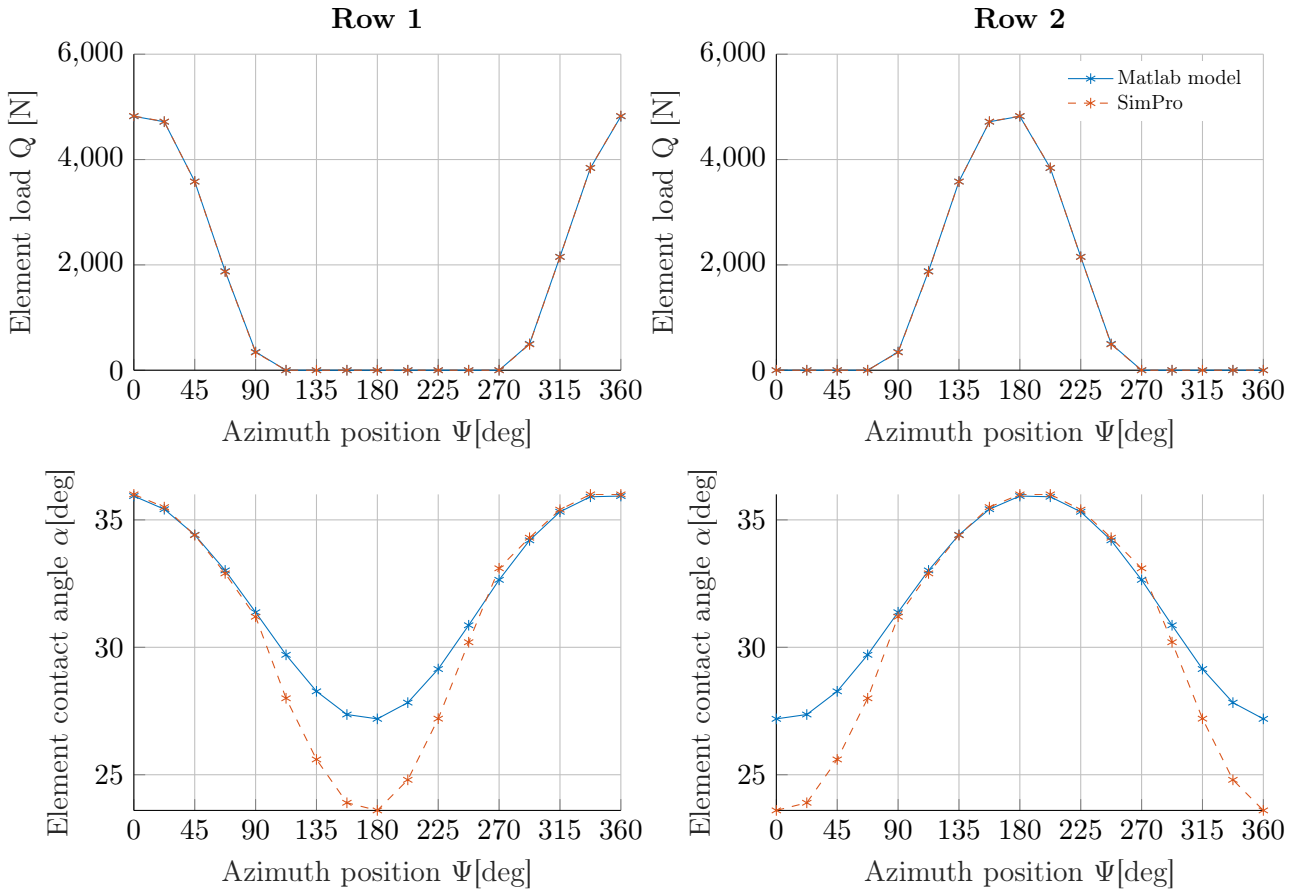
Figure 2.7: Comparison of the rigid bearing model to SKF SimPro Expert. Both assume a rigid inner and outer ring. Note that the rolling elements on row 1 between azimuth 90° and 270° are unloaded. This means that the contact angles on this interval are not relevant. The same applies to the rolling elements in row 2 outside the interval.

angles calculated in both SimPro and the model. Note that only the contact angles of the rolling elements in the loaded zone are relevant since the other rolling elements are just loose in the bearing with no load, thus their contact angle is not of interest. The

loaded zone of row 1 goes from 90° to 270°, while the loaded zone of row 2 is outside this interval.

Both the rigid bearing model and the SimPro simulations were run for an HBU3 bearing. It can be seen in the plots that the loads calculated with the rigid bearing model follow the SimPro model very closely. The largest error of the estimated loads is less than 1.9 %. The contact angles of the ball bearing are also very accurate, with the largest difference being 1.5 %. From this comparison, it can be observed that the rigid bearing model performs very good. The load distribution is estimated very accurately with the rigid bearing model in comparison with the SimPro software.

2.2.6. VERIFICATION OF HERTZIAN CONTACT MODEL

Many FEA data is generated for the construction of the raceway deformation model and the strain model. These FEA simulations are modeling an outer ring with a rolling element on which a load is applied. The most realistic way to model this in FEA is to create a sphere, that represents the ball, and apply a load to it. This sphere is then constraint to the outer ring via a contact. The problem with this is that these contact constraints are highly nonlinear and need a very fine mesh, meaning that it is not robust and is time-consuming to solve [17]. A much faster way to model the rolling element is to calculate the size and stress distribution of the contact ellipse with the Hertzian contact model. In this section, we will look at the performance of this Hertzian contact model by comparing it in FEA against a realistic ball in contact with the raceway.

The rolling elements in the bearing are in contact with the raceway, and there is an interaction of forces between these parts. The accurate, but time-consuming, contacts are preferably replaced with other loads in accordance with the principle of Saint-Venant:

If the forces acting on a small portion of the surface of an elastic body are replaced by another statically equivalent system of forces acting on the same portion of the surface, this redistribution of loading produces substantial changes in the stresses locally but has a negligible effect on the stresses at distances which are large in comparison with the linear dimensions of the surface on which the forces are changed.[18]

Since the outer ring is relatively thin, it is unknown if the principle of Saint-Venant holds for this case. A study is therefore done to find out whether the rolling element can be replaced by a load distribution that is applied to a surface that has the shape of an ellipse as defined in the Hertzian contact model. The load distribution on this ellipse is defined by equation 2.24.

A simplified model of an HBU3 bearing is built. Since this model is symmetric, only a

half bearing is made with a symmetry-constraint on the plane that divides the model in half. A sphere is placed at $\psi = 0$ in row 1 against the raceway to represent the rolling element, and it is constraint with a contact to the raceway. Figure 2.8 shows
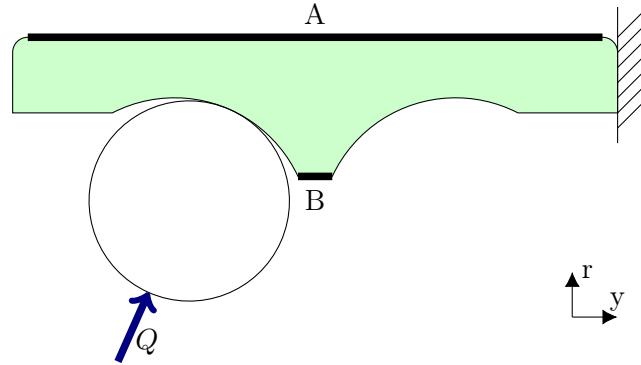

Figure 2.8: Schematic of the 3D FEA model used to verify the Hertzian contact model. A single rolling element in row 1 is loaded with Q, while the outer ring is fixed on its outboard edge. The von Mises stresses on edges A (outer surface) and B (raceway shoulder) of the results are compared to each other.

a schematic of the model set up in FEA. A load of $10.7\,\mathrm{kN}$ is applied at a contact angle of $38.2°$. These loads and contact angle are realistic values for a bearing with a large moment acting on it. The corresponding Hertzian contact ellipse size and load distribution are calculated for the model with the rigid bearing model. The boundary on the right side is fixed. The edges A (outer surface) and B (raceway shoulder) will be used to compare the results.

A fine mesh is used for both simulations to ensure that the discretization of the model does not significantly influence the results. The model with the ball in contact took $1420\,\mathrm{s}$ to solve while the model with only the Hertzian contact took $53\,\mathrm{s}$, which already shows the need for removing the rolling element with the contact constraint. The von Mises stresses from both results are compared to each other, because these are independent of the direction of the stresses. Figure 2.9 shows what the von Mises stresses are in the modeled outer ring and rolling element. The colors range up to a stress of $200\,\mathrm{MPa}$. This is not the maximum stress in the image, as the stress in the contact is much higher. With this color range, it is possible to see what the stress is on the outer surface of the outer ring.

The von Mises stresses on edge A and B are shown in figure 2.10. On edge A, the difference between the two models is minimal. The largest error on A is $1.5\,\%$ at location $16.2\,\mathrm{mm}$. On edge B, the error is slightly larger, with an error of $3.9\,\%$ at $0\,\mathrm{mm}$, but the error decreases rapidly further along the edge. The beginning of this edge is located $1.5\,\mathrm{mm}$ away from the edge of the contact area, thus it is not surprising that this is not entirely accurate. It is also impossible to place strain gauges this close to the edge of the raceway shoulder, so this will not be a problem. It can be
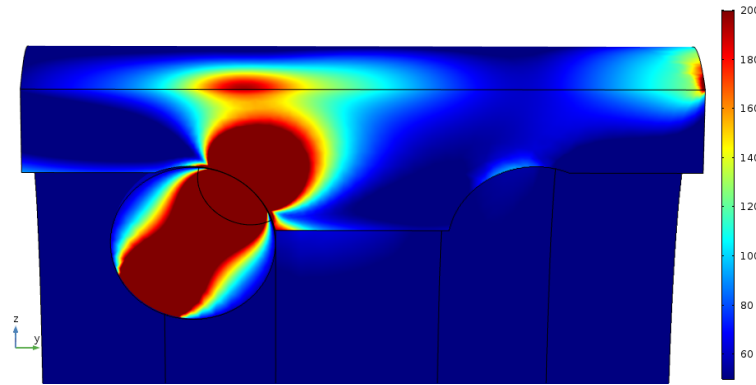
Figure 2.9: The von Mises stresses (MPa) in the outer ring and rolling element. The color scale ranges up to 200 MPa, while the stresses near the contact are much higher. With this range it is possible to see how the load affects the stresses on the surface of the outer ring. The outer ring is constrained on the right side, causing local stresses at the right.
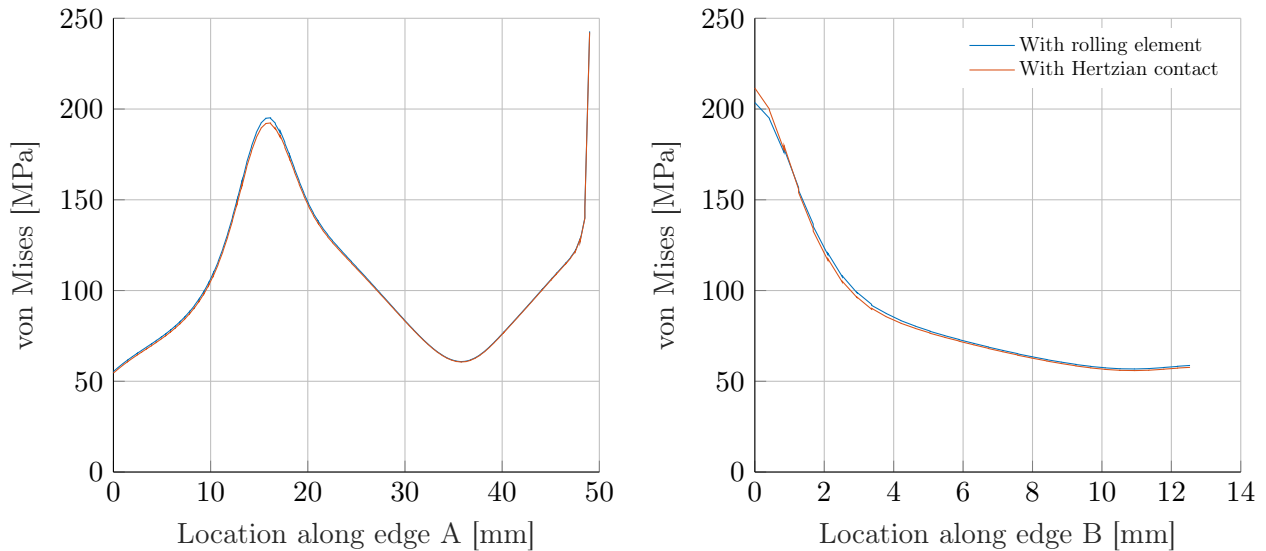

Figure 2.10: Von Mises stress (MPa) along the edges as calculated with the FEA. One FEA is modeling an outer ring and a rolling element in contact with each other. The other is just an outer ring with a load distribution applied to an ellipse-shaped contact area, as modeled with the Hertzian contact theory. Edge A is on the outer surface, and edge B is on the raceway shoulder.

concluded that the Hertzian contact model performs very good as a substitute for a rolling element with a contact constraint in the FEA modeling, thus making the simulations significantly faster and more robust.

2.3. Raceway deformation model

The loads on all the rolling elements are calculated with an analytical model that assumes a rigid outer ring. In reality, the outer ring of the HBU3 bearing is relatively thin so it will deform significantly. A semi-analytical model is proposed based on generated FEA data to model this deformation. Figure 2.11 shows a schematic of
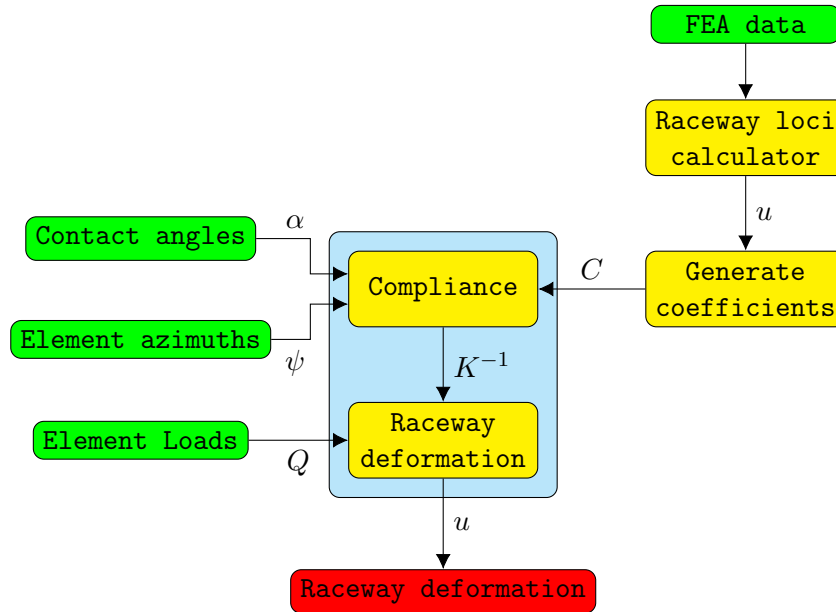

Figure 2.11: Schematic overview of the raceway deformation model. Coefficients of the Fourier series and Chebyshev polynomials are generated from the FEA data once. The model calculates the deformation of both raceways as a function of the location of the rolling elements, their contact angles, and loads.

what this model looks like. A set of coefficients C is calculated from the FEA data. This step is done once after the FEA data is generated. After this, the FEA data is not needed anymore when the Raceway Deformation Model (RDM) is used. Input for this model are the contact angles and element loads that are calculated in the rigid bearing model, and the azimuth of each element, which is an input in the whole model. The analytical rigid bearing model looks at the location of the raceway locus in order to determine the deformation of each Hertzian contact. This locus is a virtual line that represents the center of the raceway. The displacements of the locus, u_r and u_y, are determined in the proposed RDM and are added in equations 2.7 and 2.8. The deformation of the outer ring is captured in the displacement of these loci.

This section will explain how the coefficients and compliance matrix K^{-1} are calculated in order to determine the raceway deformations.

2.3.1. Extracting the location of the raceway loci from FEA

The raceway locus will be extracted from the FEA data. The problem with this locus is that it is not a physical location in the outer ring so it can not be easily extracted from the FEA. This means that it needs to be estimated based on the location of the other points in the outer ring. This subsection gives the algorithm used to determine the location of these loci. Figure 2.12 shows the points used in a cross-section of one raceway.
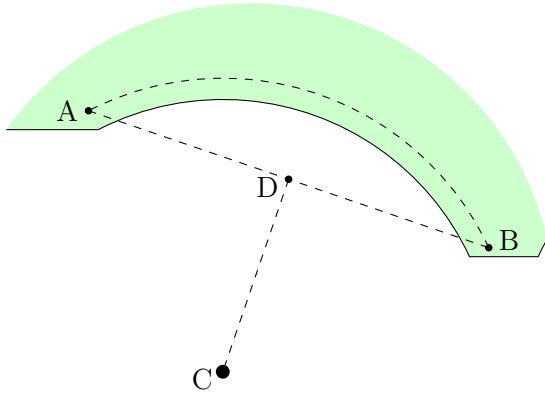
(a) Undisplaced location of the outer raceway locus. Assumed is that all these point are rigidly fixed to each other.

(b) Animation of the displaced location of the outer raceway locus due to an element load Q. Note how all the points move and stay fixed with respect to each other. (The animation only works in Adobe Reader.)

Figure 2.12: Location of the outer raceway locus, C. This is not a physical location in the outer ring and can therefore not be extracted from the FEA. Assuming a fixed location of C with respect to A and B, the locus can be estimated from these points in the FEA.

The points of the undeformed raceway are shown in figure 2.12a, and the corresponding locations of the points of the deformed raceway due to a load Q are shown in figure 2.12b. The raceway locus is represented by point $\hat{C}$. Points $\hat{A}$ and $\hat{B}$ are extracted from the FEA and used to calculate the location of $\hat{D}$, which is precisely in the middle of $\hat{A}$ and $\hat{B}$

$$\hat{D}_i = \frac{\hat{A}_i + \hat{B}_i}{2} \tag{2.29}$$

where $i = r, y$ for radial and axial direction. The displacement and rotation of $\hat{D}$ are then calculated

$$d_i = \hat{D}_i - D_i, \qquad \gamma = \tan^{-1}\left(\frac{\hat{B}_r - \hat{D}_r}{\hat{B}_y - \hat{D}_y}\right) - \tan^{-1}\left(\frac{B_r - D_r}{B_y - D_y}\right) \tag{2.30}$$

Assumed is then that the distance between C and D does not change, or

$$l^2 = (C_r - D_r)^2 + (C_y - D_y)^2, \quad \text{and} \quad l = \hat{l} \tag{2.31}$$

The line $\hat{C}$-$\hat{D}$ is orthogonal to the line $\hat{A}$-$\hat{B}$. Using these equations then gives the location of the raceway locus

$$\begin{bmatrix} \hat{C}_r \\ \hat{C}_y \end{bmatrix} = \begin{bmatrix} \hat{D}_r \\ \hat{D}_y \end{bmatrix} + \begin{bmatrix} -\frac{C_y - D_y}{C_r - D_r} \\ 1 \end{bmatrix} \frac{l \sin(\gamma)}{\sqrt{1 + \left(\frac{C_y - D_y}{C_r - D_r}\right)^2}} \tag{2.32}$$

With the new location of the raceway loci known the displacement of the loci is

$$u_i = \hat{C}_i - C_i \tag{2.33}$$

The choice for the location of A and B influences the accuracy of the estimation of the raceway loci location. High accuracy for a large part of the azimuth can, on the one hand, be achieved by choosing a location of A and B close to the surface of the raceway and close to the middle (i.e., close to the nominal contact angle of 38°). On the other hand, it is crucial to ensure that the local deformation of the element load is not measured since this local deformation is already accounted for in the nonlinear Hertzian contact model. Points A and B are chosen at $2\,\mathrm{mm}$ from the surface at the edges of the raceway. The local effects due to the contact deformation do not influence these points much.

2.3.2. Interpolating the raceway deformation
Now that the deformation of the raceway is extracted from the FEA data a model will be constructed that calculates the raceway loci displacements for a single load that is applied to the outer ring via the rolling elements. These deformations are interpolated using Fourier and Chebyshev polynomials. Via the superposition principle, the deformations due to every single load will be combined to get the total deformation of the outer raceways. These deformations can then be led back into the rigid bearing model to calculate the redistributed rolling element loads for this deformed state. The main concept of the model proposed by [19] is used, and improved to calculate the displacements of the raceway loci.

The model of [19] is a simplified model of a bearing designed to be very fast so that it can be used in an unscented Kalman filter (UKF) at the cost of accuracy. The model uses FEA data generated at only one contact angle. This makes the state observer and the generation of the FEA data fast, but small deviations of a few degrees from this single contact angle increases the error of the deformation. FEA done by SKF shows that the contact angles range from 33.4° to 52.3°, so using FEA data for a single contact angle is not sufficient for our application as will be discussed in subsection 2.4.2. The FEA data will simulate different contact angles ranging from 33.4° to 52.3°, and the raceway deformation model will incorporate these various contact angles. The model of [19] also only uses the radial component of the raceway deformation. While this is ideal for a fast state observer, it is not very accurate since the axial deformation is of the same order of magnitude as the radial deformation and it is therefore chosen

to use both directions. Finally, the mode of [19] extracts the deformation of a single point in the outer ring between the raceways and assumes this to be the raceway deformation u_r. While again this makes the UKF fast, FEA shows that this is not very accurate, thus in the proposed model, it is chosen to estimate the true deformation of the raceway loci as shown in subsection 2.3.1.

A total of 8 raceway deformation models are made; one for each of the possible combinations of

Deformed row There are two rows, which both deform.

Deformation directions The deformation is split into a radial and axial component.

Loaded row Both rows have loaded rolling elements, which affect the deformation of their own row, but also the other.

For the sake of clarity, only the deformation in a single direction of only one raceway will be considered. The construction of all the deformations are made in the same way.

The outer ring is modeled as any spring is modeled:

$$u(\psi) = K^{-1}(\psi, \Psi, \alpha)Q(\Psi, \alpha) \tag{2.34}$$

In this case, however, the compliance (i.e., inverse stiffness) K^{-1} is a nonlinear value that relates the deformation u of the outer ring on arbitrary azimuth position ψ to the load Q of a single rolling element which is located at azimuth Ψ and contact angle α. An example of what this compliance function looks like can be seen in figure 2.13. This plot shows how the compliance is a function of the azimuth of the deformation ψ, and the azimuth of the applied load. It is also dependent on the contact angle α, but this value is fixed in the plot to 43.4°. The deformation per load on the same azimuth where the load is applied (i.e., $\psi = \Psi$) is the highest, although the raceway also deforms for other azimuths. The influence of the shape of the outer ring can be seen in this plot. Around azimuths 40°, 140°, 200°, and 340° the outer ring has bolt holes, as later can be seen in section 2.5. These are very stiff and thus ensure a low compliance of the raceways. The deformation is extracted from the FEA data. Note that it is assumed that the deformation is linear with the applied load in accordance with the superposition principle since the stresses in the outer ring operate in the linear elastic range. The compliance is defined as:

$$K^{-1}(\psi, \Psi, \alpha) = \boldsymbol{\varphi}(\psi)\boldsymbol{\Theta}(\Psi, \alpha) \tag{2.35}$$

which is composed of the predefined compliance shapes $\boldsymbol{\varphi}$ and the corresponding compliance approximation $\boldsymbol{\Theta}$. This is like a Fourier series where $\boldsymbol{\varphi}$ contains the set of sines and cosines and $\boldsymbol{\Theta}$ consists of the coefficients. In this case, the coefficients are not constant but vary as a function of Ψ and α. The compliance shapes are defined as:

$$\boldsymbol{\varphi}(\psi) = \begin{bmatrix} \sin(m\psi)_{m=0} & \cos(m\psi)_{m=0} & \cdots & \sin(m\psi)_{m=M-1} & \cos(m\psi)_{m=M-1} \end{bmatrix} \tag{2.36}$$
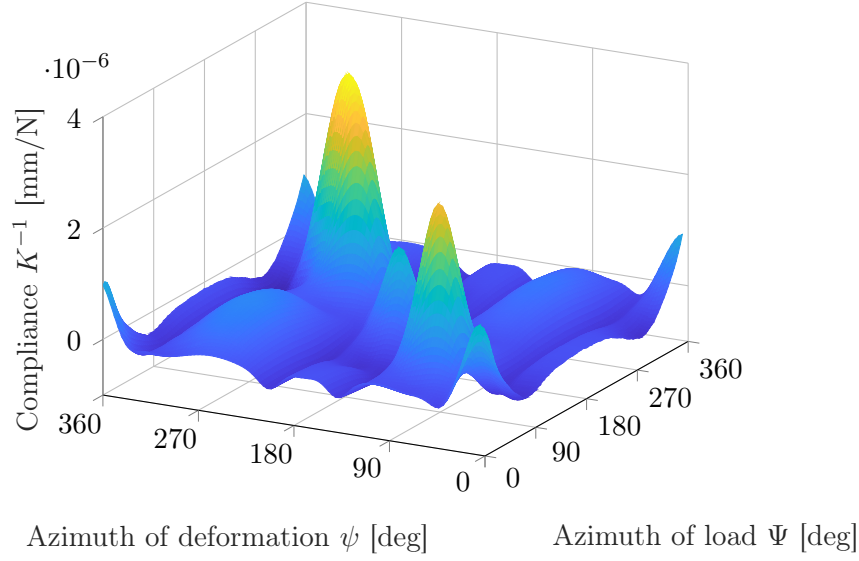
Figure 2.13: The radial compliance K^{-1} of row 1 due to a load at a contact angle of 43.4° at the same row. This compliance is a function of the contact angle α, the azimuth of the deformation ψ, and the azimuth of the applied load Ψ. As can be expected, this plot shows that the deformation per load on a specific azimuth is the highest when the load is applied to the same azimuth. However, the raceway also deforms when these azimuths are not in the same place, albeit less.

As mentioned in [19], the advantages of using sines and cosines with a period of $m\psi$ are that they are orthogonal and continuous along the whole azimuth of the outer ring. The number of shapes can be chosen by selecting a value for M.

The compliance approximation is a vector column vector with all the compliances of the corresponding shapes:

$$\mathbf{\Theta}(\Psi, \alpha) = \begin{bmatrix} \theta_1(\Psi, \alpha) \\ \vdots \\ \theta_{2M}(\Psi, \alpha) \end{bmatrix} \tag{2.37}$$

The FEA data is used to calculate the radial deformation along the outer ring for predetermined element loads. Since the compliance shapes are also known, it is possible to calculate the compliances on location Ψ and contact angle α when combining equations 2.34 and 2.35. A least-squares method is used to find a single solution of θ_m such that:

$$\min \sum_{\psi} \left(\theta_m(\Psi, \alpha) \boldsymbol{\varphi}_m(\psi) Q(\Psi, \alpha) - u(\psi, Q(\Psi, \alpha)) \right)^2 \tag{2.38}$$

There are a total of $2M$ compliance approximations θ_m which in turn are dependent on the load location and contact angle. The load locations and contact angles are discretized due to the FEA data, but a continuous function is required. To do this a combination of Fourier series and Chebyshev polynomials is used with which it is

possible to interpolate the 2D datasets θ_m. A modified version of the method presented in [20] is used for this interpolation. The following function is used to estimate a continuous θ_m:

$$\theta_m(\Psi, \alpha) = \sum_{k=1}^{(2M)} \sum_{w=1}^{(W)} c_{k,w} \omega_{\Psi,k}(\Psi) \omega_{\alpha,w}(\hat{\alpha}) \tag{2.39}$$

Here $c_{k,w}$ are the coefficients and $\omega_{\Psi,k}$ and $\omega_{\alpha,w}$ are the Fourier and Chebyshev functions, which are valid on the domains $[0, 2\pi]$ and $[-1, 1]$. This means that the contact angles α need to be normalized to this domain of $[-1, 1]$. These normalized contact angles we call $\hat{\alpha}$. The Fourier function $\omega_{\Psi,k}$ is

$$\omega_{\Psi,k} = e^{-ik(\Psi-1)2\pi/360} \tag{2.40}$$

with the index k going from 1 to $2M$, and Ψ in degrees. All these functions are placed into the matrix Ω_Ψ. The Chebyshev functions have W shapes and are defined as

$$\begin{aligned} \omega_{\alpha,1} &= 1 \\ \omega_{\alpha,2} &= \hat{\alpha} \\ \omega_{\alpha,w} &= 2\hat{\alpha}\omega_{\alpha,w-1} - \omega_{\alpha,w-2} \end{aligned} \tag{2.41}$$

here the index w goes from 1 to W. These Chebyshev polynomials are placed into the matrix Ω_α.

To calculate the coefficients $c_{k,w}$, we will treat equation 2.39 as an $\mathbf{Ax} = \mathbf{B}$ problem. For this, the coefficients $C_{k,w}$ will be placed into the matrix C, which has one column with a total length of $2MW$. In our case we get the following system of linear equations:

$$\Omega C = \Theta_m \tag{2.42}$$

Θ_m is a column vector with a total length of the number of FEA simulations done, containing all the values of θ_m for only one m. The Fourier and Chebyshev functions are computed for all the possible values of Ψ and α at which the load is applied. The Kronecker product of these functions is then used to construct Ω:

$$\Omega = \Omega_\Psi \otimes \Omega_\alpha = \begin{bmatrix} \omega_{\Psi_1,1}\Omega_\alpha & \omega_{\Psi_1,2}\Omega_\alpha & \cdots & \omega_{\Psi_1,2M}\Omega_\alpha \\ \omega_{\Psi_2,1}\Omega_\alpha & \omega_{\Psi_2,2}\Omega_\alpha & \cdots & \omega_{\Psi_2,2M}\Omega_\alpha \\ \vdots & \vdots & \ddots & \vdots \\ \omega_{\Psi_N,1}\Omega_\alpha & \omega_{\Psi_N,2}\Omega_\alpha & \cdots & \omega_{\Psi_N,2M}\Omega_\alpha \end{bmatrix} \tag{2.43}$$

With Ω and θ_m known it is now possible to calculate the coefficients C_m. When θ_m is to be calculated, a new matrix Ω should be constructed for the desired locations Ψ and contact angles α. This is a continuous function, so with equation 2.42 it is possible to

calculate θ_m for any location. The deformation then becomes

$$
\begin{bmatrix} u(\psi_1) \\ \vdots \\ u(\psi_i) \end{bmatrix} = \begin{bmatrix} \boldsymbol{\varphi}(\psi_1) \\ \vdots \\ \boldsymbol{\varphi}(\psi_i) \end{bmatrix} \begin{bmatrix} \boldsymbol{\Theta}(\Psi_1, \alpha_1) \cdots \boldsymbol{\Theta}(\Psi_j, \alpha_j) \end{bmatrix} \begin{bmatrix} Q(\Psi_1, \alpha_1) \\ \vdots \\ Q(\Psi_j, \alpha_j) \end{bmatrix} \tag{2.44}
$$

Here the deformation is calculated at all i locations. When using this raceway deformation model in conjunction with the rigid bearing model to calculate the load distribution of the rolling elements, the location at which the deformation is calculated is equal to the position of the rolling elements, i.e., $\psi = \Psi$. The creation of this model is done for both radial and axial deformation of both rows due to loads that are applied to both rows. This gives a total of 8 sets of coefficients C. One of the assumptions of the model is that the superposition principle can be applied to the elastic outer ring. This will be verified using an FEA with a simple load case with a few rolling elements.

2.3.3. AMOUNT OF FOURIER AND CHEBYSHEV MODES

Now that the model has been constructed, it is used to analyze certain parts of it. To start, the coefficients of θ for all the modes of the radial compliance K^{-1} of row 1 due to any load on row 1 are plotted in figure 2.14. This is the same compliance function that is depicted in figure 2.13 that was shown earlier. Note that every single Fourier or Chebyshev polynomial is called a mode. The coefficients of the first three w-modes, the first 15 k-modes and the first 30 m-modes are shown. It can be seen that if speed is important, for instance, when using this model in a state observer, the modes can be limited to about 2 w-modes, 10 k-modes, and 20 m-modes. This is the case for all θ. An interesting artifact is present around the $k = 2m$ line, where the coefficients are highest. To understand why this is happening, we need to look at the shapes of the compliance function, which are shown in figure 2.13. The compliance [mm/N] is shown as a function of the azimuth along the loaded row and the azimuth of the load itself. This compliance in the other direction and on the second row and for different contact angles has a similar shape, but for simplicity, only this case is demonstrated. The shape of the graph is somewhat symmetric along the $\psi = \Psi$ line. When looking at the compliance shapes as defined in equation 2.36, it can be seen that the frequency of each m mode is

$$
f\{\boldsymbol{\varphi}\} = [0, \quad 0, \quad \psi, \quad \psi, \quad 2\psi, \quad 2\psi, \quad \cdots \; (M-1)\psi, \quad (M-1)\psi] \tag{2.45}
$$

while the frequency of each k-mode of the compliance approximation is

$$
f\{\Omega_\Psi\} = [0, \quad \psi, \quad 2\psi, \quad \cdots, \quad (M-1)\psi] \tag{2.46}
$$

This means that the frequency for each 2 m-modes are equal to the frequency for each k-mode. Since the shape of the compliance for each contact angle is somewhat
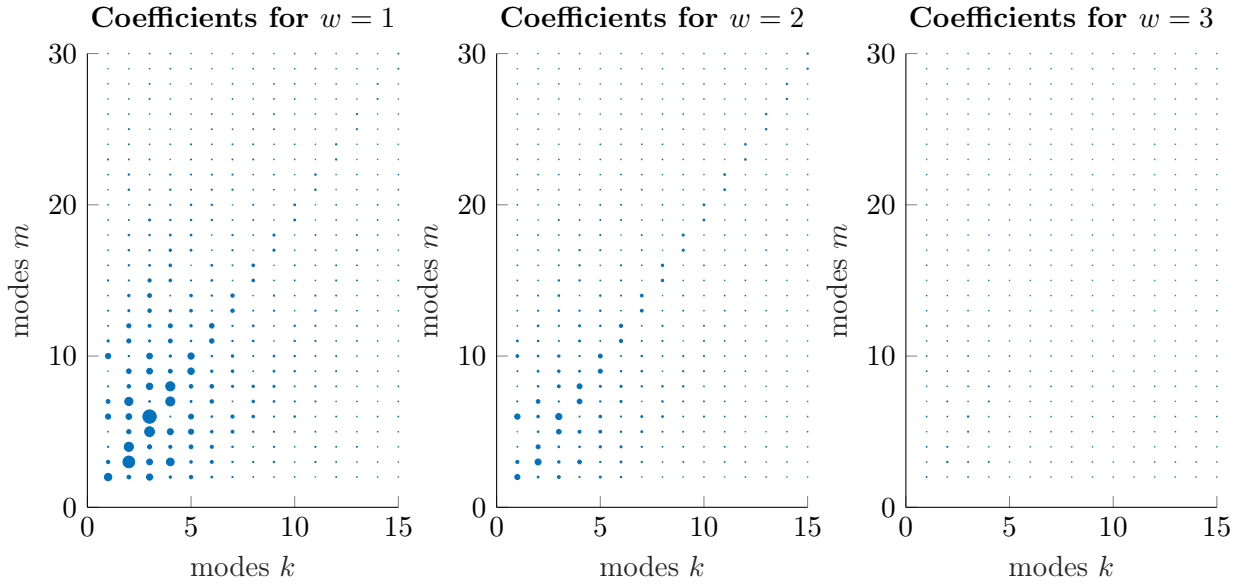
Figure 2.14: The coefficients C of θ for the radial deformation of row 1 due to any load on row 1. The size of the dots represents the size of C. Only 2 w-modes, 10 k-modes, and 20 m-modes are needed to increase the speed of the model while maintaining high accuracy. The highest modes can be found around the $k = 2m$ line.

symmetric, it is expected that the coefficients C, as shown in figure 2.14, are indeed highest around the $k = 2m$ line.

A Singular Value Decomposition (SVD) is made of the same compliance to analyze the order of the system. Plots of this SVD can be found in appendix B where the normalized singular values, left-singular vectors, and right-singular vectors are shown. The normalized singular values show what part of the variance in the compliance is accounted for in that mode. All the singular values and corresponding modes are ordered from large to small. The left-singular vectors are orthonormal modes of the raceway compliance, and the right-singular vectors indicate how much each mode is activated due to the load position, which we will call mode dynamics. The modes look very similar to the corresponding mode dynamics. This is expected as the compliance is almost symmetric. Another interesting phenomenon that occurs is that from mode 8 and higher, the singular values seem to appear in pairs. This is not caused by the symmetry in the compliance, but due to the fact that the physical outer ring itself is symmetric around the Cartesian xy-plane. Each pair of modes is mirrored to each other. If the FEA data was made with the outer ring attached to a nonsymmetric knuckle, these pairs would not be observed. There is no clear separation in the singular values that distinguishes the noise from the rest of the modes.

An option to reduce the model size might be to 'rotate' the compliance in such a way that it becomes not a function of the location of the deformation, but a func-

tion of the phase between the deformation location and the applied load. Figure 2.15 shows what this looks like. The SVD of this function is shown in appendix C. As
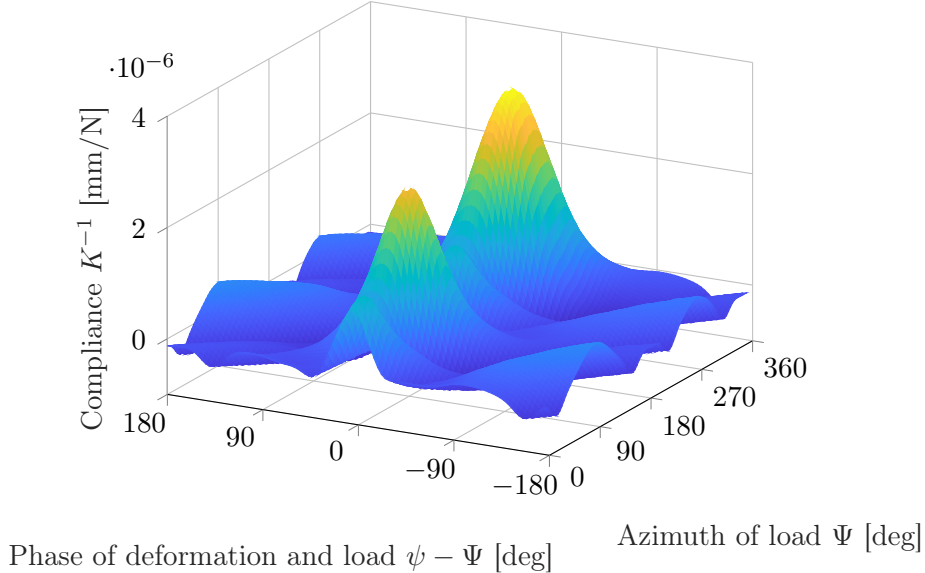

Figure 2.15: The rotated radial compliance K^{-1} of row 1 due to a load at a contact angle of 43.3° at the same row. This is different from the compliance function shown in figure 2.13. In this case, the y-axis does not represent the location of the deformation, but the phase between the location of the deformation and the load. This function is somewhat symmetric along the $\psi - \Psi = 0$ line.

expected, the first few modes cover more of the variance than the first modes of the default compliance. Also, most modes are symmetric or anti-symmetric. The first 32 cumulative singular values of both compliances are plotted in figure 2.16. Here it can be seen that only with three modes of the singular value decomposition the rotated compliance covers more variance than the default compliance. Other than that both show similar performance, so in the RDM the default compliance,which is a function of the azimuth of the load and the azimuth of the deformation, will be used. Keep in mind that the modes of the singular value decomposition are not the same as the Fourier and Chebyshev polynomials. These SVDs give insight in what elements of the bearing dictate the compliance function. The symmetric shape of the outer ring can be found back in the symmetric modes of the SVD of the default compliance. The 'rotated' compliance shows somewhat symmetric behavior around the loaded azimuth (i.e., The deformation is fairly similar for $\psi - \Psi = \Psi - \psi$).

2.3.4. VERIFICATION OF THE RDM
With the RDM being built, it is essential to know if it works. Before verifying the whole model with the BETSY rig, an FEA simulation is done for a specific load case
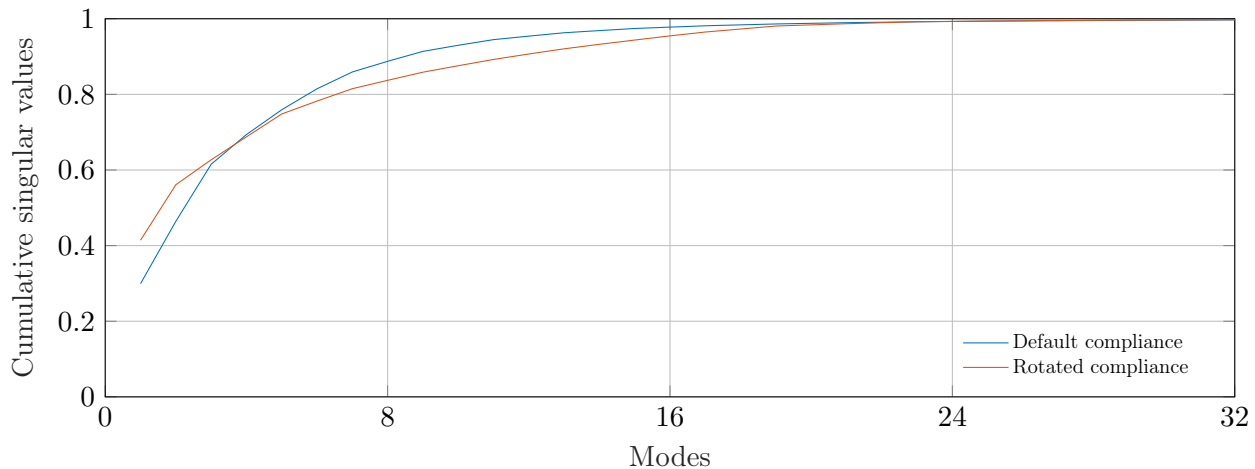
Figure 2.16: Cumulative singular values of the default compliance and rotated compliance. This gives an indication about which compliance function can best be used. For more modes, it seems best to use the compliance function in default orientation.

in order to check whether the RDM works appropriately. This load case is shown

Quantity	Value	Unit
F_x	-73	N
F_y	852	N
F_z	13150	N
M_x	-312	Nm
M_z	249	Nm

Table 2.1: The forces applied to the bearing for the comparison between the FEA and the proposed model.

in table 2.1. The individual forces on each rolling element can be seen in appendix D. The raceway deformation calculated with both the FEA and RDM in both radial and axial direction of both rows are plotted in figure 2.17. The RDM seems to work properly as the errors are small. The maximum error for each plot is shown in table 2.2.

RMSE	Row 1	Row 2
Radial	2.82 %	3.93 %
Axial	1.96 %	1.93 %

Table 2.2: The maximum errors of the deformation for the load case used to verify the raceway deformation model. The corresponding plots can be seen in figure 2.17.

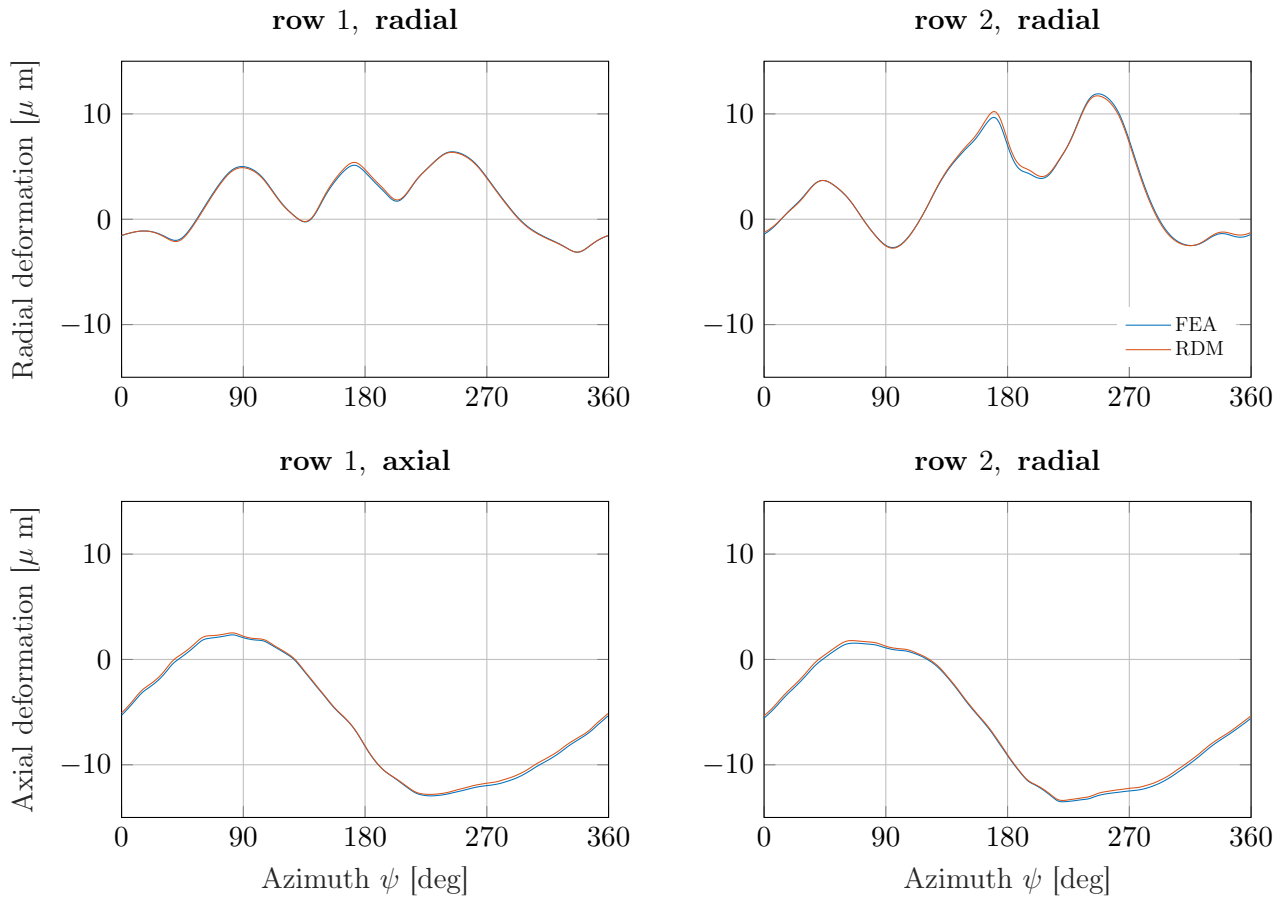The effect of the RDM on the load distribution over all the rolling elements can also

Figure 2.17: The radial and axial deformations of the raceways, as calculated by the FEA and RDM for a load case, in which 23 of the 32 rolling elements are loaded. The difference between the two models is very small.

be analyzed. This is done by applying the same load case to the bearing. This is done for different positions of the rolling elements to get a continuous shape of the loaded zone. The shape of this loaded zone with and without the RDM is shown in figure 2.18. Without RDM the loads on all the balls are determined with only the rigid bearing model, which assumes a rigid outer ring. The RDM is constructed for the bearing that is also used for the validation in chapter 3. This bearing has very stiff flanges around the bolt holes that fix the bearing to the knuckle. The locations of these bolts are around azimuths 40°, 140°, 200°, and 340°. This can be seen in the plot of the loaded zone with the RDM enabled. The loads on the location of the bolts are higher due to the increased stiffness. For this load case, a change of up to 9.1 % can be observed due to the RDM, which is a significant difference. This shows that only a rigid bearing model is not sufficient in calculating the load distribution, and
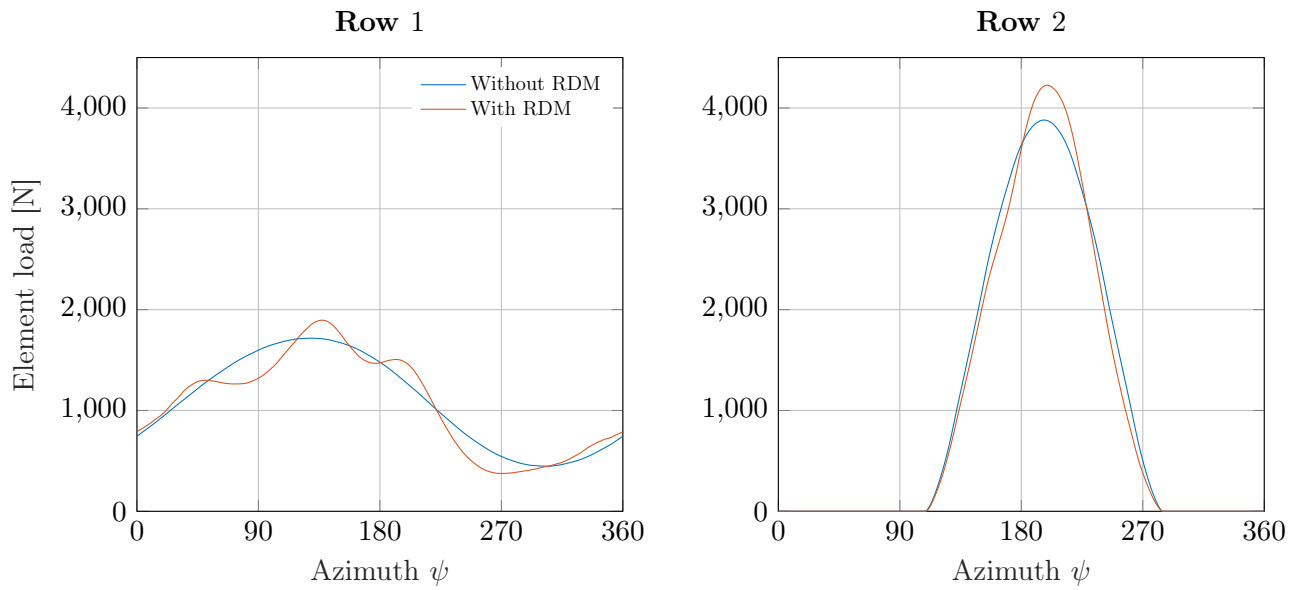
Row 1   **Row** 2

Figure 2.18: The load of the rolling elements on each position ψ for a specific load case modeled with and without the raceway deformation model (RDM). Around azimuths 40°, 140°, 200°, and 340° the load increases with the RDM. This is caused by the increased stiffness due to the bolt holes which are located at these azimuths.

the raceway deformation model is needed to make a better estimate.

2.4. STRAIN MODEL

The load, location, and contact angle of each rolling element have been calculated with the rigid bearing model in combination with the raceway deformation model. The goal of the whole model is to simulate strains on the outer surface of the bearing. In order to achieve this, a separate strain model is used to calculate these strains. Figure 2.19
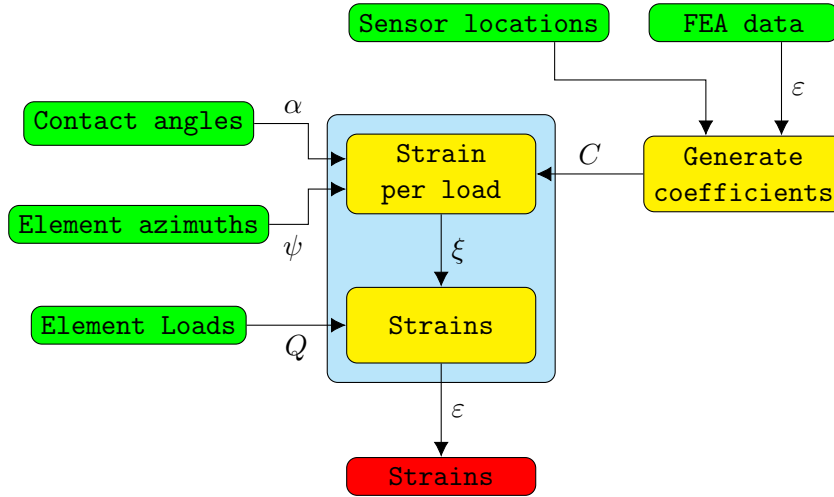
Figure 2.19: Schematic overview of the strain model. Coefficients for the Fourier and Chebyshev will be generated from the FEA data. The difference between this strain model and the RDM is that with this model the strain per load is calculated only for each predefined sensor location, as opposed to the compliance function of the RDM which is calculated for the whole continuous raceway. The strain is a function of the element loads, contact angles, and azimuths.

shows an overview of how this strain model works. The strains are the derivatives of deformation, thus this model can be built in a similar way as the RDM, with the exception that the strains are not described for the whole bearing but only for specified sensor locations. These could be the locations on which the strain gauges are placed. As with the RDM, the coefficients C have to be calculated only once for each sensor location. Once this is done, the FEA data is not needed anymore, provided that the model is not needed for other sensor locations.

2.4.1. INTERPOLATING THE STRAINS

The interpolation of the strain on the surface of the outer ring is similar to the method shown in subsection 2.3.2. Equation 2.39 to 2.43 are used to construct the strain model. Only in this case, we will not use θ_m but a set of ξ that will be interpolated. This ξ represents the strain per load as a function of the location and contact angle of the rolling element, on different predetermined sensor locations. An example of what the strain per load looks like for a specific sensor can be seen in figure 2.20. For each sensor (i.e., strain gauge) the following equation is used to calculate the local strain
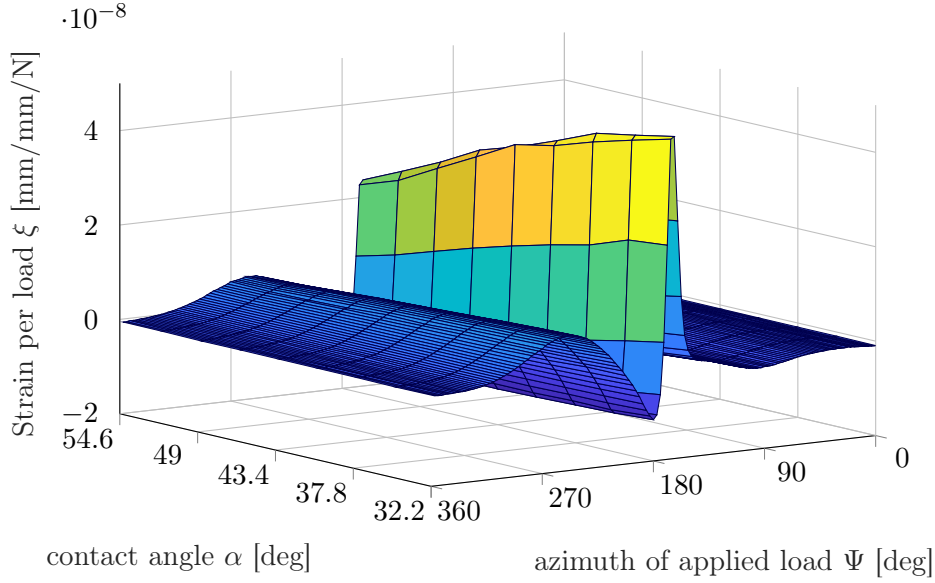
Figure 2.20: Strain data ξ for any load on row 2 and sensor at the bottom of the bearing ($\psi = 176°$). The strain per load is highest when the rolling element is exactly on the same azimuth of the sensor, while the strain becomes negative directly next to this location. This lot shows that the influence of the contact angle on the strain is significant.

due to each rolling element

$$\varepsilon = \xi Q \tag{2.47}$$

The equation for the continuous ξ becomes

$$\xi(\psi, \hat{\alpha}) = \sum_{k=1}^{(2M)} \sum_{w=1}^{(W)} c_{k,w} \omega_{\psi,k}(\psi) \omega_{\alpha,w}(\hat{\alpha}) \tag{2.48}$$

Here $\omega_{\psi,k}$ and $\omega_{\alpha,w}$ are of the polynomials, as shown in equations 2.40 and 2.41. The coefficients $c_{k,w}$ are calculated as described in the previous section. An example of the coefficients can be seen in figure 2.21. Here the same sensor is used as in the previous figure. This figure shows that if the model needs to be faster, only the first 3 w-modes and the first 45 k-modes can be used without a significant consequence in accuracy for this bearing type.

When transforming a continuous time signal into a discrete time signal, the sampling frequency of the continuous signal must be twice as high as the highest recorded frequency in the discrete signal, according to the Nyquist-Shannon sampling theorem. In the case of the bearing, the signal, which is the strain, is not a function of time, but of the azimuth of the load. This azimuth is a continuous signal that needs to be sampled into a Fourier series with the highest frequency at $\dfrac{45}{360°}$. This means that at
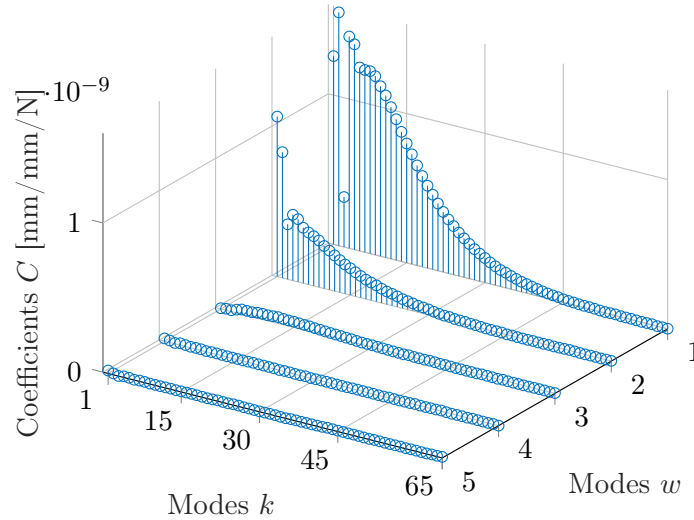
Figure 2.21: The coefficients C for Strain data ξ for sensor at the bottom of the bearing due to load on row 2. This shows that only the first three w-modes and first 45 k-modes to maintain full accuracy.

least 90 simulations along the azimuth are needed in order to be able to reconstruct this Fourier series.

2.4.2. Comparison of contact angle interpolation variations

SKF uses a detailed model in FEA of a BAR0282 bearing unit to simulate the strains on the outer ring. Analyses show that the contact angles in this bearing range from 33.4° to 52.3° for realistic load cases. Analysis with the proposed strain model show that FEA data needs to be generated for different contact angles on every azimuth.

Different variations of the strain model are compared to determine their accuracies. To generate the FEA data fast, ideally, all the simulations are done at only one contact angle of, for instance, 41°. The problem with this is that the model will be accurate around this contact angle, but as soon as the contact angle is much larger or smaller, the accuracy will drastically decrease. The variations of the model which are tested are:

Single contact angle The FEA data is generated with all the rolling elements on a fixed contact angle of 41°.

Single contact angle split into components Separate simulations are done in which the load from the rolling element is split up into a radial and an axial load.

Multiple contact angles on one location Again the FEA data is generated with all the rolling elements on a fixed contact angle, but this time some separate simulations are done on one azimuth location with multiple contact angles. From

these separate simulations, a gain is calculated for each contact angle and applied to each azimuth location.

Multiple contact angles on all locations The simulations are done with multiple contact angles on each azimuth.

All the variations of these models are made and compared to each other. A load case is used with a single element in the second row at azimuth position 270°. The contact angle is varied, and the resulting strain on the outer surface close to the rolling element is analyzed and compared to a validation FEA. The results can be seen in figure 2.22. Only the model that is constructed from FEA data generated at all contact angles at all azimuths gives an accurate result for contact angles far away from 41°, so therefore this variation is chosen to be used. This means that the number of FEA simulations will be multiplied by the number of contact angles that need to be simulated. This significantly increases the simulation time, but also the accuracy of the strain model.
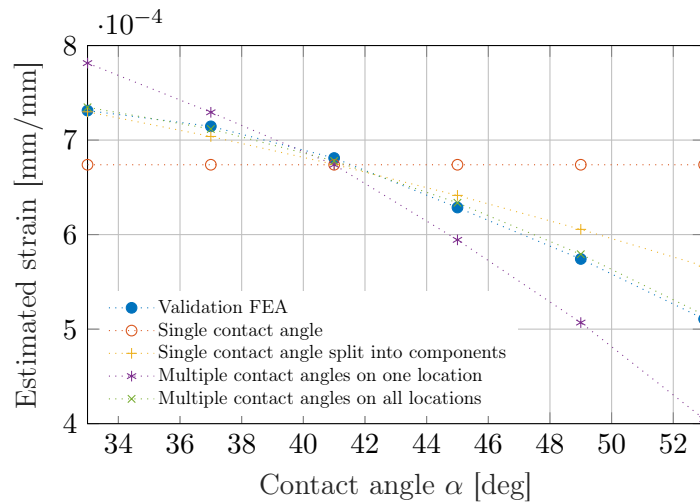

Figure 2.22: Estimated strain by different models for a single element with varying contact angles. Only the model that considers the contact angle on every azimuth is very accurate when compared to the validation FEA.

2.4.3. Influence of contact angle on strain signal

As mentioned in the introduction, the generation 1 algorithms try to estimate the loads on each individual rolling element. Often the signal is converted to the frequency domain in order to analyze the amplitude of the ball pass frequency. This is the frequency at which the rolling elements pass the sensor. This amplitude is called the first harmonic, H_1. The same can be done for twice the frequency, which is the second harmonic H_2. The strain model will be used to show the difference in signal due to a varying contact angle. Only the rolling elements in row 2 will be loaded with a force

of 7.5 kN while they rotate. The strain is sampled in two locations on the surface of the outer ring. These locations can be seen in figure 2.23. The first location is on the
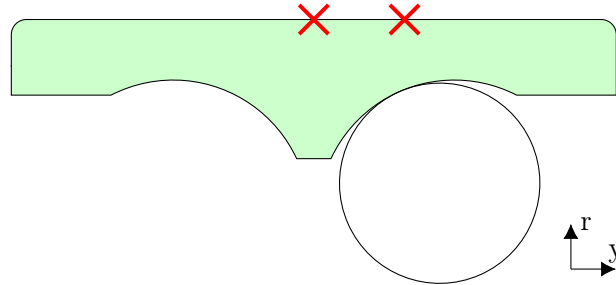

Figure 2.23: Schematic outer ring where only the elements in row 2 are loaded. The red marks indicate the location on which the strain is analyzed. One is between the two rows, while the other is above row 2.

surface between the two rows, and the other is above row 2. The contact angle will be varied, and the first and second harmonics will be extracted from the signal. The
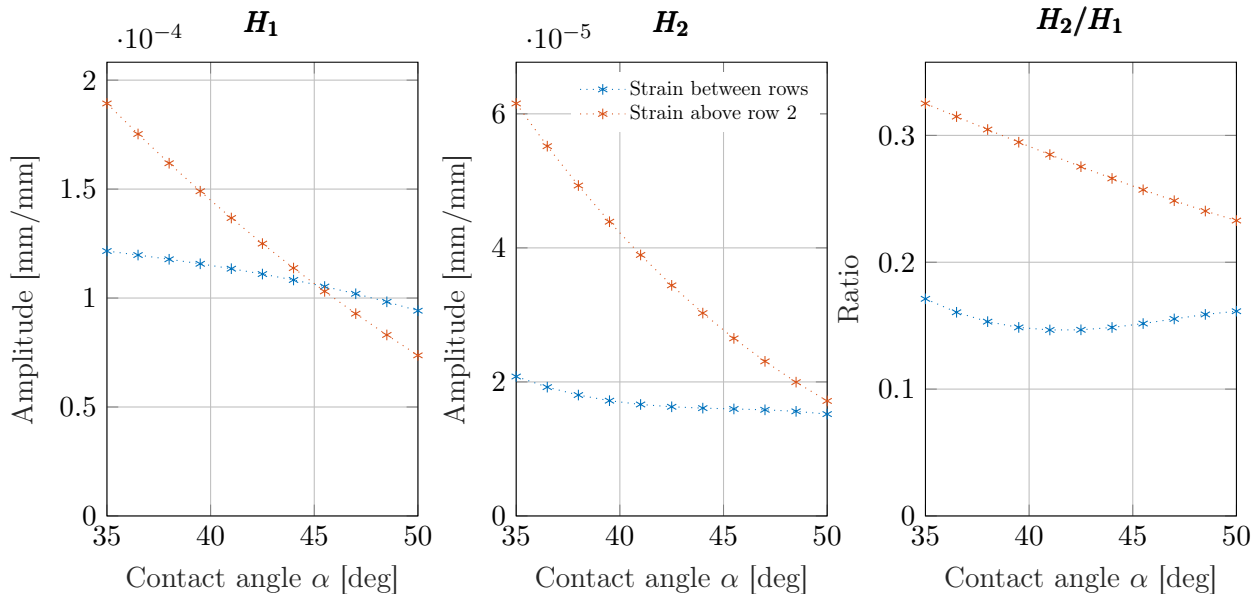
Figure 2.24: The first and second harmonics and their ratios of the strain signals measured for different contact angles and a fixed contact load of 7.5 kN. The strain signal close to the rolling element shows a much higher H_2/H_1. It can also be seen that then the contact angle is around 42°, this ratio is lowest for the strain measured between the rows. At this contact angle the distance between this location and the contact area is also the smallest.

results are shown in figure 2.24. First of all, the harmonics of measured above row 2 are on average higher, which is expected, because this location is much closer to the loaded

contacts. Estimating the load based on the strength of the first or second harmonic alone is not sufficient, because these also vary with the load on the ball. The ratio between the second and first harmonic, however, should remain constant for a varying load because it is assumed that the amplitudes of both harmonics are proportional to the load. This ratio is shown in the right plot and shows that the closer the contact of the rolling element comes to the sensor location, the higher this ratio becomes. The same simulations are done for a fixed contact angle of 41° and varying loads on all the elements to verify that the ratio is not dependent on the element loads. These results
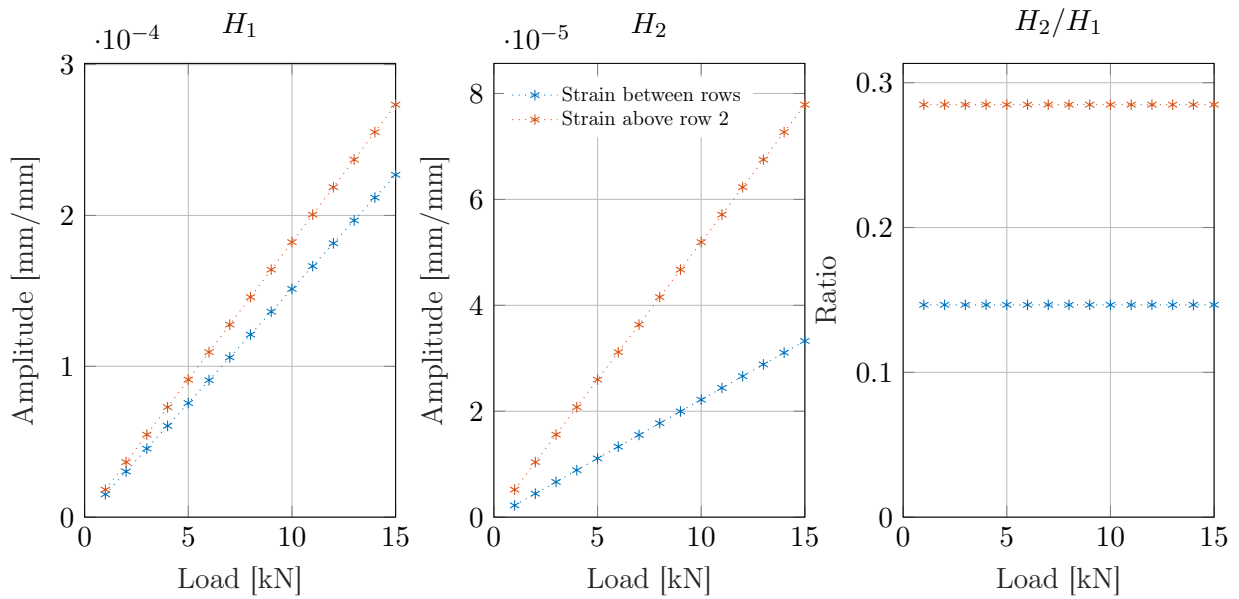

Figure 2.25: The first and second harmonics and their ratios of the strain signals measured for different loads and a fixed contact angle of 41°. The ratio between the second and first harmonics is not related to the load that acts on the rolling elements.

are plotted in 2.25. It shows that the ratios remain constant for varying loads.

2.5. FEA data

The raceway deformation model and the strain model extract the deformation and strain from FEA simulations to construct the models. The FEA data is created by running 1536 simulations, each with a single rolling element on 128 different places along the azimuth and 6 different contact angles, for both rows. The total time to compute these is around 5 days continuously on a laptop. This might seem a long time, but is still significantly shorter than the 30 days it takes SKF to simulate the FEA of only 20 load cases of a complete bearing on a computing cluster. Once these 5 days of computing are over, any load case can be simulated with the proposed model. This section will discuss the setup of the FEA data used to construct this model.

2.5.1. The FEA setup

The proposed model will be verified on the BEaring Test SYstem (BETSY) rig where a modified BAR0282 bearing will be mounted onto a thick steel plate. The FEA model will be made in such a way that it best represents the validation setup. The modified outer ring of a BAR0282 HBU3 bearing is modeled in COMSOL Multiphysics together with the plate. Figure 2.26a shows an image of the model in COMSOL.

(a) Front view of the outer ring and plate with fixed constraints applied to the blue surface. The bolts are shown in red.

(b) Rear view of the outer ring in COMSOL. The green parts are the shims that are placed between the outer ring and plate.
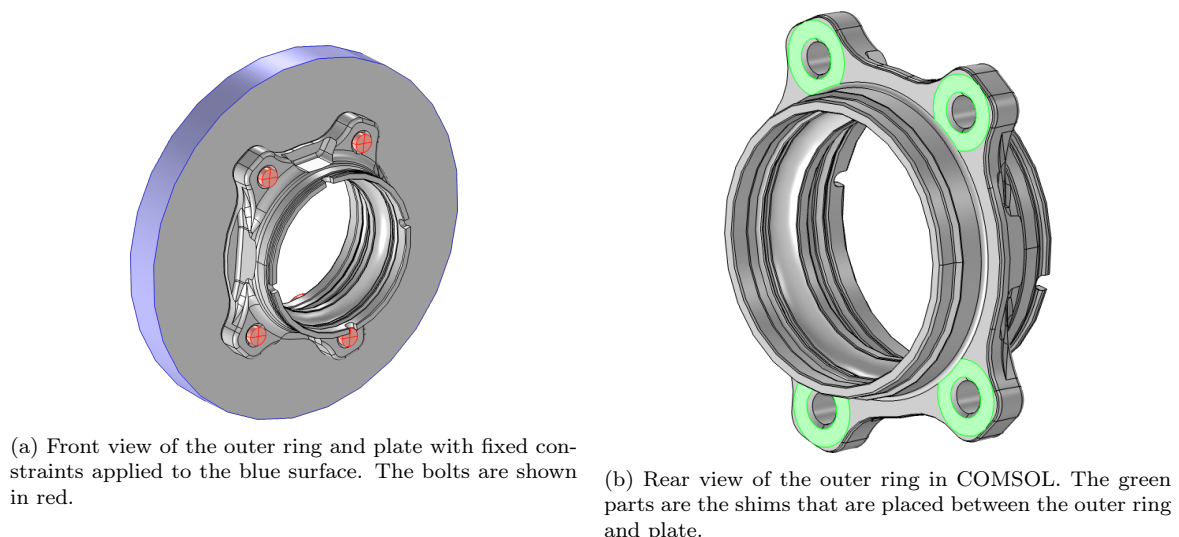
Figure 2.26: Front and rear view of the COMSOL model of the modified outer ring.

The plate is constrained on its outer surface and is shown in the figure by the color blue. Many simulations will be done, so a fast FEA model is a must. Ideally, the FEA is linear since this keeps the solving fast and stable. In reality, this is not the case because there are a few highly nonlinear contact constraints, namely between the rolling elements and the outer ring, and between the outer ring and the plate. Solving such problems in FEA can take a long time and is not robust [21, 22]. As shown in subsection 2.2.5, the Hertzian contact model is an accurate alternative for a rolling

element with a contact constraint and is thus used in the FEA model. The contact ellipse from the Hertzian model can be observed in figure 2.27, where it is highlighted in blue. A distributed load is applied on this surface in accordance with equation 2.24. Simulations show that the contact between the plate and the outer ring is in full
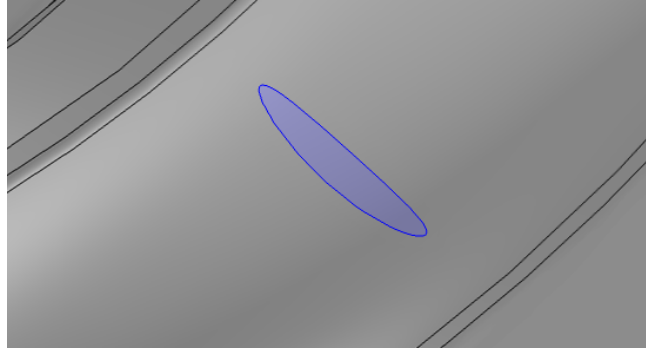

Figure 2.27: Close-up of COMSOL model of the outer ring with the Hertzian contact ellipse highlighted in blue. A distributed load is applied to this area to simulate a rolling element in contact.

contact during some load cases, while it comes loose during other load cases. In order to get rid of this nonlinear behavior, the outer ring will be mounted on the plate in the validation setup on shims around the bolt holes and can be seen in green in figure 2.26b. This ensures that it is always in full contact with the shims during any load case which means that a fixed constraint can be used in the FEA model, thus making the FEA linear and fast in solving.

2.5.2. MESH REFINEMENT
An FEA always calculates the displacement field of a finite amount of elements due to the loads acting on them. These elements can vary in size and are determined by the mesh. A general rule of thumb is that smaller, and thus more, elements give more accurate results but also take more time to compute. An optimum needs to be found in order to generate the FEA data which is both fast and accurate. To find this optimum, a series of simulations are done with different mesh sizes. A rolling element is placed on an azimuth of 270° and the strains are extracted on the outer surface closest to the rolling element. This location is marked by a red cross in figure 2.28. These locations are chosen because here the material is the thinnest and hence the least stiff. It is therefore expected that the inaccuracy due to a too large mesh is highest on this location. Assumed is that the error in the strain converges to zero when the number of degrees of freedom (DOF) is increased (i.e., the mesh size is decreased). Figure 2.29 shows the results of this mesh refinement. All the simulations are performed on a laptop with an Intel Core i7-8550U CPU and 32GB memory. An iterative solver is used as opposed to a direct solver because they are faster and require less memory [23]. The computation times of simulations with more than 1.5×10^7 DOF are not
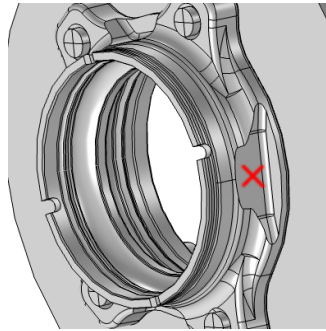
Figure 2.28: Location to sample the strain marked by the red cross. On the raceway just underneath this location, a rolling element is placed. This is the thinnest piece of the outer ring, so it is expected that the largest discretization inaccuracies are located here.
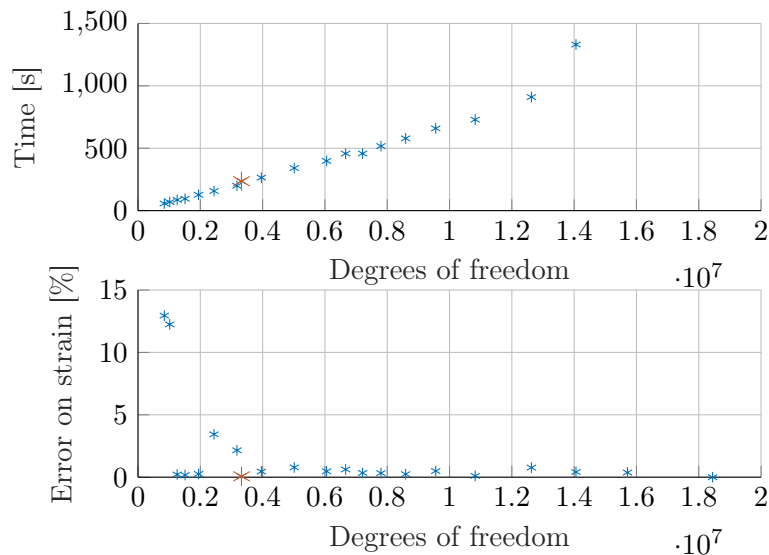

Figure 2.29: The computing time and the calculated strain for different amounts of degrees of freedom of the FEA system. At around 1.4×10^7 the simulations need more than the available 32GB of memory and become significantly slower. The simulation times of the last two simulations are clipped off and are 2917 s and 35 148 s, respectively. A mesh size of 0.75 mm, which corresponds with 0.35×10^7 DOF, is chosen since all the simulations with smaller mesh sizes show an error of smaller than 1 % with respect to the finest mesh simulated.

shown, because for simulations with more than 1.3×10^7 DOF the computer runs out of memory and the hard disc drive was used as temporary storage making the simulation times increase rapidly. The second to last and last simulation took 2917 s and 35 148 s, respectively. Since it is assumed that the simulation with the finest mesh gives the most accurate result, this is taken as the reference strain when calculating the error. The error seems to be converged at around 0.35×10^7 DOF with an error of

less than 1 %. This corresponds to a mesh size of around 0.75 mm for the whole outer ring, and this simulation is marked in the figure with a red asterisk. The time of each simulation takes around 5 minutes, which is acceptable, so all the simulations will be done with this setting.

2.5.3. Verification of linearity
One assumption that is made in the model is that the outer ring behaves linear and thus that via superposition it is possible to combine the strains and deformations due to each individual rolling element in order to get the total strain and deformation of the outer ring. To test the validity of this assumption, a load case is chosen such that a large amount of the rolling elements are loaded. For each rolling element, a simulation is done, and all the resulting deformations are superimposed such that the total deformation is calculated. This is then compared in figure 2.30 to the deformations in an FEA simulation which comprises all the rolling elements. Appendix E shows
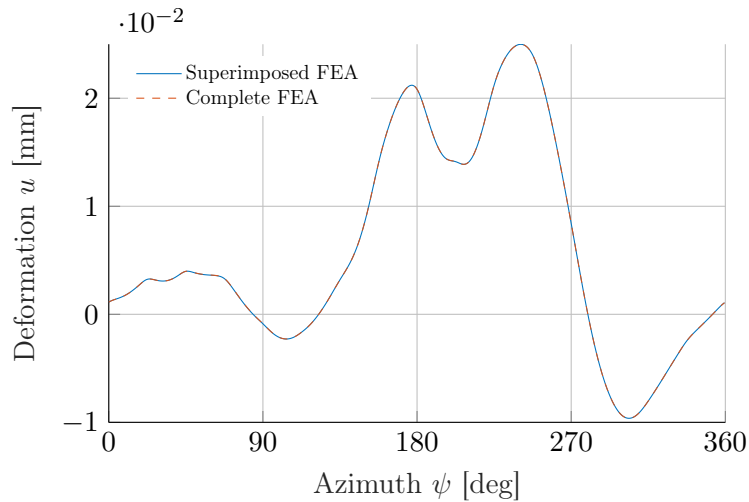

Figure 2.30: Comparison between the superimposed FEA simulations of each element and the FEA simulation of all the elements together. The largest error is 0.019%. This shows that the superposition principle is valid for the FEA simulations.

the contribution of all the elements on both rows to the radial deformation of row 1. Also, the loads and contact angles on each rolling element can be found here in table E.1. The difference between the superimposed FEA and the complete FEA can hardly be observed as both graphs lie over each other. The maximum error between the two is 0.019 %, which is zero to none. This shows that for this linear outer ring, the superposition can be used in order to calculate the total deformation and strain. If the superposition principle holds then also the compliance of the raceway and the strain per load on the outer surface should be independent of the load. To test this, a few simulations are performed where the load on a single element is varied, and the

strain per load is calculated. The results are plotted in figure 2.31. The strain per
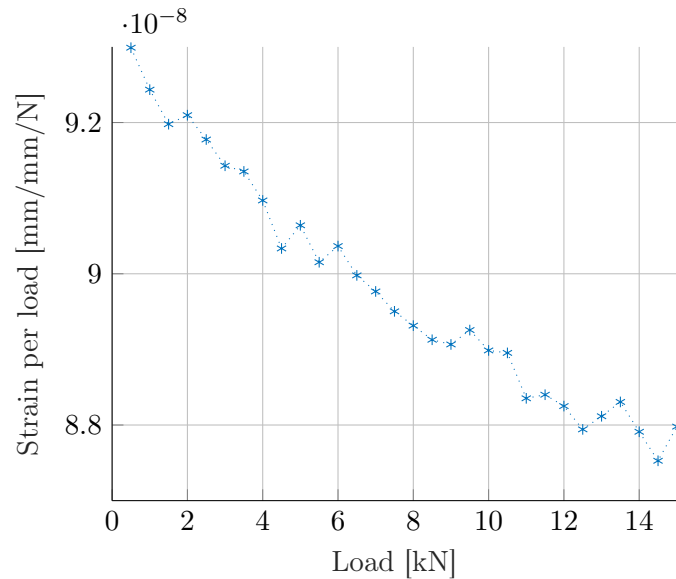

Figure 2.31: The strain per load as a function of the load. A minimal effect due to a change in load is observed in the strain per load caused by varying contact ellipse sizes. It was assumed previously that the strain is proportional to the load. This strain is sampled at a distance of 7.6 mm from the contact area, which is very nearby. Other sensor locations are located further away from the contact area, thus this effect is less. A jitter can be observed in the results. This is caused by the discretization of the mesh.

load is not exactly equal for each load. This is caused by the fact that an increase in load is not only an increase in the stress that is applied to the contact area, but also an increase in the Hertzian contact area. This small variation is enough to change the strain per load slightly. It is expected that the maximum load that will occur on a rolling element is around 15 kN. All the FEA data will be generated with a load of 7.5 kN since this is half of the expected maximum load. For this value, the maximum error on the strain per load will be 2.2 %. Keep in mind that in this example, the strain is measured 7.6 mm away from the applied load, which is a very short distance. According to the principle of Saint-Venant, which is stated in subsection 2.2.6, the effect of the size of the contact area will vanish when the distance between the applied load and the location on which the strain is measured is increased.

2.6. Summary

In this chapter, a methodology is proposed that uses FEA to construct a model that calculates the strain on the outer ring of a wheel bearing. The FEA consist of a series of simulations of a linear elastic outer ring with a single rolling element, modeled with the Hertzian contact theory, on different positions. The so-called rigid bearing model and raceway deformation model (RDM) together find the load and contact angle on each rolling element. The rigid bearing model assumes a rigid inner and outer ring, and calculates the contact angles and loads for a given force on the bearing and deformation of the raceway with trigonometry and the Hertzian contact theory. The RDM calculates the deformation of the raceway as a function of the contact angle, load, and position of all the rolling elements. This model is constructed from the FEA by interpolating these with Fourier and Chebyshev polynomials. The strain model is similar to the RDM and is also constructed from the FEA. The difference is that the strain model only estimates the strain for a predefined set of locations, while the RDM calculates the deformation for a continuous raceway. The whole model can simulate a strain signal in the time domain changing load case and updating the positions of the rolling elements.

The rigid bearing model is verified with a simulation done in SimPro, which shows an error smaller than 1.9%. The Hertzian contact model is validated for use in FEA. With errors smaller than 1.5% on the outer surface of the outer ring, the Hertzian contact model is useful in the FEA as a fast alternative to a rolling element with a contact constraint. The RDM and strain model are compared to FEA, and both show very small differences.

The strain signal simulated with the model is analyzed by looking at the harmonics. This shows that the ratio between the second and first is a function of the contact angle but does not change for different loads. This indicates that the contact angle can be estimated from the measured strain signals by analyzing this ratio.

3

VALIDATION WITH EXPERIMENT

A model is built in the previous chapter of an outer bearing ring that is able to determine the strain by using a semi-analytical approach, which is faster than conventional approaches like FEA or experiments. In order to determine if the model is accurate, an experiment is conducted so that the model can be validated. This is done by instrumenting a bearing with strain gauges and placing it into the BEaring Test SYstem (BETSY) from SKF. This system is able to apply loads to this bearing while it is rotating. This chapter will elaborate on how this experiment is executed and will discuss the results when compared to the model.

3.1. THE EXPERIMENT SETUP

For the experiment, a BAR0282 bearing was modified such that strain gauges can be glued onto the surface of the outer ring of this bearing. Figure 3.1 shows a picture of this bearing and the corresponding COMSOL model. It can be seen that pockets

(a) Photo of the modified BAR0282 bearing. Pockets are milled out of the outer ring to create a good surface for the strain gauges to adhere to. There are a total of four of these pockets.
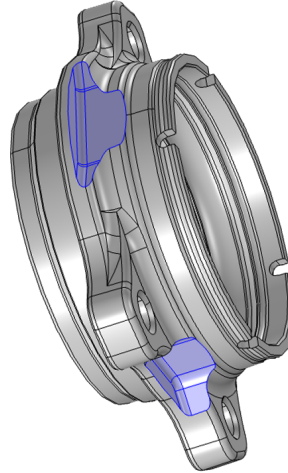
(b) Outer ring model in COMSOL of the same modified bearing. Blue indicates the pockets that are milled out.

Figure 3.1: Side by side photo and COMSOL model of the modified BAR0282 bearing.

are milled out of the surface of the outer ring such that a flat and smooth surface is produced which are ideal for applying the strain gauges. On these surfaces, a total of 18 strain gauges are placed.

Strain gauges are tiny sensors that are able to measure the strain on the surface that they glued to. They consist of a thin foil on which a conductive material is placed in a zig-zag pattern. When the bearing under the strain gauges deforms, the strain gauge is extended or contracted, thus changing its resistance. This change in resistance can be measured and converted into the strain underneath the sensor.

The locations of the 18 strain gauges that are placed on the bearing are shown in figure 3.2a. A photo of strain gauges 13 to 18 is shown in figure 3.2b. In this picture, they are glued but not yet connected with cables.

The strain gauges are placed in a Wheatstone bridge as schematically shown in figure 3.4. The strain on the strain gauge can be calculated with

$$\varepsilon = \frac{R_{sg} - R_{sg0}}{R_{sg0}\mathrm{GF}} \tag{3.1}$$

Here ε is the strain that acts on the strain gauge. The measured resistance of the strain gauge is R_{sg}, and the resistance on the gauge when there is no strain is R_{sg}.

(a) The locations of strain gauge 1 to 18 on the outer ring.

(b) Strain gauges 13 to 18 glued on the surface of the outer ring. In this picture, they are not yet connected with cables.
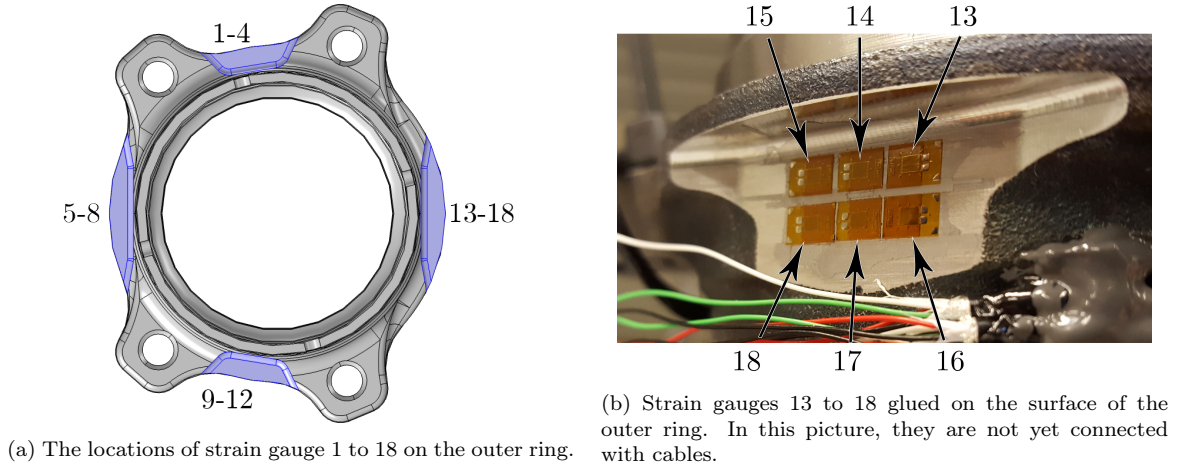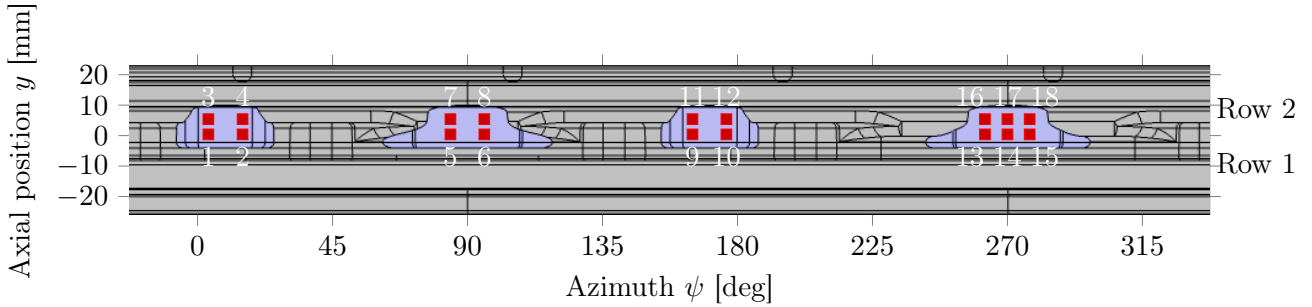
Figure 3.2: The strain gauge locations.

Figure 3.3: All the locations of the 18 strain gauges on the outer surface of the bearing, indicated by the red squares. The image shows a projection of the outer surface onto a 2D plot. The azimuth position ψ is shown in the horizontal direction. The top of the image is the front side of the bearing, while the bottom is side is attached to the plate on BETSY.

The gauge factor, GF, is a property of the strain gauge. The resistance of the strain gauge can be determined with

$$R_{sg} = \frac{RV_s - 2RV_c}{RV_s + 2RV_c}R \tag{3.2}$$

Here R_{sg} is the measured strain gauge resistance, and R are the other $350\,\Omega$ resistors. A supply voltage V_s of $10\,\text{V}$ is applied to the bridge, and the remaining terminals are connected to a conditioner which amplifies the signal V_c by a factor of 1000. The conditioners are *Burster 9236* amplifiers, which are specifically designed for strain gauge signal amplification. This is finally connected to a *Müller PAK MKII G2* controller which captures the signals with a sampling rate of $12.8\,\text{kHz}$ and a resolution of 24 bit on a $20\,\text{V}$ scale.

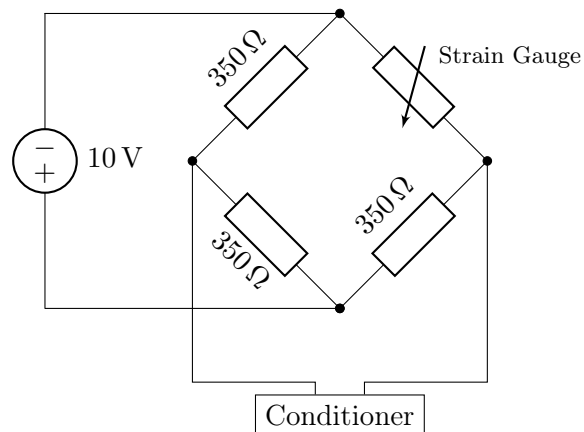With the instrumentation in place, the bearing is installed on a plate that is mounted

Figure 3.4: The circuit diagram of the strain gauge placed in the Wheatstone bridge. A supply voltage of 10 V is used, and the output of the bridge is connected to the conditioner.

on the BETSY rig in the orientation of a left front wheel in a car. This means that the bearing is rotated 165°. Figure 3.5 shows photos of this setup.
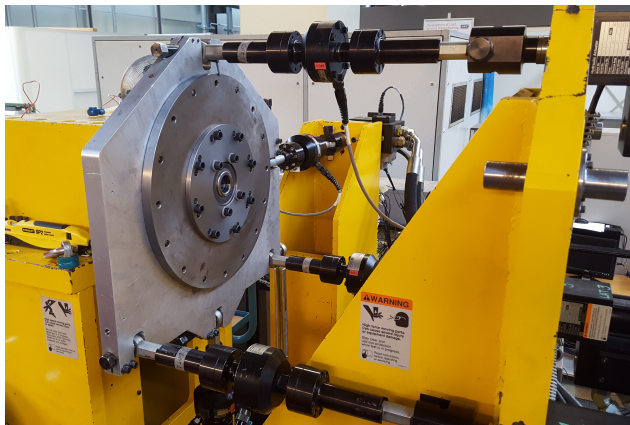
(a) The BETSY rig with the bearing installed on the plate. There is an actuator (the large black rods) in the x-axis and z-axis. Three actuators along the y-axis are used to create F_y, M_x, and M_z. Each actuator has a load cell that measures its load.

(b) The instrumented bearing installed on BETSY with shims between the outer ring and the plate.

Figure 3.5: Photos of the experiment setup in BETSY.

BETSY has five actuators that can apply loads to the plate. The unique property of a bearing is that it can not counter a moment around the axial axis, when zero friction is assumed. This means that five actuators are enough to apply any desired load case on the remaining degrees of freedom of the bearing. There are two actuators that both apply a radial force, in x- and z-direction, while the remaining three actuators are all placed in the axial y-direction. These are able to apply an axial load and a moment around the x- and z-axes.

As mentioned in section 2.5, the bearing is mounted on shims to ensure that it stays in full contact during any load case, thus making the deformation of the outer ring linear. A total of four bolts are tightened by hand with an ordinary wrench.

During all experiments shown in this thesis the inner ring of the bearing rotates at a speed of 600 rpm. The speed of the cages, that keep the rolling elements in place, is different.Its speed can be estimated with the formulas to calculate the gear ratios of planetary gears. In this case, the cages act like planet carriers while the outer ring is stationary. The speed of the cages become

$$\frac{\omega_c}{\omega_i} = \frac{R_{i,0} - r_i \cos(\alpha)}{R_{i,0} + R_{o,0} + (r_o - r_i) \cos(\alpha)} \tag{3.3}$$

Here $\dfrac{\omega_c}{\omega_i}$ is the ratio between the rotation speed of the cages and the inner ring. All the other parameters can be found back in figure 2.4. Effectively this equation calculates the ratio between the mean inner raceway contact diameter and the pitch diameter, which is defined in equation 2.2. For the BAR0282 bearing, this ratio equals approximately 0.43. With an inner ring speed of 600 rpm, which equals to 10 Hz, and 16 rolling elements per row this corresponds to a ball pass frequency of 68.4 Hz.

Keep in mind that this function is dependent on the contact angles of the rolling elements which are different for each row and change slightly for each different load case. This also means that the speed of the inboard and the outboard cages vary from each other. The frequency of each row will be determined from the signals of each load case and will be used as input to the model to determine the location of all the rolling elements. Each actuator of BETSY has a load sensor that is recorded in sync with the strain gauge signals. These measured loads will also be the input for the model.

3.2. Comparison with Axial loads

For the first comparison, we will first look at a varying axial load from $10\,\text{kN}$ to $-10\,\text{kN}$ that is applied in different steps to the bearing on BETSY. Table 3.1 shows the axial

Load case	F_x [kN]	F_y [kN]	F_z [kN]	M_x [kNm]	M_z [kNm]
1	0.00	10.00	0.00	0.00	0.00
2	0.00	6.67	0.00	0.00	0.00
3	0.00	3.33	0.00	0.00	0.00
4	0.00	0.00	0.00	0.00	0.00
5	0.00	-3.33	0.00	0.00	0.00
6	0.00	-6.67	0.00	0.00	0.00
7	0.00	-10.00	0.00	0.00	0.00

Table 3.1: The load cases used to validate the model. The loads shown in this table are rotated to the reference frame of the bearing used in this report.

load cases used. In order to be able to compare the strain signals with each other, the signals will be converted to the frequency domain via the fast Fourier transform (FFT). Figure 3.6 gives an example of what the signal looks like for load case 4 of table 3.1, and figure 3.7 shows the same signal in the frequency domain.   The left plot
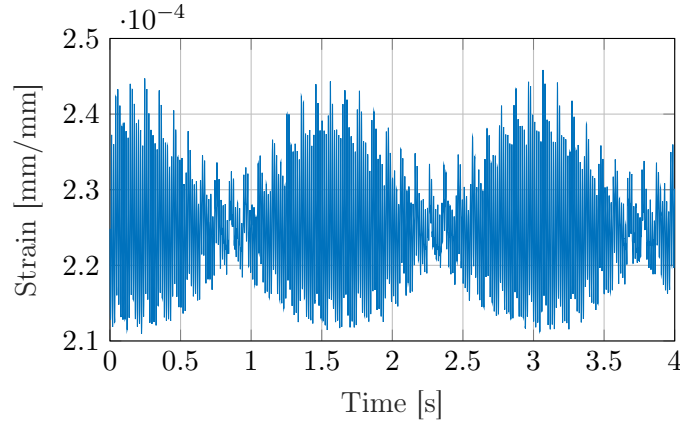

Figure 3.6: The measured strain of strain gauge 1 when no load is applied, and the bearing rotates at 600rpm. A clear amplitude modulation can be observed in the signal.

shows the signal for the first $150\,\text{Hz}$. At $10\,\text{Hz}$ a peak can be seen that corresponds to the rotation frequency of the bearing of 600rpm. Its higher harmonics can be observed at $20\,\text{Hz}$ and even $30\,\text{Hz}$. The peaks around the ball pass frequency of $68.4\,\text{Hz}$ are the largest peaks in the plot, and the middle plot is focused upon these. The second harmonic of the ball pass frequency is shown in the right plot. The frequency and amplitude of these peaks are useful information that needs to be extracted from this FFT. Since the signal is discrete, these values can not be found directly in the FFT,
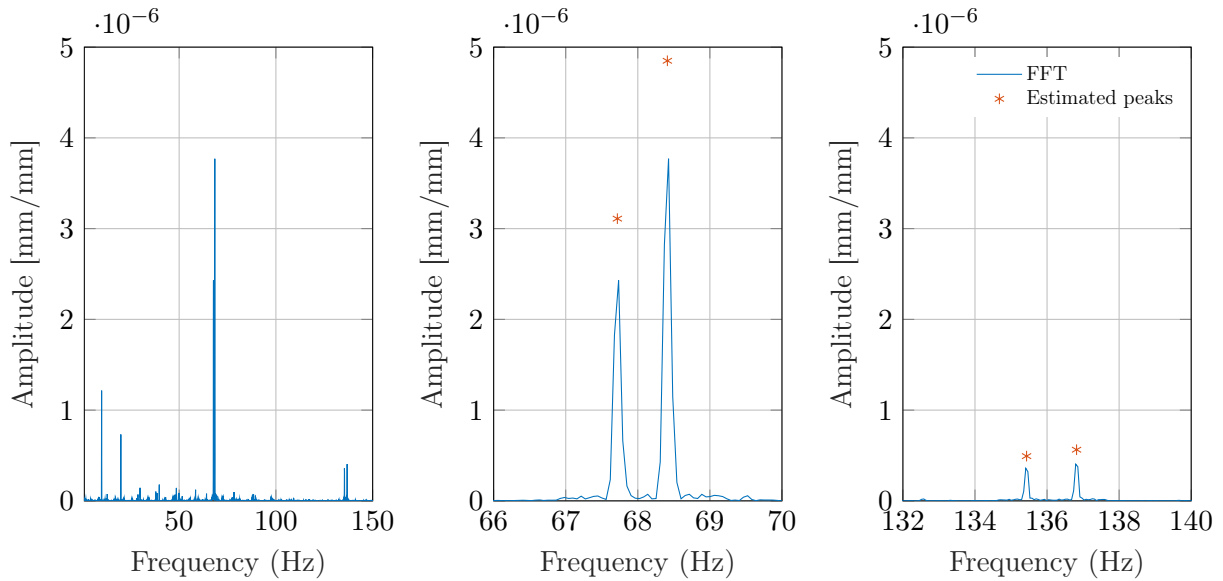
Figure 3.7: The FFT of the strains measured by strain gauge 1 during no load on the bearing and a rotating speed of 600 rpm. The left plot shows the complete FFT from 1 Hz to 150 Hz. The rotation frequency (10 Hz) can be observed and its higher harmonics. The middle plot is focused on the two large peaks around 68.4 Hz, which are the ball pass frequencies of the two rows. A clear difference in speed can be observed between the speeds for this load case. The red marks indicate the estimated amplitude and frequency of the peaks. The right plot shows the second harmonic of this ball pass frequency.

but need to be calculated. The frequency is estimated using barycentric fitting around each peak, while the amplitude is calculated by taking the root sum of squares of the samples around the peaks. The resulting frequencies and amplitudes are also shown in the plots by a red mark.

The fact that there is a speed difference between the two rows while there is no load acting on the bearing may appear strange. There are, however, differences in stiffness of both rows. Combining this with the bearing preload that is maintaining a load on the rolling elements creates different contact angles in each row. Also, the diameters of the inner rings might vary due to the way they are produced. Ideally, each sensor gives clear distinguishable peaks for each row, but unfortunately, this is not always the case. When, for instance, the speed difference between the rows is minimal, these peaks will merge together. Also when the load under the strain gauge is low, the peak diminishes to zero and is thus undetectable in the noise.

The bearing is symmetric around the horizontal plane, and since the applied axial load is also symmetric over this plane, we expect the distribution of the loads along all the rolling elements to be symmetric around the same plane. Using the model, the distribution of the loads on all the rolling elements can be calculated for these
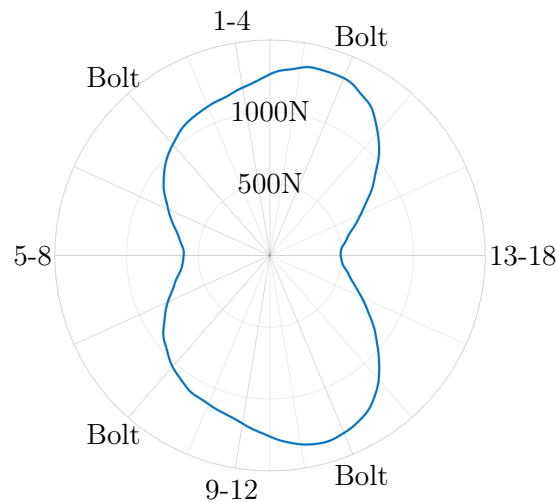
Figure 3.8: The loaded zone of all the rolling elements in the outboard row during an axial load of $-10\,\mathrm{kN}$. The loads on the other row are almost zero. The locations of the strain gauges and bolts are shown around the plot. Since the bearing is symmetric along its horizontal plane and the load is axisymmetric, the loaded zone is also symmetric. The stiff parts of the bearing increase the loads on the rolling elements.

load cases while the bearing is rotating. Averaging these rolling element loads for each azimuth with an axial load of $-10\,\mathrm{kN}$ gives a smooth line of the load distribution, which can be viewed in figure 3.8. For clarity, the axis around the plot does not show the azimuth, but the locations of the bolts and the strain gauges, as can also be seen in figure 3.2a.

The outer ring of the bearing is thick around the bolts, while it is thin on the locations of the strain gauges, especially around strain gauges 13-18. This can be seen in the load distribution where the loads are higher at the top and bottom of the bearing where the bolts are. It is expected that this behavior will give the same signals on the top and bottom of the bearing.

When looking at figure 3.3, it can be observed that the following pairs of strain gauges are in symmetric positions and should give identical signals: 1&10, 2&9, 3&12, and 4&11. The mean value of the signal (H_0), the amplitudes of the first harmonic (H_1), and the amplitudes of the second harmonic (H_2) are plotted in figure 3.9. In summary, the figure shows three columns containing:

Column 1: H_0 This zeroth harmonic is the mean value of the strain signal.

Column 2: H_1 The first harmonic is the amplitude of the ball pass frequency. Since there are two rows, each row has its own H_1.

Column 3: H_2 H_2 is the same as H_1, but at twice the frequency.

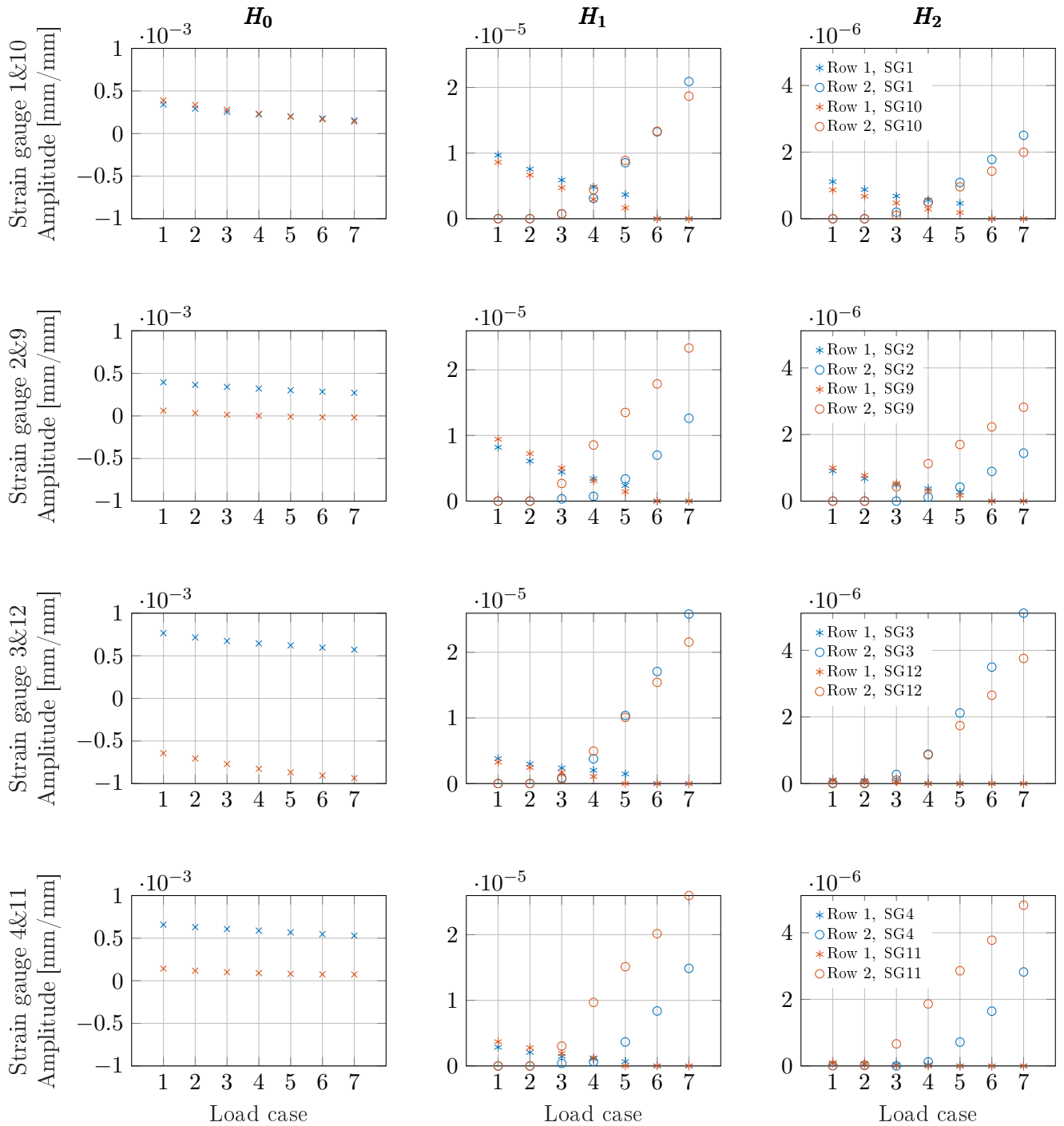Each row contains all the harmonic for the same strain signal(s).

Figure 3.9: The amplitudes of zeroth, first and second harmonics of the symmetric sensor pairs for each row when only axial loads are applied to the bearing. Each load case can be seen in table 3.1. It is expected that each sensor pair generates identical strains, which can be seen is not the case. The abbreviation SG in each legend stands for strain gauge.

Looking at these plots, it can be clearly seen that each pair of sensors does not give the same signal. The same behavior is seen within each pair, but with different offsets and different slopes. For instance, all the sensors show a decline in H_0, but all with different offsets. Not only is there an offset in H_0 between the sensors, but the slope of the decrease changes within each pair. This is especially clear in the plot for strain gauge 1 and 10 where the decline in H_0 is larger for strain gauge 10.

In the frequency domain of each signal for these load cases, a distinction could be made between the amplitudes of the harmonics for each separate row. This is only possible because a constant load and constant rotation speed are used for an extended period of time. Due to this, the contribution of each row to the signal can be determined. These separate row 1 and row 2 signal amplitudes on each sensor pair are plotted in the middle column (H_1) and right column (H_2).

Strain gauges 1, 2, 9, and 10 are all located above the center of both rows. Despite this, the signal strength due to row 1 during a large axial load (e.g., load case 1) is less than the signal strength due to row 2 during the same axial load in reverse direction (e.g., load case 7). This can be explained by the fact that the outer ring is stiffer around row 1 due to a flange being present above this row, as can be seen in figures 3.1 and 3.2. This prevents the outer ring to deform as much as it would do due to loads on rolling elements in row 2. When a high positive or negative axial load is applied to the bearing the loads on the unloaded row become very small. Otherwise, during load cases 3 to 5, the preload on the bearing will ensure that both rows stay in contact. This can be seen in the plots where the signal is produced by both rows.

When comparing H_1 and H_2 of each symmetric sensor pair with each other, a significant difference can be seen within each pair. Especially the strain gauge pairs 2&9 and 4&11 show a very large difference. Keep in mind that these sensor pairs are next to each other on the same azimuth. Since the same difference is spotted in both sets of sensors, it is believed that this is not caused by a defect strain gauge, but by differences in the load of the rolling elements close to these sensors.

During load case 3 and 4, the first and second harmonics due to a load on row 2 can be identified for strain gauge 9 and 11, while these are near zero for strain gauge 2 and 4. This indicates that the rolling element is loaded under strain gauge 9 and 11, but not under strain gauge 2 and 4. Although not shown in these plots, substantial differences are also present in the symmetric strain gauge pairs 5&6, 7&8, 13&15, and 16&18. A few possible sources for these differences could be:

Strain gauge location The strain gauge is glued on the outer surface of the outer ring by hand. The position along the azimuth can be verified by looking at the phase of each signal. This shows that for this bearing, the strain gauges are placed quite accurately along the azimuth. The axial placement of each sensor can not easily be determined by analyzing the signal, but may influence it.

Strain gauge installation During the gluing process, the strain gauges are pressed against the outer ring. This may cause a permanent deformation, and thus offset,

in the strain gauge signal. This can explain the large differences in H_0. Since the strain gauges are linear, this does not explain the differences in H_1 and H_2. The glue between the outer ring and the strain gauge may also attenuate the strain on the outer surface.

Residual stress The first step in the production of the outer ring is forging it to the approximate shape. After this, only the inside is ground to achieve the correct dimensions and surface roughness for the raceways. In modifying the bearing for the experiment, the strain gauges had to be placed on a flat and smooth surface. To accomplish this, pockets are milled out of the outer ring as can be seen in figure 3.1a. The forging process creates large stresses in the material of the outer ring. If suddenly some pockets are milled out, it is not unthinkable that the residual stresses in the outer ring deform the raceways, thus significantly changing the loaded zone of the rolling elements.

Bolt tightening When the bearing was installed on the rig, it was tightened down on four bolts. This was done with a regular wrench and not with a torque wrench. If this was done unevenly, this can cause small differences in stresses and thus deformations near these bolts. Besides this, the tightening of the bolts is an asymmetric process as all the bolts turn clockwise to fasten. The friction between the bolt and the outer ring might rotate it locally around the bolt and deform the raceways considerably.

Thickness of outer ring The outside of the outer ring is not accurately machined after it was forged. This means that the thickness of the outer ring may vary in each position. The stiffness of the outer ring is a function to the third power of the thickness of the material, so this could be of significant influence.

These possible sources affect the following aspects of the bearing:

- The distribution of the loads over all the rolling elements.

- The individual contact angle of all the rolling elements.

- The transfer of the element loads to surface strains.

- The difference in measured strain by the strain gauges and the true strain.

It is unknown how much each of these possible sources contributes to the differences in the signals, and there may be even other sources. All these effects are not calibrated in the model because it is difficult to quantify them in terms of measures that can be used in the model. Unfortunately, this makes it hard to make a quantifiable comparison between the model and the experiments.

A comparison is made between the measured and simulated strain signals from strain gauges 1, 5, 9, and 13, one from each quadrant of sensors. The zeroth, first, and second

harmonics of these strain signals are plotted in figure 3.10. The harmonics of all the strain gauges can be found in appendix F.

The strain gauges on the top and bottom of the bearing (i.e.,1-4 and 9-12) show higher strain signals (H_1 and H_2) than the other strain gauges in both the model as the experiment. This is expected as the outer ring is stiffer around these strain gauges. As shown in figure 3.8, this causes the loads on the rolling elements near the top and bottom to be higher.

When a small load is applied to the bearing, as is the case in load cases 3-5, a strain signal generated by both rows can be observed. This is expected, as a preload in the bearing ensures that the rolling elements in both rows stay loaded when a small load is applied. Looking at the top and bottom strain gauges again, the rolling elements in one row lose their load, and the signal is only generated by loads in one row.

Due to the different stiffness for each row, the load distribution of row 1 during the first load cases will not be the same as the load distribution in row 2 during the latter load cases. However, if the outer ring would be rigid, they would be the same. Strain gauge 5 and 13 show this for both the experiments as the model where row 2 continues to be loaded during load cases 1 and 2, while the elements in row 1 are unloaded during load cases 6 and 7.

The model shows the same behavior as the measured signals, but with a significant difference. These differences are in the same order of magnitude as the difference between the symmetric sensor pairs analyzed before. It is therefore not possible to make any quantifiable conclusions regarding the accuracy of the model. It is clear that further research is necessary in order to determine how much the outer ring is statically deformed while it is clamped on the plate in BETSY. The simulated signals do show the effect of the preload in the same way. The simulated signals show the same differences in signal strength due to each individual row as the measured signals do. This shows that the model is very good in predicting behavior similar to the measured signals. It is believed that the model can become more accurate, if further research is done on calibrating the model to a specific bearing.
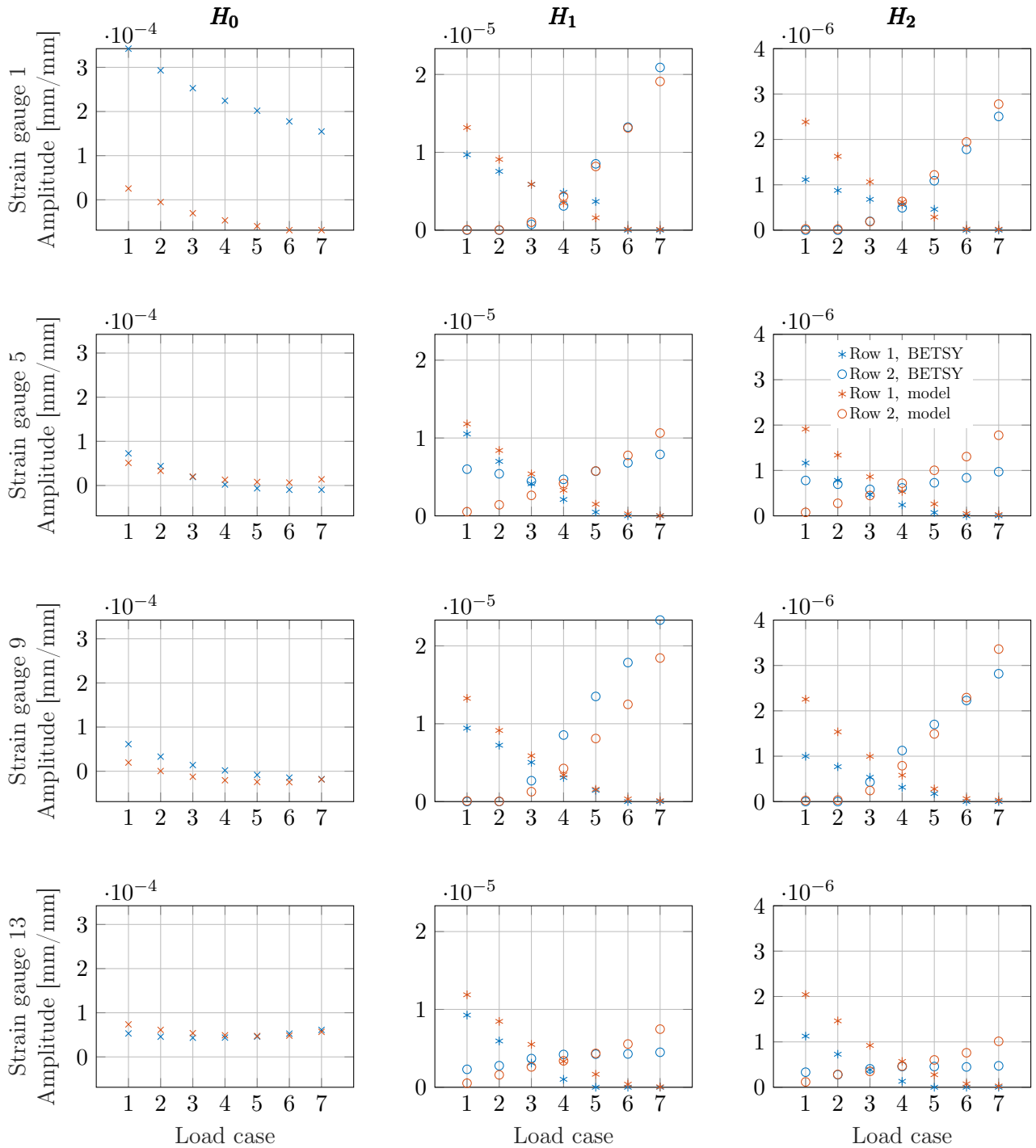
Figure 3.10: The harmonics of the strain signals measured and simulated on strain gauges 1, 5, 9, and 13. The left, middle, and right columns show the zeroth, first, and second harmonics, respectively.

3.3. COMPARISON WITH RADIAL LOADS

Further comparisons are made for a radial load that is applied to the bearing. The load will range up to 8 kN, which is a realistic load for a car wheel. The load is applied to an azimuth of $-75°$ from the top, and all the load cases are shown in table 3.2. During

Load case	F_x [kN]	F_y [kN]	F_z [kN]	M_x [kNm]	M_z [kNm]
1	0.00	0.00	0.00	0.00	0.00
2	-1.93	0.00	0.52	0.00	0.00
3	-3.86	0.00	1.04	0.00	0.00
4	-5.80	0.00	1.55	0.00	0.00
5	-7.73	0.00	2.07	0.00	0.00

Table 3.2: The radial load cases used to validate the model. The loads shown in this table are rotated to the reference frame of the bearing.

these loads, both rows will be loaded approximately equally. As could be seen before in the frequency domain of the strain signal of an unloaded bearing, both rows rotate at a different speed. During the radial load cases, this is expected to still be the case, because the outer ring is less stiff around row 2 than it is around row 1. This means
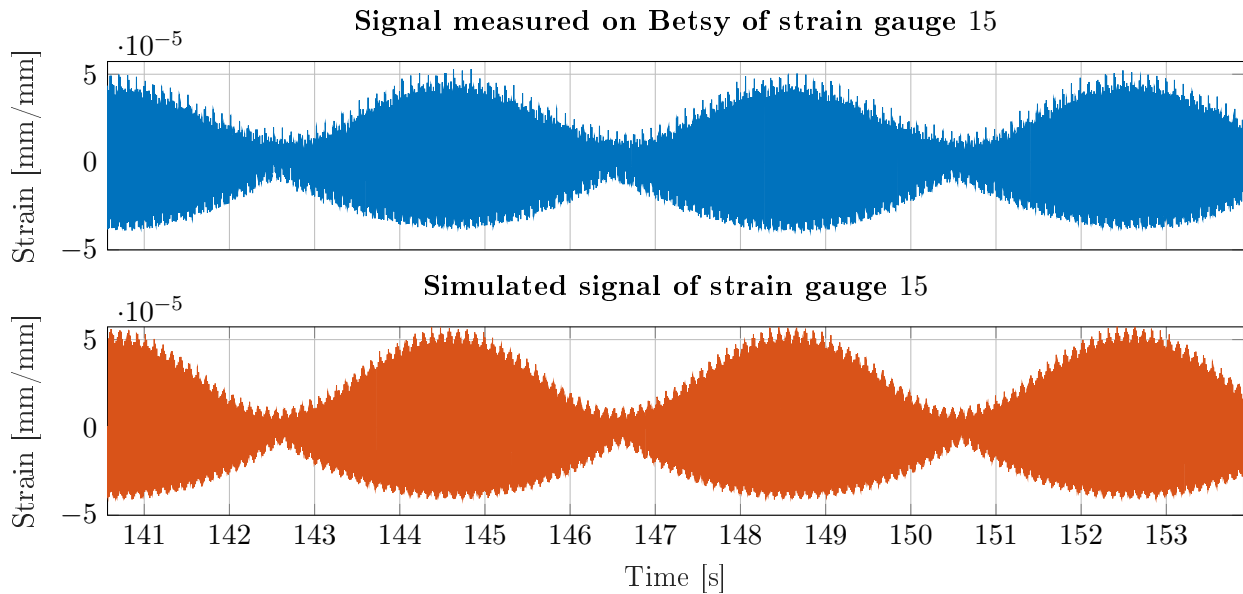

Figure 3.11: The signals measured and simulated on strain gauge 15 for a pure radial load case of $F_x = -7.67$ kN and $F_z = 2.05$ kN. The top graph shows the measured strain signal from the BETSY experiment and the lower graph shows the simulated strain signal. A modulation of the signal is clearly present due to the fact that the speed of the elements in one row is slightly faster than in the other row.

that the outer ring around will deform more around row 2, thus causing the contact

angles in each row to be different. The signal measured on strain gauge 15 during the highest radial load case is simulated, and both signals are shown in figure 3.11. The top plot shows the measured signal, while the bottom plot shows the simulated signal. The mean value of both signals is removed such that the y-axes of both plots are comparable. The rolling elements in row 1 pass by the sensor with a frequency of 67.94 Hz and row 2 with 67.70 Hz. This is a small difference, but any difference will create an amplitude modulation in the signal, as can also be observed in the signal. At the beginning of each plot (t=140.5 s), the rolling elements of both rows are in phase with each other. Since row 1 is slightly faster, it will eventually be exactly out of phase with the second row (t=142.7 s). The frequency of the modulation can be estimated with:

$$f_{\mathrm{mod}} = \left(\frac{f_{r1}}{f_{r2}} - 1 \right) f_{r1} = 0.25 \, \mathrm{Hz} \tag{3.4}$$

Here f_r are the ball pass frequencies of row 1 and 2, and f_{mod} is the frequency of the modulation. The modulation frequency of 0.25 Hz can be seen in the signal, as it repeats itself every 4 s. In this time the rolling elements of row 1 have overtaken one rolling element of row 2.

The simulated and measured signals from strain gauges 1, 6, 15, and 18 will be analyzed. Strain gauge 6 is on the opposite side of the loaded zone, so it is anticipated that it will show no first and second harmonic in the signal during the larger load cases. Strain gauges 15 and 18, on the other hand, are closest to the highest loaded elements. Finally, strain gauge 1 is also close to the average loaded elements. The results of these strain gauges can be found in figure 3.12, while the results of all the sensors can be found in appendix G.

Looking at the first strain gauge, which is located between both rows, the strain signal due to both rows seems to be about equal and slightly increasing for increasing loads. Strain gauge 15, also located between both rows, shows a much larger contribution of row 2, while the model estimates an equal contribution. On strain gauge 18, next to 15, the model and measurements show similar behavior for both rows. It is, of course, expected that when the load is increased, the signals also increase in these locations. Strain gauge 6, however, is on the opposite side, and here a decrease in signal strength can be seen for increasing load cases. This is expected as the loads on the rolling elements reduce. Due to the preload in the bearing, the load on these elements are not zero for the first four load cases.

All signals show a slight exponential increase or decrease (depending on location), which is also predicted in the simulated signals.

Again, as with the axial load cases, there is a significant difference in the signals of the model and the measurements, but the general behavior found in the experiment is also encountered in the model.
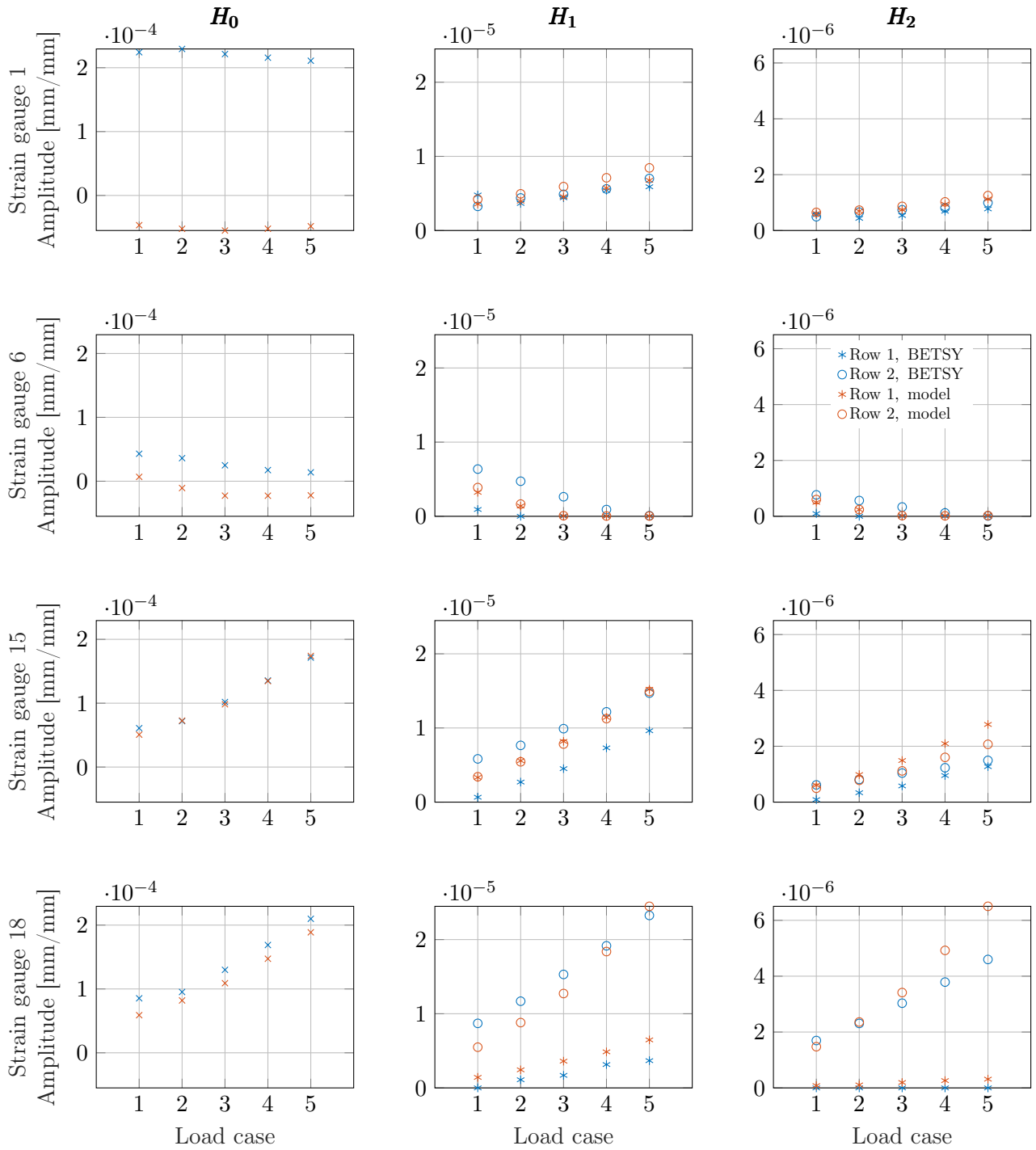
Figure 3.12: The harmonics of the strain signals measured and modeled on strain gauges 1, 6, 15, and 18 while a radial load is applied. The left, middle, and right plots show the zeroth, first, and second harmonics, respectively.

3.4. Comparison with Moment loads

The final comparison will be made for a moment that is applied to the bearing. Ranging up to $2.5\,\mathrm{kN\,m}$ in steps of $500\,\mathrm{N\,m}$, the moment is applied in 6 load cases under an angle of 15° from the top, all shown in table 3.3. These moments occur during

Load case	F_x [kN]	F_y [kN]	F_z [kN]	M_x [kNm]	M_z [kNm]
1	0.00	0.00	0.00	0.00	0.00
2	0.00	0.00	0.00	-0.48	0.13
3	0.00	0.00	0.00	-0.97	0.26
4	0.00	0.00	0.00	-1.45	0.39
5	0.00	0.00	0.00	-1.93	0.52
6	0.00	0.00	0.00	-2.41	0.65

Table 3.3: The moment load cases used to validate the model. The loads shown in this table are rotated to the reference frame of the bearing.

cornering of a car when a lateral force acts on the contact patch of the tire. In the bearing these moments create the highest loads on all the rolling elements, thus these moments are considered the heaviest loads that act on a bearing, with loads on the rolling elements ranging up to $15\,\mathrm{kN}$. It is expected that if there are temperature effects present, they will be most apparent during these load cases.

Figure 3.13 shows what the strain signal measured by strain gauge 2 looks like during load cases 2 to 6. Each load case is applied for $30\,\mathrm{s}$ after which a $10\,\mathrm{s}$ resting period is employed in order to distinguish each separate load case. During this resting period, the bearing continues to rotate at 600 rpm, but no load is applied. Looking at the strain signals during these resting periods, a drift can be observed. This drift can even be seen slightly during the load cases, where a slow decline of mean strain signal over time is present. The right side of the figure shows two plots containing the zeroth and first harmonic of these signals.

The temperature increase in the bearing deforms the outer ring so that the strains change over time. This deformation, in turn, affects the loads on the rolling elements, thus influencing the first harmonic. The temperature affects the first harmonic only slightly, but the exponential trend in the strain signals appears to not yet be at a steady-state value. This indicates that the temperature will probably increase even further if the experiment took longer. Further experiments with high loads for a long time should show how much the temperature affects the first harmonic of the signals. The change in zeroth harmonic, due to the temperature change, is in the same order of magnitude as, for instance, the increase due to increasing load during the axial and radial load cases. This shows that it is very hard to estimate the load on the bearing based on the zeroth harmonic alone.

For the comparison of the signals from these load cases, strain gauges 2, 4, 10, and 12 are used. Figure 3.14 shows the results. All the other signals can be found in appendix H. During these load cases, both rows have a loaded zone in the opposite
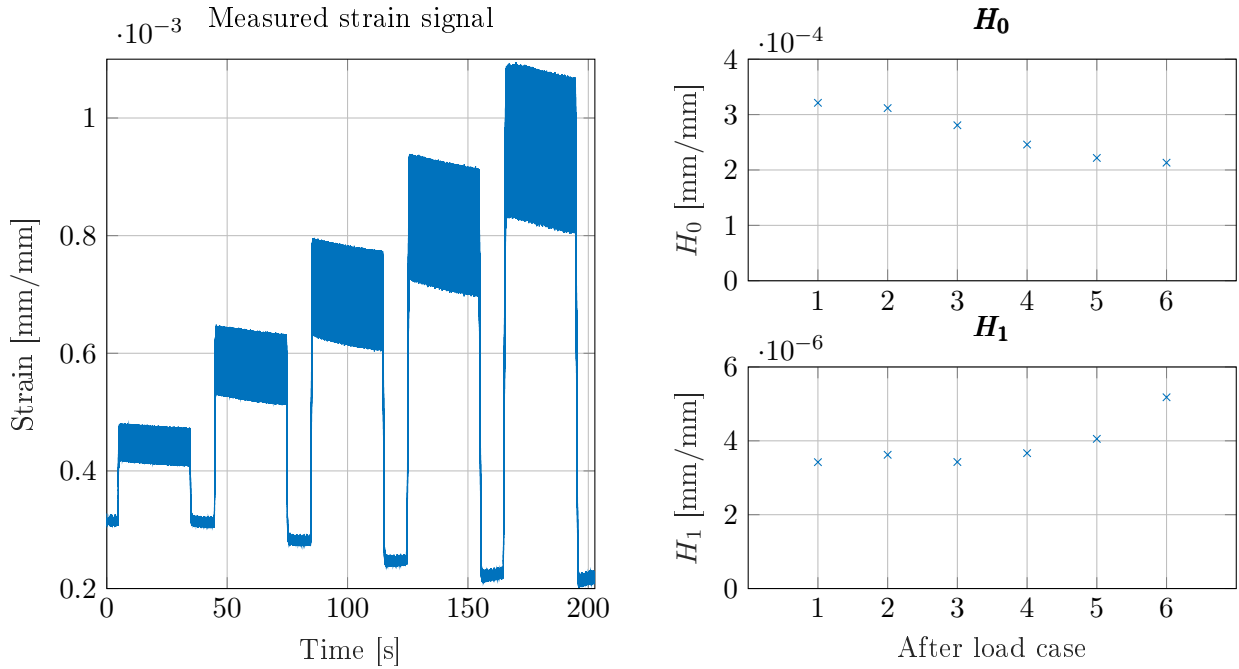
Figure 3.13: The signal measured with strain gauge 2 while different moments are applied to the bearing is shown in the left plot. Between each load case there is a small resting period in which no load is applied for 10 s. It can be seen that the signals increase between each applied load case due to thermal effects. The right two plots show the amplitudes of H_0 and H_1 of the signal during each resting period between the load cases.

direction in order to counteract the moments that act on the bearing. Strain gauges 2 and 4 are closest to the highest loaded elements in row 1, while strain gauges 10 and 12 are closest to the highest loaded elements in row 2. See figure 3.15 for a schematic overview of the locations of the strain gauges and the loaded rows. Both sets of strain gauges are next to each other on the same azimuth. Strain gauge 2 and 10 are between the rows, while the other two are above row 2. The first observation that can be made is that the zeroth harmonic increases for an increasing load at strain gauges 2 and 4, while it remains somewhat constant on the other strain gauges. The model also predicts this behavior, albeit with an offset. The model also follows H_1 quite good, but 50 % higher. Since only row 1 is loaded near strain gauges 2 and 4, a strong H_1 is seen in strain gauge 2, but not in strain gauge 4. Strain gauge 4 is located above row 2, so this behavior is expected. The other two strain gauges both show a strong H_1 due to row 2.
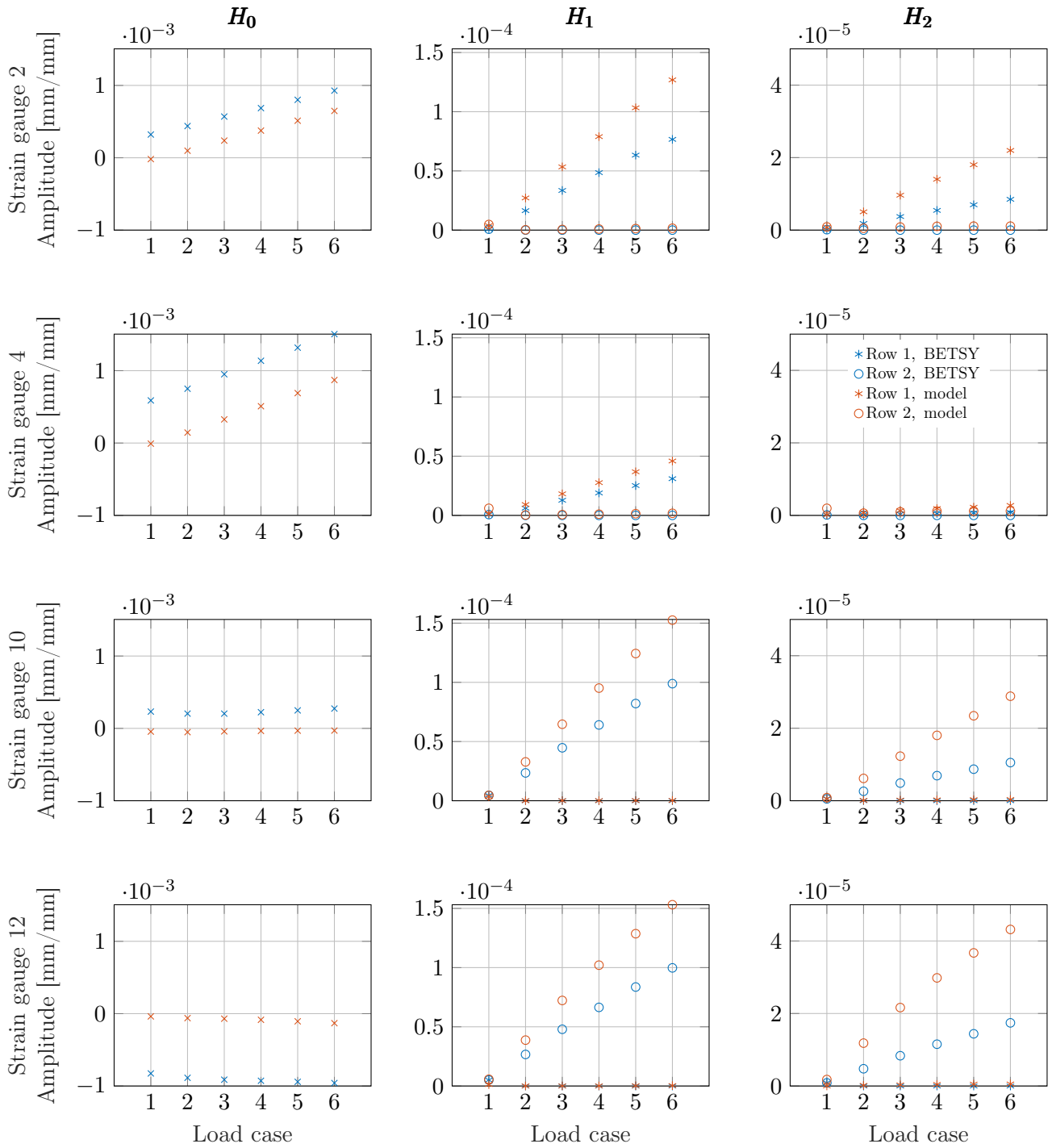
Figure 3.14: The harmonics of the strain signals measured and simulated on strain gauges 2, 4, 10, and 12. The left, middle, and right plots show the zeroth, first, and second harmonics, respectively. The simulated signals show the same behavior as the measured signals, with only an offset and a different factor.
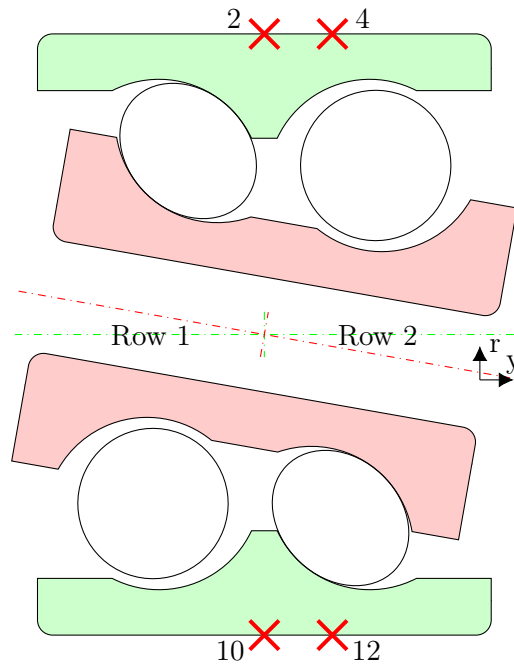
Figure 3.15: A schematic overview of the moment load cases with the locations of strain gauges 2, 4, 10, and 12. Gauge 2 and 10 are between both raceways, and the other two not. Strain gauge 4 is located far away from the loaded elements, while strain gauge 12 is very close.

It is expected that when the distance between the strain gauge and the loaded element is close, the higher harmonics become stronger. In other words, when a strain gauge is right on top of the raceway, it is expected that H_2/H_1 becomes larger than if the strain gauge would be placed further away. This can be seen in the signals. Strain gauge 4 is able to detect a first harmonic strain signal with insignificant higher harmonics. Strain gauge 2 is closer to row 1, and although its H_1 is 3 times higher, the H_2 is around 8 times higher. Strain gauges 10 and 12 show this as well. Both H_1 are about equally high, while the H_2 of strain gauge 12 is more than $50\,\%$ higher in both the measurements and the model.

While the moments are applied, the increase in harmonics is almost linear. This is measured during the experiments but is also simulated with the model. Other than an offset in H_0 and a ratio in H_1 and H_2, the model performs good during these moment load cases. Note that during these extreme moment load cases, with large element loads, the effect of any static raceway deformation diminishes, since these effects are an order of magnitude lower than the strain signals generated by the element loads. This explains why the model shows the exact same behavior as the experiments, disregarding any offset and ratio present in each strain gauge.

3.5. Summary

A methodology for calculating strain signals on the outer ring of a wheel bearing as a function of the load applied to the bearing was presented in chapter 2. In the current chapter, this model was compared to experiments. For these experiments, a bearing was instrumented with strain gauges and placed in a test rig. This rig rotates the bearing and applies load to it while the strain signals are recorded.

An axial load applied to the bearing shows unexpected behavior of the bearing. The strain gauges opposing each other with respect to the symmetry plane show a large difference in signals when compared to each other, while a symmetric load is applied. The observed signals indicate that a large distortion in the shape of the raceways may be present due to manufacturing or installation of the bearing.

When comparing all the measured signals to the simulated signals, the differences are in the same order of magnitude as the differences due to the distortion in the raceway, making it difficult to make a quantifiable comparison. All the signatures in the measured signals are seen in the simulated strains, indicating that the model might work good, but needs to be calibrated. It is believed that the uncertainties in the bearing, like the distortion in the raceway, can be defined with only a small set of parameters that can be calibrated with only a few measurements.

4

Conclusions and recommendations

For SKF it would be useful to have a fast model of a bearing which calculates the strains for certain loads for their development of a load sensing algorithm. During this thesis, a model was developed in order to achieve this goal.

The semi-analytical model consists of a part that calculates the load and contact angle of each rolling element, by means of a rigid bearing model and a raceway deformation model, and a part that converts these into strains on the surface of the bearing. This last part, which is called the strain model, and the raceway deformation model, are constructed from a set of linear elastic FEA simulations. These simulations contain a finite element model of an outer ring on which a single rolling element is modeled with the Hertzian contact model. The inner ring of the bearing is assumed rigid. The model can be run continuously for different loads and positions of the rolling elements to obtain strain signals in the time domain.

The model is compared with experiments performed on the BEaring Test SYstem (BETSY) at SKF on which a modified HBU3 bearing is placed. All the phenomena that can be observed in the signals as a result of the load are predicted by the model, and both the model and the experiments show similar trends. With the model it becomes much easier to understand the experiments, because not only the strains are generated, but also the individual rolling element loads and contact angles can be extracted, and the direct relation between these and the strain signal. This gives insights on how the physical shape of the bearing influences the strains, which can be used to improve the bearing design and strain gauge location during the development of the load sensing bearing.

The results of the comparison show that the bearing itself shows unexpected behavior, which is likely caused by static deformations of the raceways, which in turn modify the distribution of the loads over all the rolling elements. There is also doubt in the

precision of the placement and installation of the strain gauges. These factors have a large influence on the signal, making it very hard to compare them to the model. A difference is observed between the model and the measured strains which is in the same order of magnitude as the difference caused by the unforeseen static raceway deformations and the uncertainties in the strain gauges, making any quantitative measures to compare the two of limited value. Other than that the model predicts the same general behavior as can be seen in the experiments, indicating that the main processes that act in the bearing are simulated properly. However, any quantifiable conclusions about the performance of the model can not yet be made.

4.1. Research subquestions

In the introduction of this thesis, some subquestions to the research question were made. Throughout the report, the evidence to answer these questions are stated. The questions and their summarized answers are:

What mechanics in the bearing determine the loads and contact angles on each rolling element?   Both the contacts of the rolling elements with the raceways and the flexibility of the outer ring can be considered as spring. By finding the equilibrium of all the forces acting on all the bodies, a distribution of the loads over the rolling elements and their contact angles can be found.

What are the effects of the contact angle on the first and second harmonics of the strain signal?   As the rolling element moves closer to the strain sensor due to a change in contact angle, the harmonics of the signal rise. The ratio between the second and first harmonic is a function of the contact angle but is independent of the load that acts on the rolling elements. This ratio might be used to estimate the contact angles of the rolling elements.

Are the strains in the time domain and the spatial domain related?   Analysis of the raceway deformation shows that the outer ring has a varying stiffness along the azimuth. This causes a load distribution during rotation that is different in the time domain than in the spatial domain. The same can be said for a non-symmetric load on the bearing. This means that the strains measured in the time domain cannot be converted into the spatial domain.

How can the FEA be simplified to decrease the computation time, but maintain accuracy?   Various simplifications are made to the FEA to decrease its computation time. An optimization of the mesh size ensures a good accuracy while decreasing the time to solve the simulations. The whole FEA of the outer ring is made linear elastic by ensuring that no contact constraint has to be used between the outer

ring and the plate. The rolling elements are replaced by a Hertzian contact model, thus also removing a nonlinear contact constraint.

4.2. Recommendations and future work

Much work is still to be done in order to improve the model. If this is done, there are many potential usages for the model in the future. The following recommendations are made:

- The model should be calibrated in order to improve its accuracy. It is believed that the factors that create the unexpected bearing behavior can be summarized in a few parameters, which all need to be calibrated:

  Strain gauge properties Due to inaccuracies in the installation process of these strain gauges, they can deform, thus creating a static offset in the strain signal. Also, the exact location, adhesive under the sensor, and gauge factor can influence the strain signal. This might be resolved by calibrating a coefficient to the simulated sensor signal.

  Static raceway deformation Modifying the bearing for the experiments and clamping it tight on the plate might have created a static deformation of the raceways. Keep in mind that any local deformation in the raceway will influence the loads and contact angles on all the rolling elements. The static raceway deformation is not easily contained in only a few parameters, since it is continuously varying along each raceway. Further research is needed to identify all the sources for this raceway deformation in order to calibrate it, or find a method to manufacture or install the bearing without any static deformation at all.

  Preload All HBU3 bearings are assembled with a preload. This is defined by a single parameter, but this could be considered as an even static raceway deformation and be incorporated in calibrating the static raceway deformation.

- The FEA simulations were done without any contact constraints, and the whole bearing was mounted solid to the plate via washers, thus making the FEA linear and fast to solve. This linearity is imitated in the experiments by mounting the bearing via washers on the plate, ensuring no varying contact. Further experiments and simulations without washers need to be compared in order to investigate the accuracy of the model under these conditions. Alternatively, the bearing can be redesigned such that linear behavior in this contact guaranteed.

- If the model is found to be accurate, it can be used to analyze different strain gauge locations. An optimization can be made such that a set of locations is found that is able to reconstruct the load while minimizing the number of strain gauges, thus reducing the costs of this load sensing bearing.

- The goal of the model was to estimate the strains on a bearing when a load is applied, but it might also be used to estimate defects in bearings. When a large cavity is present in the outer ring, a so-called spall, this might be detected in the strain signals. When a rolling element enters a spall, its load temporarily reduces. This means that the load is carried over the other rolling elements, which gives a signature that might be detected in the strain signals. To fully model this behavior, the model needs to be extended with a transient model that simulates the rolling element rolling out of the spall.

- As explored by [19], a model can be used to create a state observer that estimates the load based on the strain measurements. The advantage of a model-based estimator, as opposed to a data-driven estimator, is that less calibration will be needed since the calibration parameters can be a set of measurable physical parameters.

As more knowledge is acquired about all the phenomena that occur in HBU3 bearings and the understanding of the strain signals increases, a better load estimation algorithm can be designed. In the not too far future, we might see cars equipped with load sensing bearings as standard, for improved car control and safety, with controllers that use the wheel loads as input states.

REFERENCES

[1] S. Tsugawa, "Automated driving systems: Common ground of automobiles and robots," *International Journal of Humanoid Robotics*, vol. 08, no. 01, pp. 1–12, 2011. Link: https://doi.org/10.1142/S0219843611002319

[2] V. K. Kukkala, J. Tunnell, S. Pasricha, and T. Bradley, "Advanced driver-assistance systems: A path toward autonomous vehicles," *IEEE Consumer Electronics Magazine*, vol. 7, no. 5, pp. 18–25, Sept 2018. Link: https://doi.org/10.1109/MCE.2018.2828440

[3] C. H. Jeong, J. Y. Kim, and D. H. Jung, "Research on vehicle stability technology based on wheel force," *International Journal of Automotive Technology*, vol. 16, no. 3, pp. 435–445, Jun 2015. Link: https://doi.org/10.1007/s12239-015-0045-y

[4] C.-K. Chae, B.-K. Bae, K.-J. Kim, J.-H. Park, and N.-C. Choe, "A feasibility study on indirect identification of transmission forces through rubber bushing in vehicle suspension system by using vibration signals measured on links," *Vehicle System Dynamics*, vol. 33, no. 5, pp. 327–349, 2000. Link: https://doi.org/10.1076/0042-3114(200005)33:5;1-Q;FT327

[5] Kistler Group, "www.kistler.com," Link: https://www.kistler.com.

[6] MTS Systems Corporation, "www.mts.com," Link: https://www.mts.com.

[7] F. Braghin, M. Brusarosco, F. Cheli, A. Cigada, S. Manzoni, and F. Mancosu, "Measurement of contact forces and patch features by means of accelerometers fixed inside the tire to improve future car active control," *Vehicle System Dynamics*, vol. 44, no. sup1, pp. 3–13, 2006. Link: https://doi.org/10.1080/00423110600867101

[8] F. Cheli, D. Ivone, and E. Sabbioni, "Smart tyre induced benefits in sideslip angle and friction coefficient estimation," in *Sensors and Instrumentation, Volume 5*, E. Wee Sit, Ed. Cham: Springer International Publishing, 2015, pp. 73–83. Link: https://doi.org/10.1007/978-3-319-15212-7_9

[9] A. Tuononen, "On-board estimation of dynamic tyre forces from optically measured tyre carcass deflections," *International Journal of Heavy Vehicle Systems (IJHVS)*, vol. 16, no. 3, pp. 362–378, 2009. Link: https://doi.org/10.1504/IJHVS.2009.027139

[10] J. den Engelse, "Estimation of the lateral force acting at the tire contact patch of a vehicle wheel using a hub bearing unit instrumented with strain gauges and eddy-current sensors," Master's thesis, Delft University of Technology, 2013. Link: http://resolver.tudelft.nl/uuid:fc936c60-314b-4366-9030-aeb5316e0468

[11] K. Nishikawa, "Hub bearing with integrated multi-axis load sensor," *NTN Technical Review*, vol. 79, pp. 58–63, 2011. Link: http://www.ntnglobal.com/en/products/review/pdf/NTN_TR79_en_p058_063.pdf

[12] K. Ono, T. Takizawa, and M. Aoki, "Preload measuring device for double row rolling bearing unit," U.S. Patent 8 864 382, October 21, 2014. Link: http://www.freepatentsonline.com/8864382.html

[13] J. Van Doornik, "Haptic feedback on the steering wheel near the vehicle's handling limits using wheel load sensing," Master's thesis, Delft University of Technology, 2014. Link: http://resolver.tudelft.nl/uuid:fc11179e-9aa9-4a13-9dda-21c45d6747b1

[14] D. De Bot, "A temperature state estimator for a load sensing hub bearing unit," Master's thesis, Delft University of Technology, 2009. Link: http://resolver.tudelft.nl/uuid:60000ecc-cd80-4330-b6c1-f16e23a0947f

[15] A. Jayashankar, "Experimental & modeling study of the influence of support stiffness on load sensing bearings," Master's thesis, Delft University of Technology, 2011. Link: http://resolver.tudelft.nl/uuid:e3728796-78b6-4c61-b95e-f55b4e30762c

[16] T. A. Harris, *Rolling bearing analysis; 3rd ed.* New York, NY: John Wiley and Sons, 1991, the book can be consulted by contacting: EN-ACE-SU: Kemppinen, Juha Mikko Kalervo. Link: https://cds.cern.ch/record/2196766

[17] COMSOL Inc., "Structural contact modeling guidelines," Link: https://www.comsol.com/support/knowledgebase/1102/.

[18] S. Timoshenko, J. Goodier, and McGraw-Hill, *Theory of Elasticity, 2nd Ed.*, 1934.

[19] S. Kerst, B. Shyrokau, and E. Holweg, "A semi-analytical bearing model considering outer race flexibility for model based bearing load monitoring," *Mechanical Systems and Signal Processing*, vol. 104, pp. 384 – 397, 2018. Link: https://doi.org/10.1016/j.ymssp.2017.11.008

[20] L. Ambarwati and H. Gunawan, "Two dimensional interpolation using tensor product of chebyshev systems," *Proceedings of the Third International Conference on Mathematics and Natural Sciences*, pp. 970–981, 2010. Link: https://www.researchgate.net/publication/267409188

[21] W. Frei, "Solving nonlinear static finite element problems," *COMSOL Blog*, 2013. Link: https://www.comsol.com/blogs/solving-nonlinear-static-finite-element-problems/

[22] W. Frei, "Load ramping of nonlinear problems," *COMSOL Blog*, 2013. Link: https://www.comsol.com/blogs/load-ramping-nonlinear-problems/

[23] W. Frei, "How much memory is needed to solve large comsol models?" *COMSOL Blog*, 2014. Link: https://www.comsol.com/blogs/much-memory-needed-solve-large-comsol-models/

A
DIMENSIONLESS CONTACT PARAMETERS

The dimensionless contact parameters are used in calculating the semi axes of the Hertzian contact ellipse and the contact deformation. These parameters are shown in table A.1.

$F(\rho)$	a^*	b^*	δ^*
0	1	1	1
0.1075	1.076	0.9318	0.9974
0.3204	1.2623	0.8114	0.9761
0.4795	1.4556	0.7278	0.9429
0.5916	1.644	0.6687	0.9077
0.6716	1.8258	0.6245	0.8733
0.7332	2.011	0.5881	0.8394
0.7948	2.265	0.548	0.7961
0.83495	2.494	0.5186	0.7602
0.87366	2.8	0.4863	0.7169
0.90999	3.233	0.4499	0.6636
0.93657	3.738	0.4166	0.6112
0.95738	4.395	0.383	0.5551
0.9729	5.267	0.349	0.496
0.983797	6.448	0.315	0.4352
0.990902	8.062	0.2814	0.3745
0.995112	10.222	0.2497	0.3176
0.9973	12.789	0.2232	0.2705
0.9981847	14.839	0.2072	0.2427
0.9989156	17.974	0.18822	0.2106
0.9994785	23.55	0.16442	0.17167
0.9998527	37.38	0.1305	0.11995
1	∞	0	0

Table A.1: Dimensionless contact parameters for the Hertzian model.

B

SINGULAR VALUE DECOMPOSITION OF THE COMPLIANCE OF THE RDM

In subsection 2.3.3 the compliance function of the Raceway Deformation Model (RDM) is analyzed. This compliance function gives the deformation of the raceway per applied load and it is a function of the azimuth of this deformation, and the azimuth of the applied load. The singular value decomposition of the compliance function of row 1 is shown in figures B.1, B.2, and B.3.
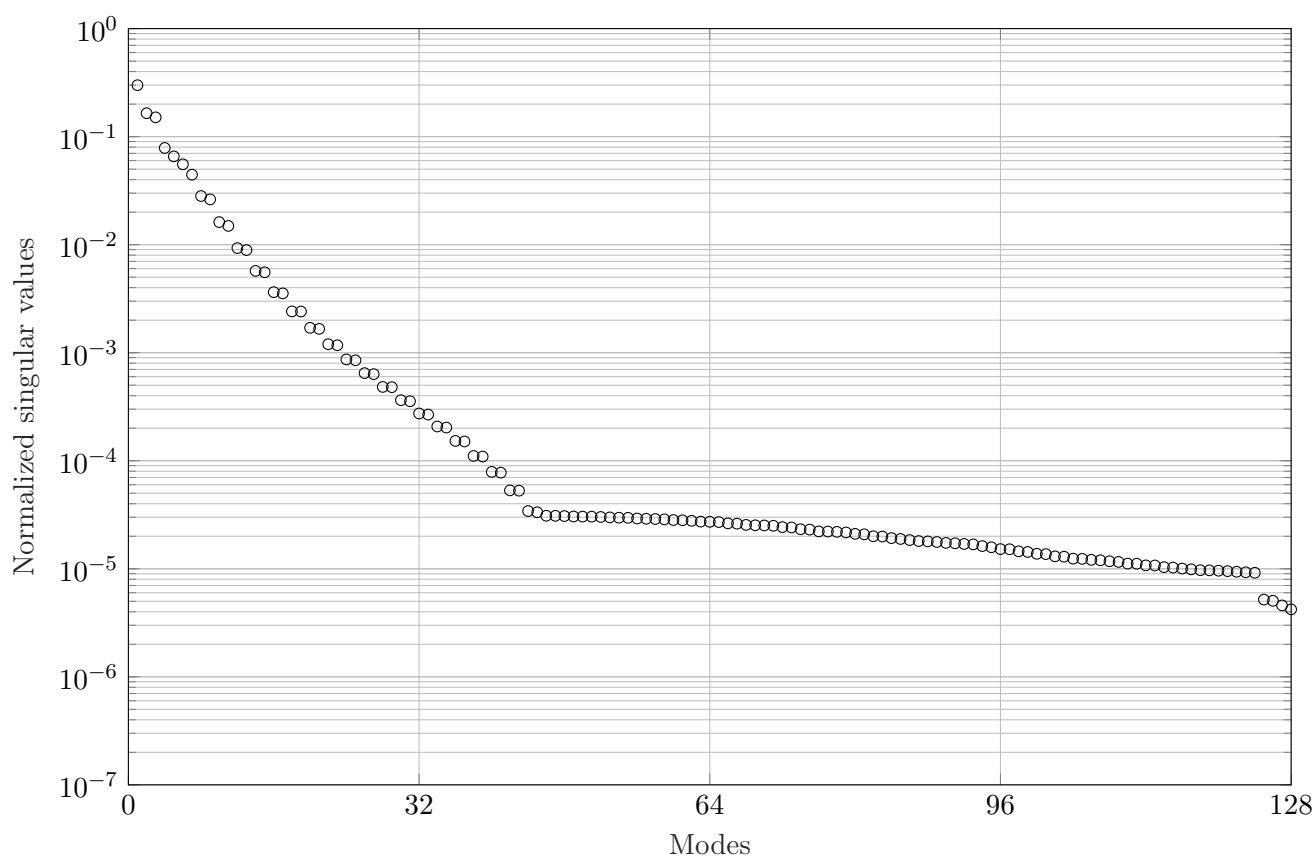

Figure B.1: Normalized singular values of the compliance function of row 1. Note that singular values 8 to 41 show up in pairs of equal value. This implies a symmetry along the $x = y$ plane of the compliance function.
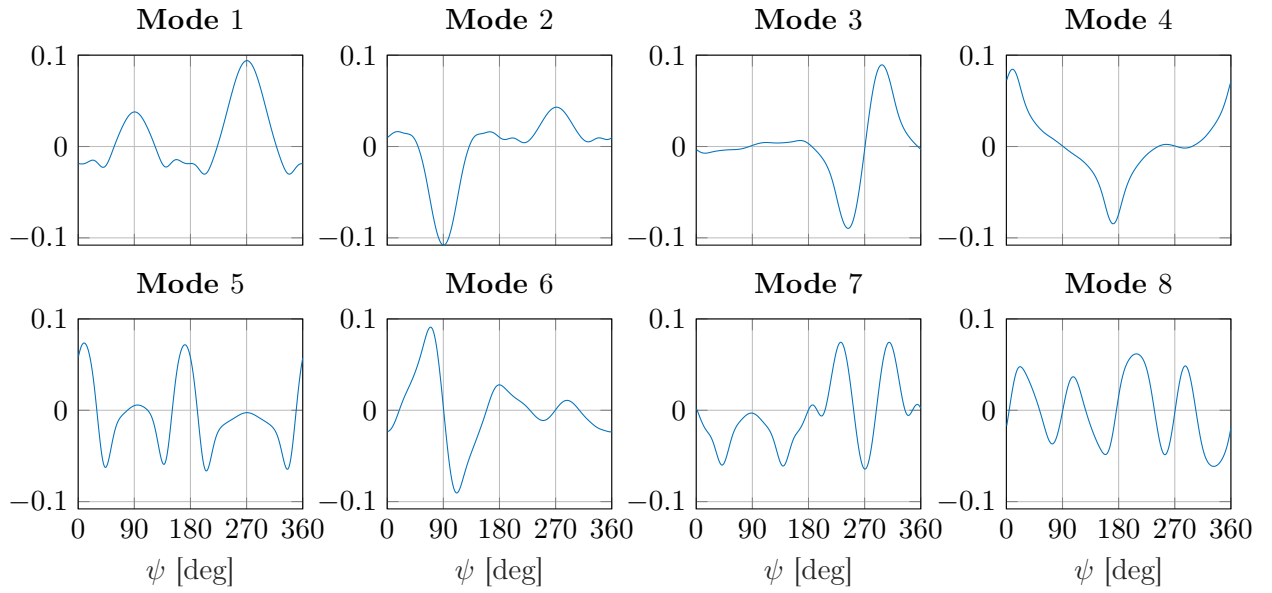
Figure B.2: The first 8 left-singular vectors of the compliance function of row 1. The effect of the stiff bolt holes located at azimuths 40°, 140°, 200°, and 340° can clearly be seen.
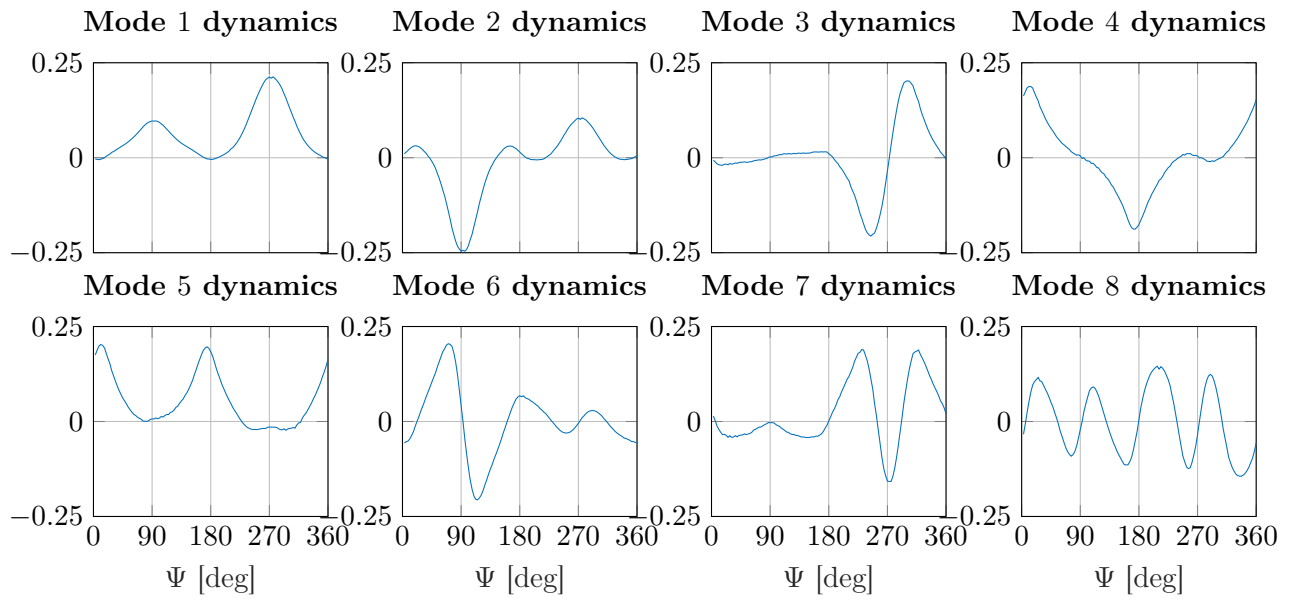
Figure B.3: The first 8 right-singular vectors of the compliance. Note how similar these are to their corresponding left-singular vectors.

C

SINGULAR VALUE DECOMPOSITION OF THE ROTATED COMPLIANCE OF THE RDM

In subsection 2.3.3 the compliance function of the Raceway Deformation Model (RDM) is analyzed. The symmetry along the $x = y$ plane is further analyzed by looking at the 'rotated' compliance function of row 1. This function gives the raceway deformation per applied load. It is a function of the azimuth of the deformation, and because it is 'rotated', also of the difference between the azimuth of the applied load and the azimuth of the deformation. The singular value decomposition of this 'rotated' compliance function of row 1 is shown in figures C.1, C.2, and C.3.
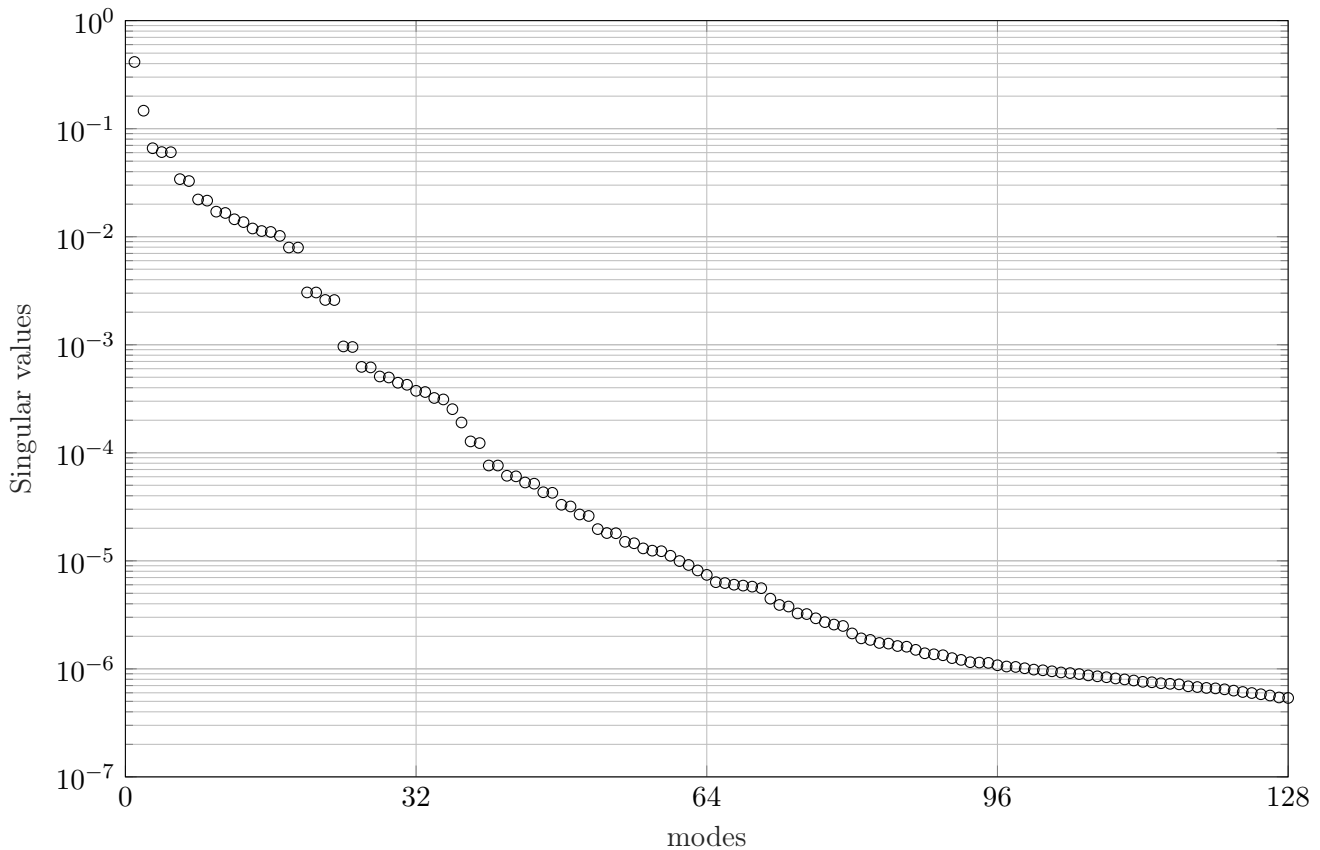
Figure C.1: Singular values of the 'rotated' compliance function of row 1. As with the normal compliance function, some singular values appear in pairs. This suggest that in this 'rotated' reference frame there is still some symmetry.
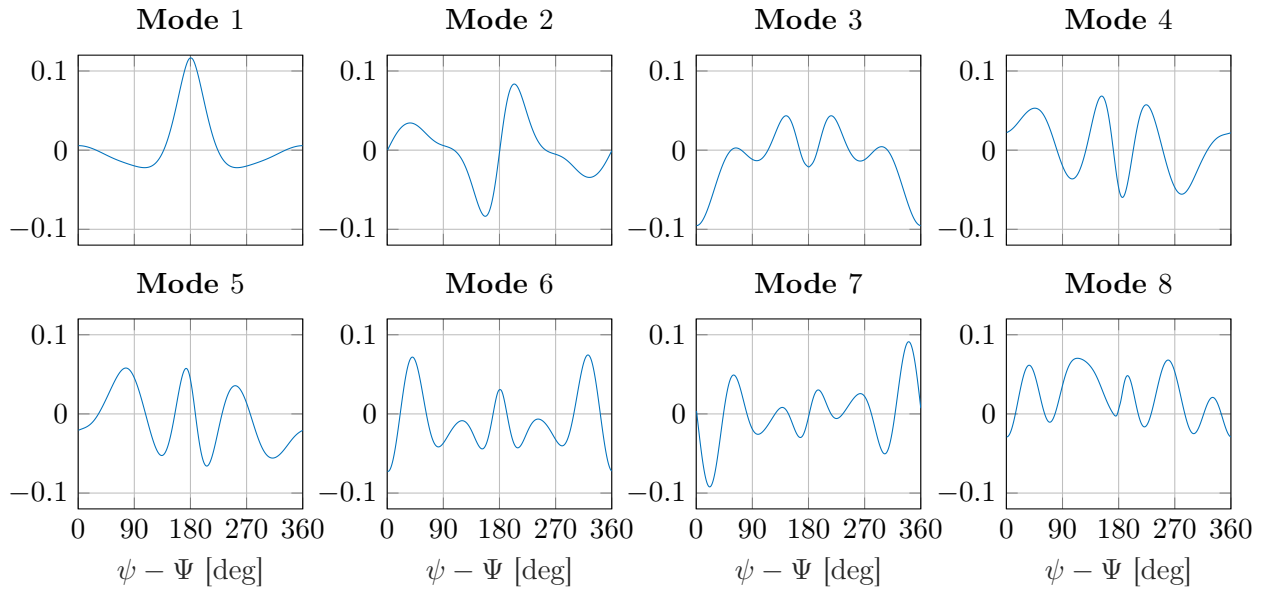
Figure C.2: The first 8 left-singular vectors of the 'rotated' compliance function of row 1. Most of the modes are either symmetric or anti-symmetric.
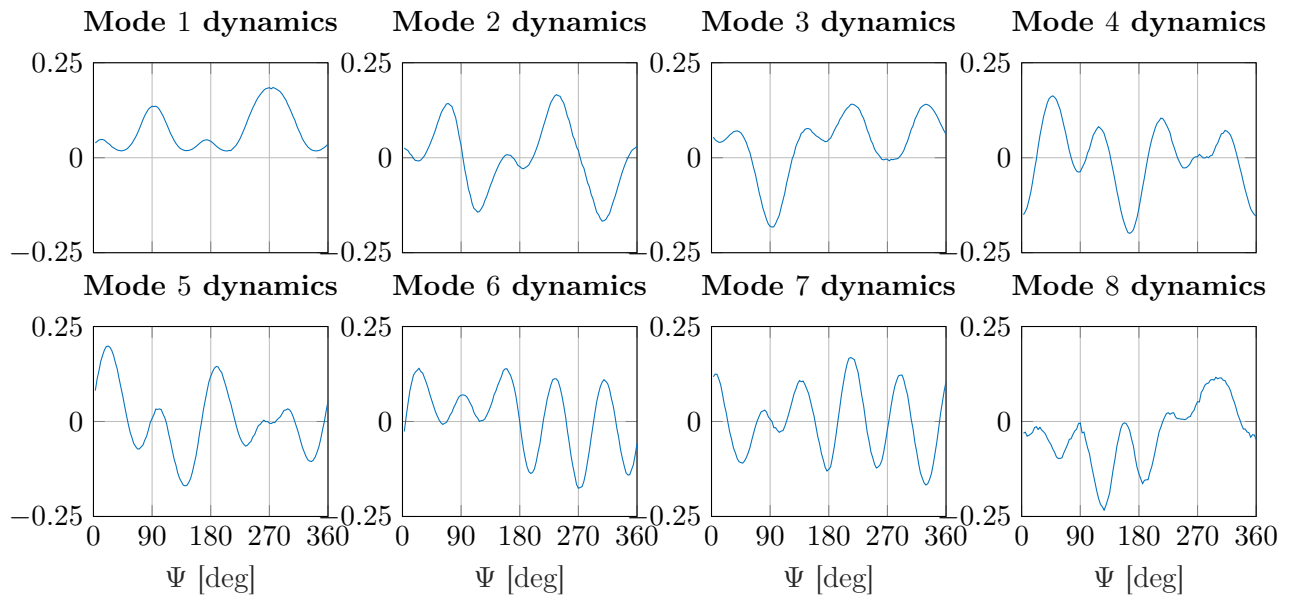

Figure C.3: The first 8 right-singular vectors of the 'rotated' compliance function of row 1.

D
LOAD CASE FOR RACEWAY DEFORMATION VERIFICATION

Quantity	Value	Unit
F_x	-73	N
F_y	852	N
F_z	13150	N
M_x	-312	Nm
M_z	249	Nm

(a) Forces acting on bearing.

Element number	Row 1		Row 2	
	Q [N]	α [°]	Q [N]	α [°]
1	930	43.9	-	-
2	1230	43.7	-	-
3	1281	43.2	-	-
4	1267	42.3	-	-
5	1487	40.9	-	-
6	1839	39.2	653	36.9
7	1783	38.0	1971	37.2
8	1486	37.2	3122	37.5
9	1513	36.6	4204	37.6
10	1123	36.6	3762	38.0
11	608	37.3	2120	38.8
12	383	38.2	723	39.1
13	395	39.5	-	-
14	460	40.8	-	-
15	599	42.2	-	-
16	747	43.3	-	-

(b) Contact loads and contact angles of all rolling elements.

Table D.1: Forces acting on bearing and rolling elements for the load case for raceway deformation model verification.

E

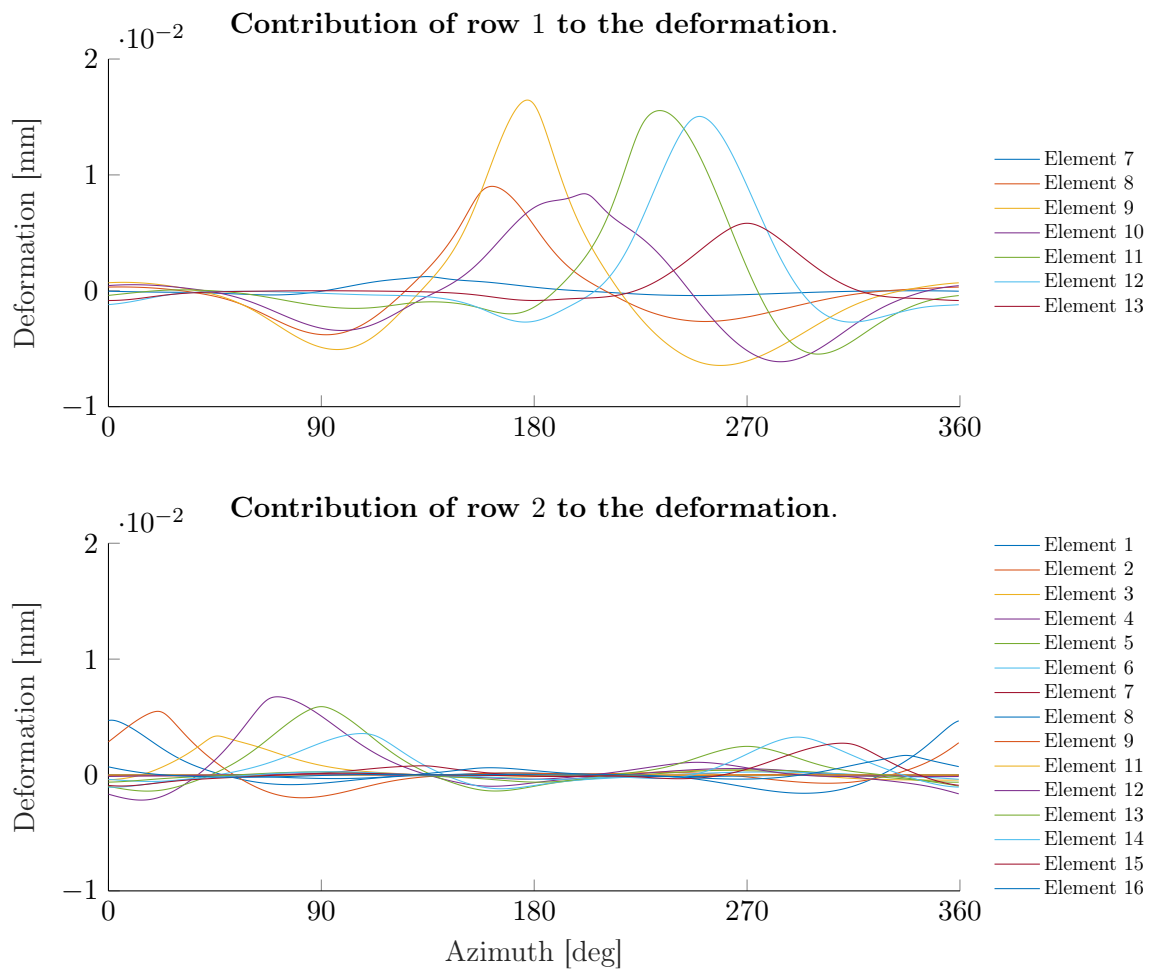## INDIVIDUAL CONTRIBUTIONS ON THE SUPERIMPOSED DEFORMATION

Figure E.1: Contribution of all the elements on both rows to the radial deformation of row 1.

Quantity	Value	Unit
F_x	-1325	N
F_y	-5863	N
F_z	11417	N
M_x	-1799	Nm
M_z	370	Nm

(a) Forces acting on bearing.

Element	Row 1		Row 2	
number	Q [N]	α [°]	Q [N]	α [°]
1	-	-	5252	47.4
2	-	-	6869	48.2
3	-	-	7268	48.2
4	-	-	5354	48.1
5	-	-	3342	47.0
6	-	-	2777	43.4
7	1668	35.1	1881	40.3
8	5338	36.3	738	37.8
9	8457	37.2	9	36.4
10	10891	37.4	-	-
11	8563	38.5	6	35.0
12	4711	39.5	647	34.8
13	1648	39.1	1472	36.3
14	-	-	1973	39.2
15	-	-	2609	42.3
16	-	-	3894	45.0

(b) Contact loads and contact angles of all rolling elements.

Table E.1: Forces acting on bearing and rolling elements for load case 1.

F
ALL THE HARMONICS IN THE SIGNALS FOR AXIAL LOADS

During one set op experiments different axial loads ranging from $-10\,\text{kN}$ to $10\,\text{kN}$ are applied to the bearing in increments of $3.33\,\text{kN}$. This creates 7 separate load cases. When transforming the strain signal measured by each strain gauge to the frequency domain a clear distinction can be made between the contribution of each row to the signal. The zeroth, first and second harmonics of these signals are plotted in the figures shown in this appendix and compared with the modeled strains. Although large differences can be observed between the measured strains on BETSY and the modeled strains, the general behavior seen in the experiments can also be seen in the model. These load cases are discussed in section 3.2.
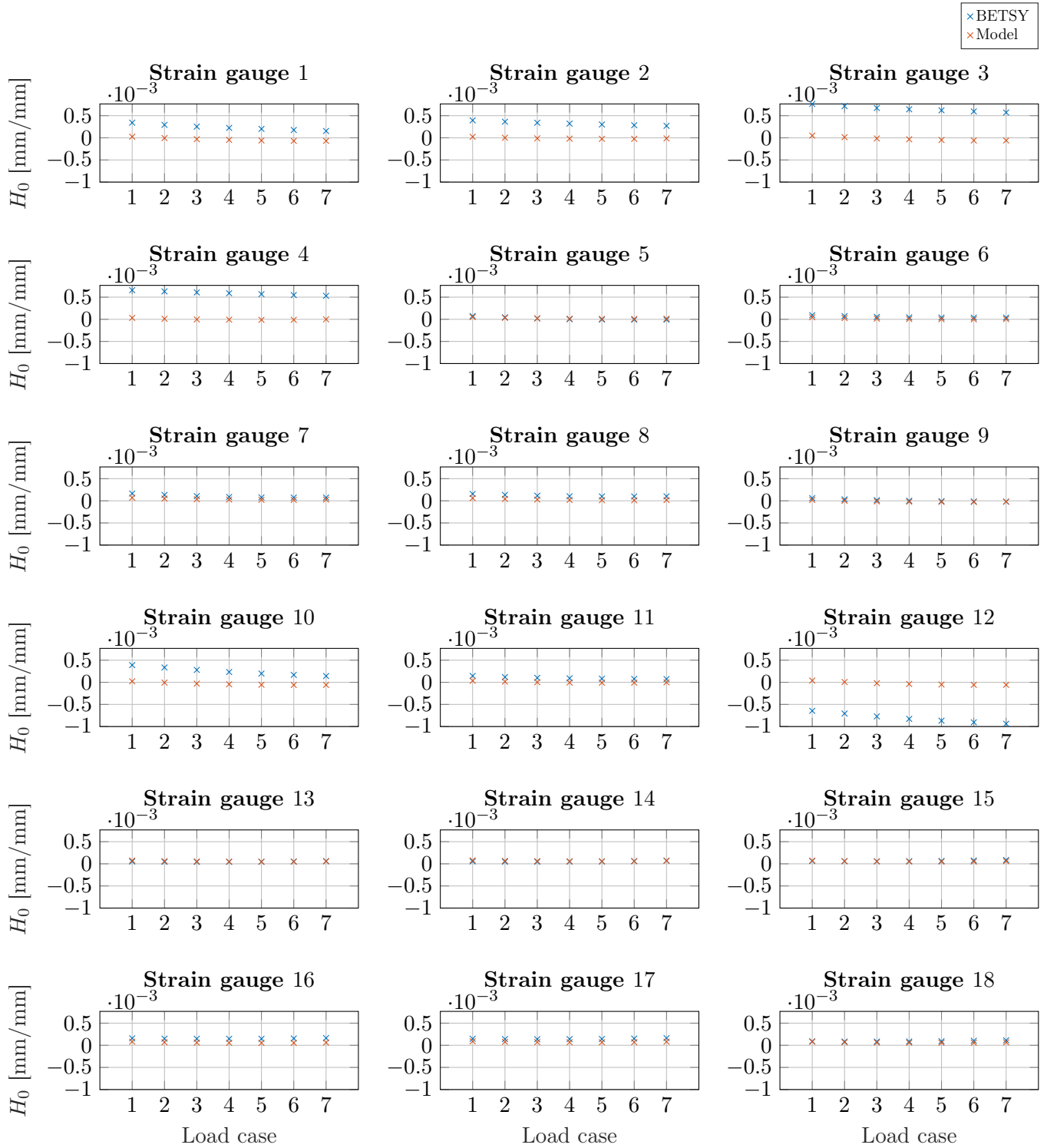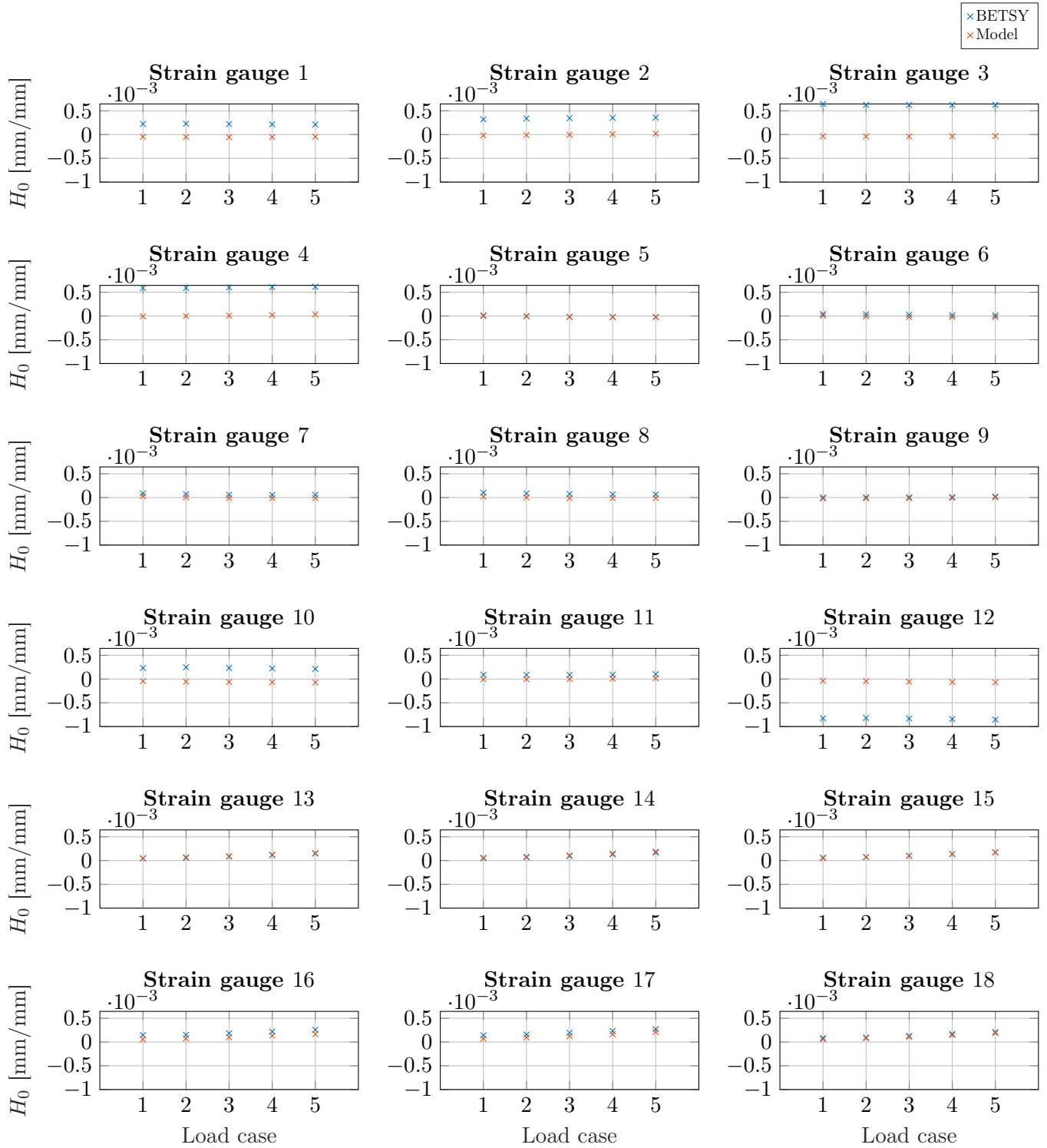
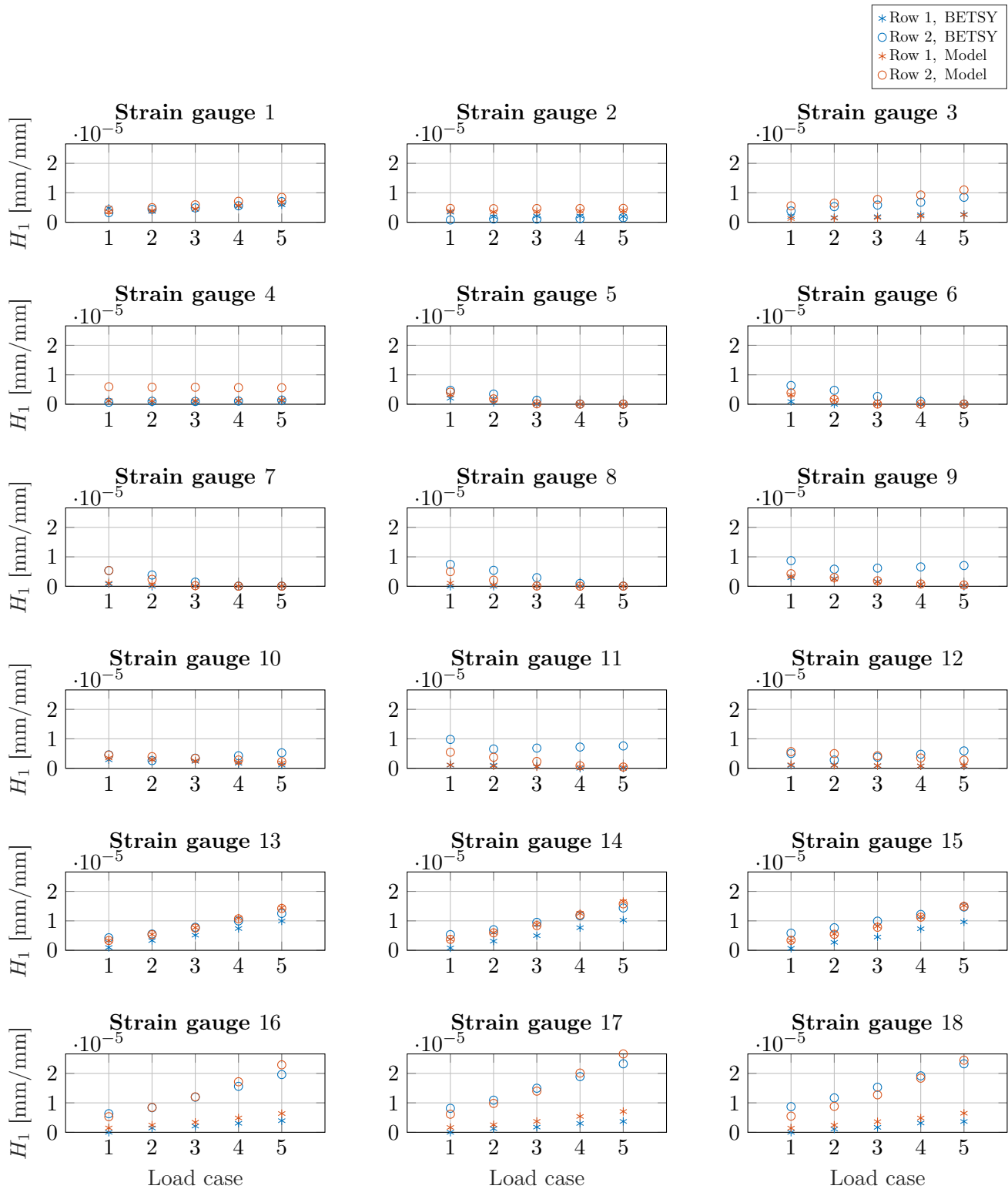Figure F.1: The zeroth harmonics (mean) of the measured and modeled strains.
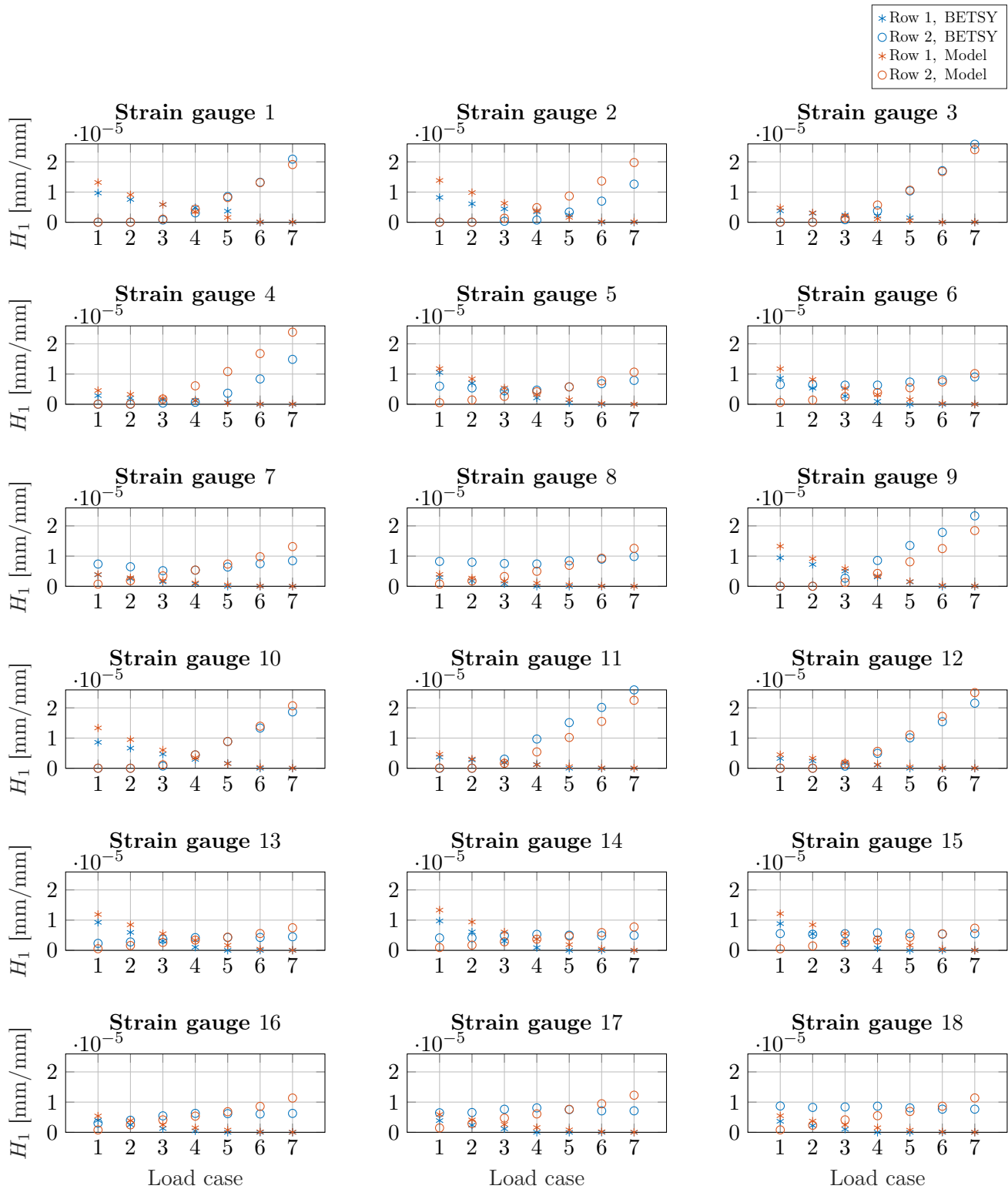
Figure F.2: The first harmonics of the measured and modeled strains.
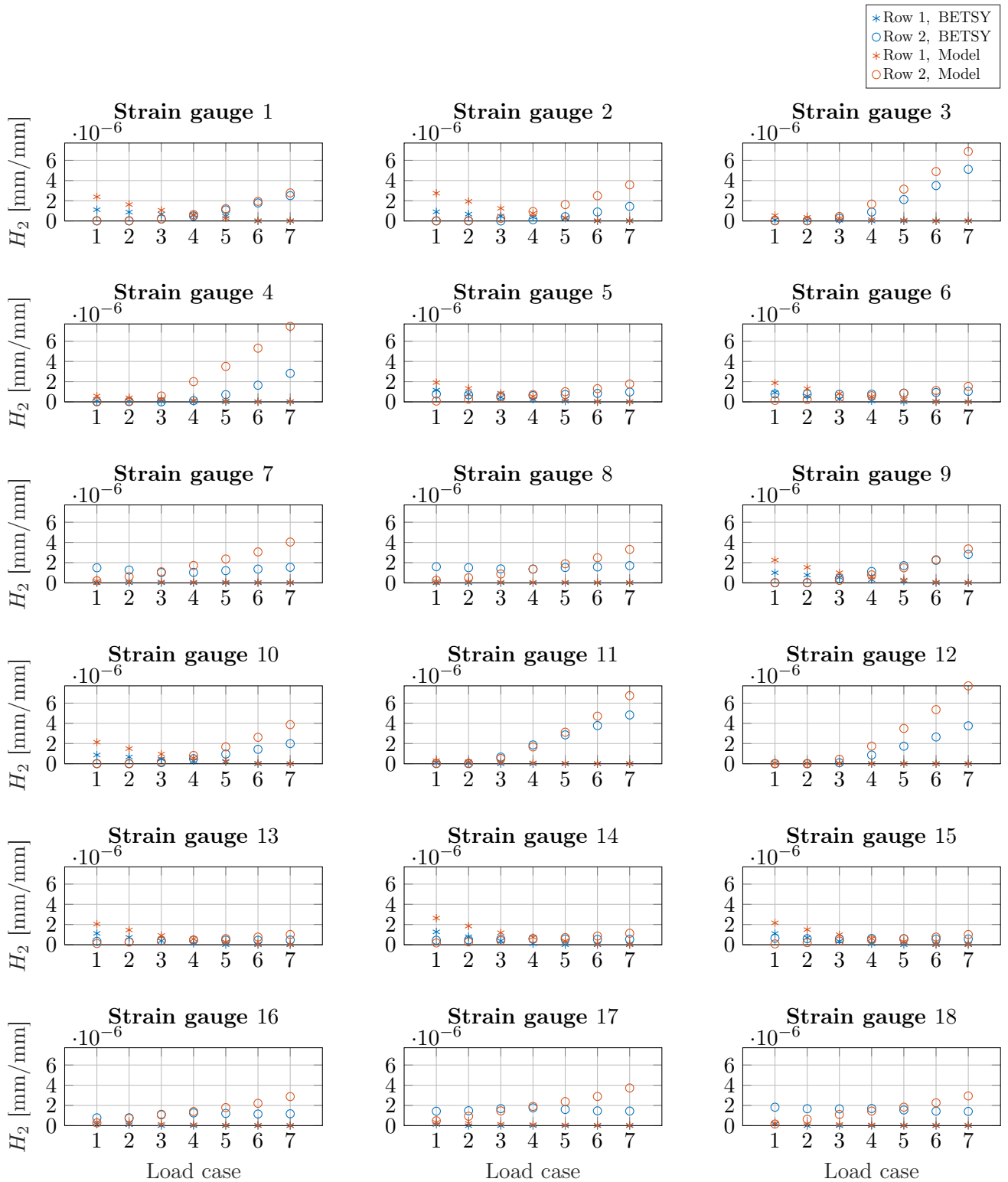
Figure F.3: The second harmonics of the measured and modeled strains.

G

ALL THE HARMONICS IN THE SIGNALS FOR RADIAL LOADS

Radial loads ranging from $0\,\mathrm{kN}$ to $8\,\mathrm{kN}$ are applied to the bearing in increments of $2\,\mathrm{kN}$. This creates 5 separate load cases. When transforming the strain signal measured by each strain gauge to the frequency domain a clear distinction can be made between the contribution of each row to the signal. The zeroth, first and second harmonics of these signals are plotted in the figures shown in this appendix and compared with the modeled strains. Although large differences can be observed between the measured strains on BETSY and the modeled strains, the general behavior seen in the experiments can also be seen in the model. These load cases are discussed in section 3.3.

Figure G.1: The zeroth harmonics (mean) of the measured and modeled strains.

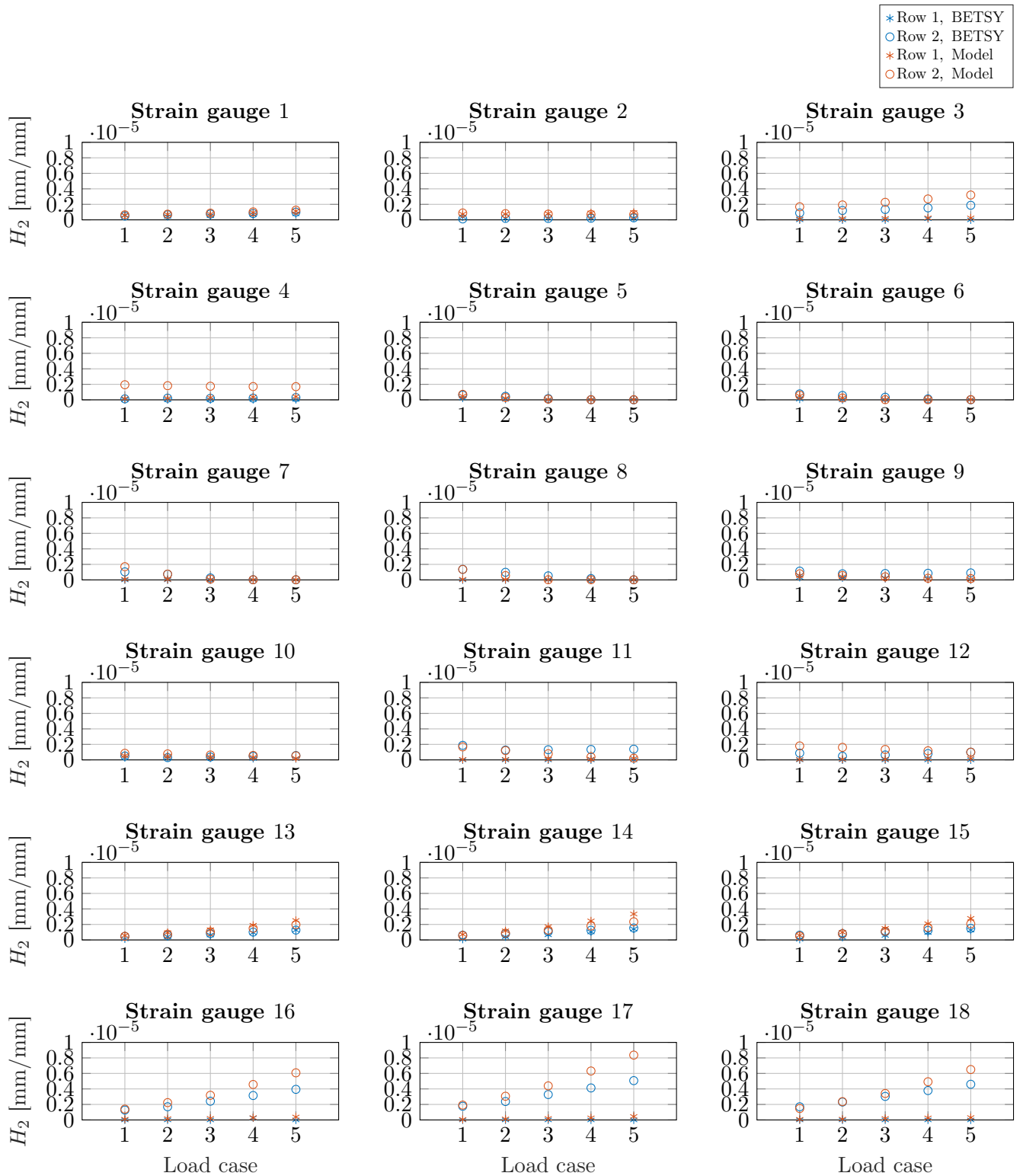Figure G.2: The first harmonics of the measured and modeled strains.

Figure G.3: The second harmonics of the measured and modeled strains.

H

ALL THE HARMONICS IN THE SIGNALS FOR MOMENT LOADS

Different moments ranging from $0\,\text{kN\,m}$ to $2.5\,\text{kN\,m}$ is applied to the bearing in increments of $500\,\text{N\,m}$. This creates 6 separate load cases. When transforming the strain signal measured by each strain gauge to the frequency domain a clear distinction can be made between the contribution of each row to the signal. The zeroth, first and second harmonics of these signals are plotted in the figures shown in this appendix and compared with the modeled strains. Although large differences can be observed between the measured strains on BETSY and the modeled strains, the general behavior seen in the experiments can also be seen in the model. These load cases are discussed in section 3.4.
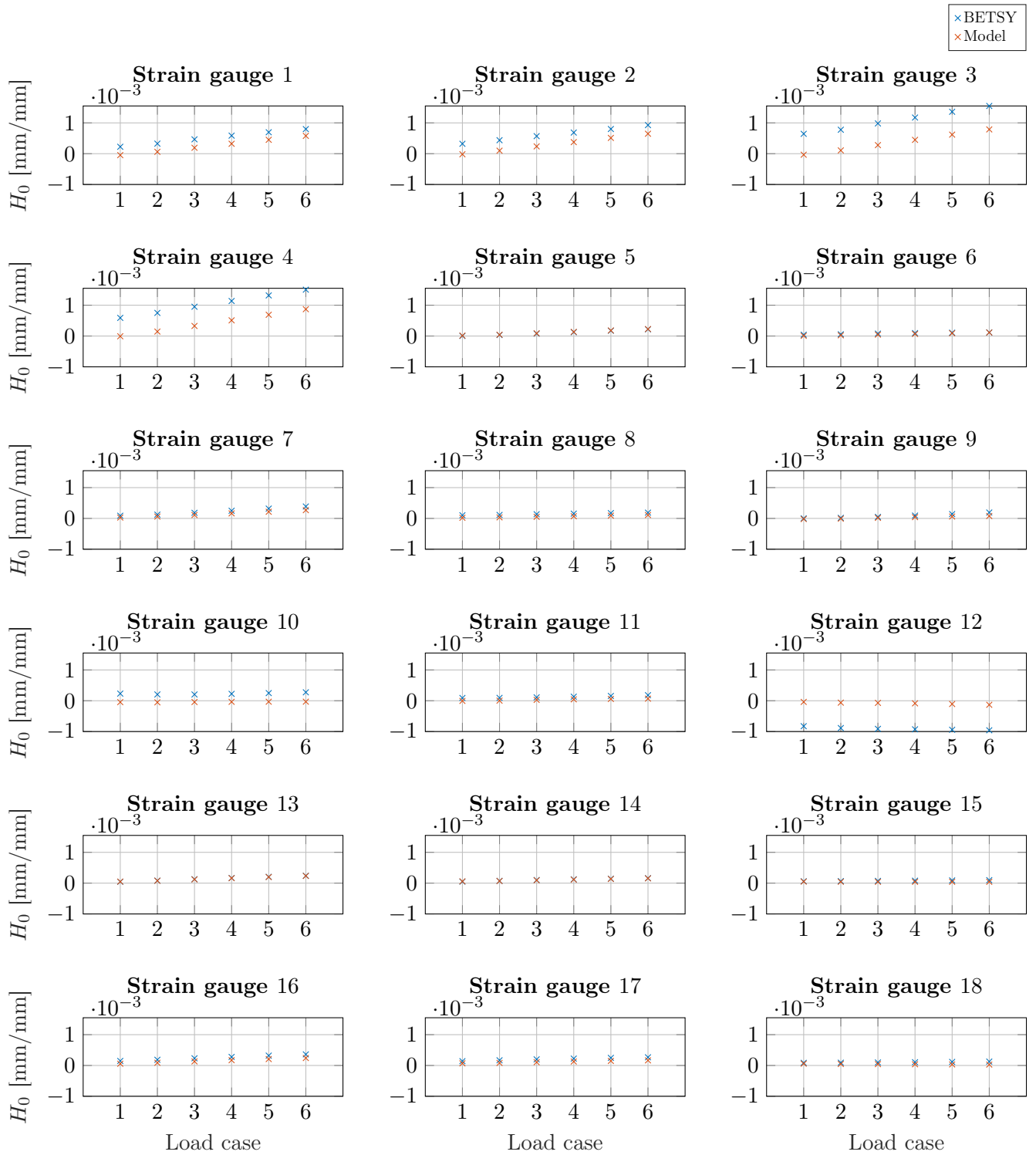
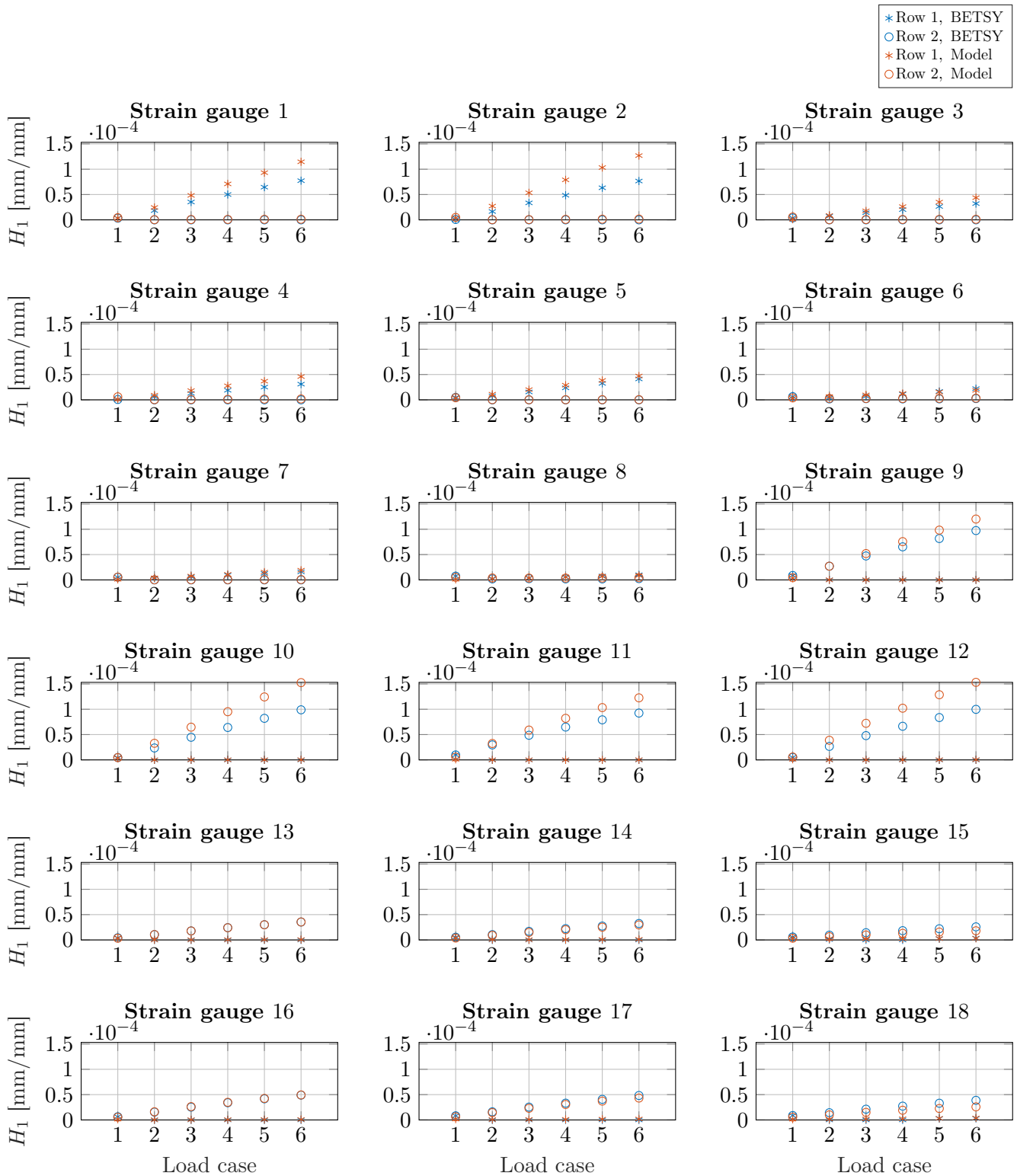Figure H.1: The zeroth harmonics (mean) of the measured and modeled strains.

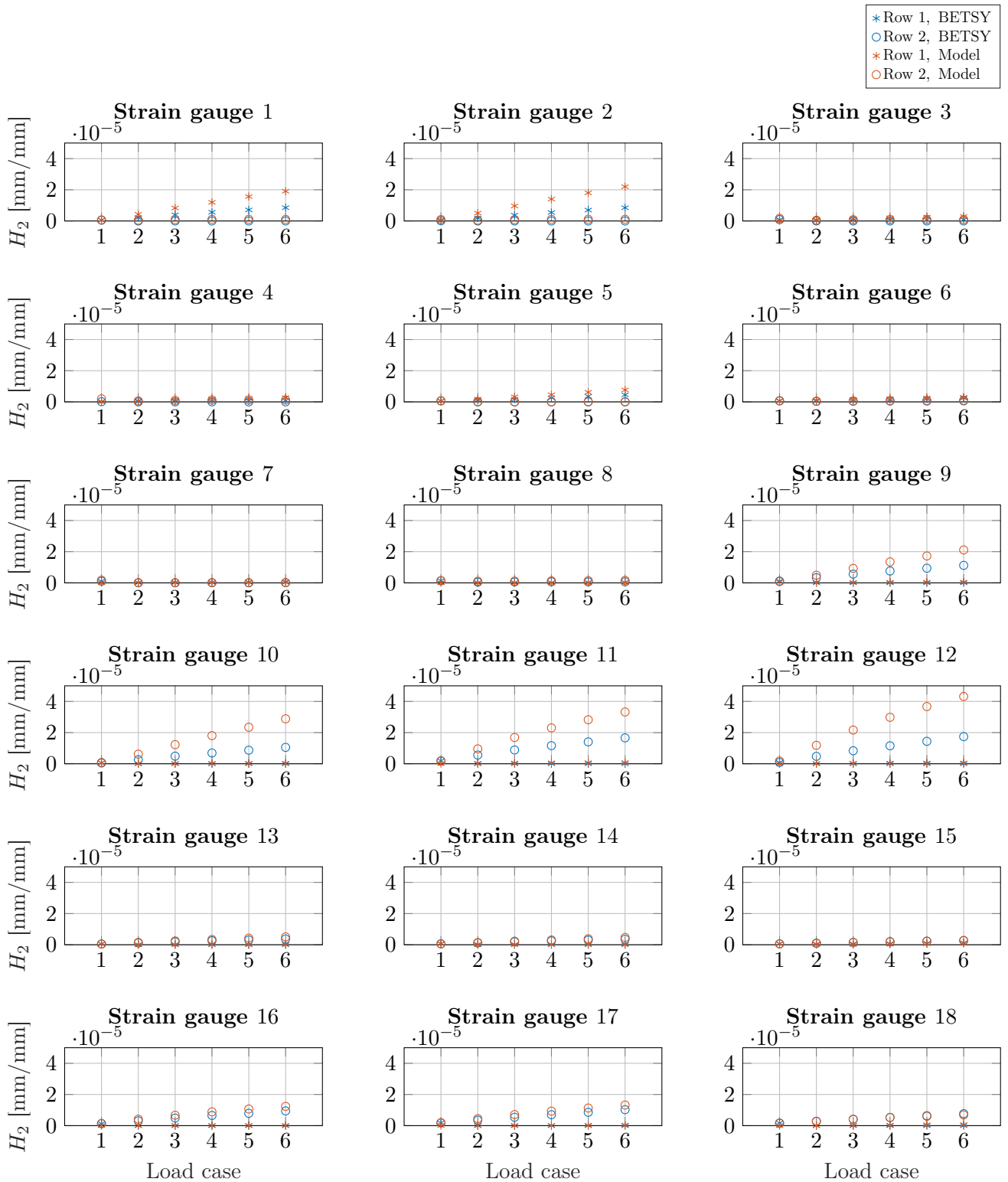Figure H.2: The first harmonics of the measured and modeled strains.

Figure H.3: The second harmonics of the measured and modeled strains.